



Fisica

CORSO DI DOTTORATO DI RICERCA IN

XXXV

CICLO DEL CORSO DI DOTTORATO

Accreting black holes and neutron stars probed with X-ray polarimetry

Titolo della tesi

Romana Mikušincová

Nome e Cognome del dottorando

firma

Prof. Giorgio Matt

Docente Guida/Tutor: Prof.

firma

Prof. Giuseppe Degrassi

Coordinatore: Prof.

firma



Accreting black holes and neutron stars probed with X-ray polarimetry

Dipartimento di Matematica e Fisica
Dottorato di Ricerca in Fisica (XXXV cycle)

Romana Mikušincová

ID number 762

Advisor

Prof. Giorgio Matt

Academic Year 2021/2022

Thesis not yet defended

Accreting black holes and neutron stars probed with X-ray polarimetry

PhD thesis. Roma Tre University of Rome

© 2023 Romana Mikušincová. All rights reserved

This thesis has been typeset by \LaTeX and the Sapthesis class.

Author's email: romana.mikusincova@uniroma3.it

.to dreamers

The dedication of this Thesis is split n ($n \in \mathbb{N}$) ways:

First and foremost, my sincere gratitude goes to my supervisor, Professor Giorgio Matt. I am grateful for his excellent guidance, dedicating his time and energy to teach me and giving me the opportunity to learn from him and gain invaluable skills and knowledge. It is for his effort, commitment, patience, convenient ideas, helpful advice and useful comments that this thesis was created. The best that is in this thesis is dedicated to him.

I am grateful to RNDr. Michal Dovčiak, PhD for the continuous opportunity to learn from him, for his effort to teach me whenever I needed help.

My sincere gratitude goes to Dr. Roberto Taverna for his immense patience, effort and willingness to teach me, explain, and discuss ideas, issues, and error messages. Thank you.

Another important thank you is dedicated to Dr. Francesco Ursini, for numerous consults, explanations, and discussions over data analysis, and his tremendous help on this work.

I am thankful RNDr. Jiří Svoboda, PhD for his ideas and helpful comments, for showing me the ropes of data analysis and the applications of my work.

I want to thank Andrea Gnarini, Lorenzo Marra and Jakub Podgorný for the numerous discussions, exchanged ideas and help with this work.

A truly special thank you is dedicated to my parents for being my support and cheering me on through my entire life. Knowing that there are no words that could accurately describe the extent of gratefulness I possess, thank you.

A huge amount of gratitude goes in the following ways:

Vittoria Elvezia-Gianolli and Anastasia Yilmaz for your ever-present good mood, support and strength when I needed it. For keeping me sane. Thank you for being my friends.

Azade Ghannad and Raul Ciancarella for all the mental support, especially during the period of writing this thesis, for your help and strength, good mood and a bunch of jokes when I needed it. For creating a safe space for me. Thank you.

Inga, Katya, Andrejka, Lydka, Katka and Abhijeet for your everlasting support and creating a place I always look forward returning to. Thank you for being my friends. I wish I knew all of you earlier.

Marcel, for all the shared laughs, light-hearted conversations, encouragement and your wonderful spirit;

Peter, for the help and explanation when needed, for your wonderful personality and cheering me on. For being you. Thank you.

Zuska, the person who's been in this with me for as long as I can remember, for sitting in the first row of this roller-coaster ride for all this time and not having decided to tap out;

Baška, Miloš, Ninka and Vanes for being friends, for backing me up and checking up on me;

I am tremendously grateful to everyone in the Room 81 & Acquario, especially Francesca, Filippo, Cintia, Simone, Marco, Andrea, Ivano, Massimo, Giulia, Lorenzo, Vittoria, Rita, Alessio R., Gabriele, Daniele, Raul and Sacha. It's been wonderful sharing my ups and downs with you.

Jay, for your hope, support, but most of all, for your kindness. Thank you for being my friend.

Dheeraj, for your kindness and friendship. For making this world a beautifully better place by being you. Thank you.

Sudip, for your optimism, great laughs and for the words of comfort anytime I needed;

Daniel, for your support and the strength you gave me. You've helped in ways you are not aware of. Thank you.

all the beautiful people at the Villa Maraini Foundation that I have had the privilege of getting to know;

Mrs. Barusová and Mr. Meleg for showing me the beauty of science, giving me solid foundations to build on, for the motivation and comfort you provided me with, for giving me the courage to pursue the career of a scientist;

Grams, for your encouragement and love, for showing me how to be my own friend, for inspiring me to be the best version of myself, for being my hero, for the immensely inspirational strength and hope. For making me believe I can do anything I set my mind to. For your resilience. For carrying a little bit of heaven in your pockets every day and anywhere you go. Thank you.

I am thankful to #AcademicChatter for help, support, great ideas and helpful

tips throughout my PhD journey;

last, but not least, I have a special thank you reserved for my family, friends and mentors that have been supporting me through the entire period of my studies.

Abstract

X-ray polarimetry represents a new tool for studying astrophysical sources, which became possible thanks to the new mission - the Imaging X-ray Polarimetry Explorer (IXPE) launched on December 9, 2021. Observations of several X-ray binary systems containing either a black hole or a neutron star have been a top priority during the first year of IXPE operations. In this thesis, we focus on both types of X-ray binary systems with the aim of studying different physical aspects.

In the first part, we focus on an XRB containing a black hole - GRS 1915+105. The primary occurrence of the source in thermal state makes it the perfect candidate for black hole spin measurements. To credibly assess the source polarimetric properties, we use a multicolor black body emission model accounting for thermal radiation from the disk accretion complemented by self-irradiation of the accretion disk. We simulate observations of GRS 1915+105 with IXPE and study the impact of a constant albedo on the polarization properties of the source. We demonstrate the capabilities of the mission and the precision of the black hole spin constraints. Unfortunately, GRS 1915+105 has been in an obscured state since 2018, and is therefore used as a test source in this study. The results obtained from our analysis are applicable to any bright source in thermal state.

In the second part, we shift our focus on those XRB systems where the compact object is a neutron star. The currently used model for weakly magnetized Neutron Stars in Low-mass X-ray binaries (NS-LMXBs) considers their X-ray spectrum to be composed of two principal constituents: a thermal component in the soft part of the spectrum (below 1 keV) created by a cold and optically thick accretion disk and a hard one originating in a hot environment of optically thin plasma in the source corona. In the western-like model (White et al., 1988) the hot photons emitted by the NS are observed directly and described using a black-body profile, while a corona obscures the accretion disk and is responsible for Compton scattering of the photons coming from the disk. On the other hand, the eastern-like model (Mitsuda et al., 1984, 1989) considers a reversed scenario with the NS population being almost fully Comptonized due to the presence of corona, and the accretion disk is observed directly as a blackbody. In our study, we assess the differences between these two models by analyzing the spectra of the three weakly magnetized NS-LMXB sources to be observed by IXPE in the first year of operation: GS 1826-238, Cygnus X-2 and GX 9+9 observed by the NuSTAR telescope in June 2014, January 2015 and April 2019, respectively. The aim of these studies was also to provide input parameters for Monte Carlo simulations of the polarization characteristics of these sources, which help interpreting the IXPE results.

List of publications

Published

X-ray Polarimetry as a Tool to Measure the Black Hole Spin in Microquasars: Simulations of IXPE Capabilities

Authors: *R. Mikušincová, M. Dovčiak, Michal Bursa, Niccolò Di Lalla, Giorgio Matt, Jiří Svoboda, Roberto Taverna, Wenda Zhang*

MNRAS, 2023, 519, 6138, doi: 10.1093/mnras/stad077

Accretion geometry of the neutron star low mass X-ray binary Cyg X-2 from X-ray polarization measurements

Authors: *R. Farinelli, ... , R. Mikušincová, ...*

MNRAS, 2023, 519, 3681, doi: 10.1093/mnras/stac3726

Polarization properties of the weakly magnetized neutron star X-ray binary GS 1826-238 in the high soft state

Authors: *F. Capitanio, ... , R. Mikušincová, ...*

ApJ, 2023, in press, doi: 10.48550/arXiv.2212.12472

Submitted

The high polarisation of the X-rays from the Black Hole X-ray Binary 4U 1630–47 challenges standard thin accretion disc scenario

Authors: *A. Ratheesh, ... , R. Mikušincová, ...*

The First X-ray Polarization Observation of the Black Hole X-ray Binary 4U 1630–47 in the Steep Power Law State

Authors: *N. Rodriguez Cavero, ... , R. Mikušincová, ...*

The first X-ray polarimetric observation of the black hole binary LMC X-1

Authors: *J. Podgorný, ... , R. Mikušincová, ...*

X-ray polarimetry and spectroscopy of the neutron star low-mass X-ray binary GX 9+9: an in-depth study with IXPE and NuSTAR

Authors: *F. Ursini, ... , R. Mikušincová, ...*

In preparation

Coronal properties of weakly magnetized neutron stars in LMXBs

Authors: *Romana Mikušincová, Andrea Gnarini, Giorgio Matt, Francesco Ursini*

Conferences with active participation

07/2020 **EAS**, Virtual conference

Oral contribution: X-ray polarimetry as a tool to measure the black hole spin in microquasars: simulations of IXPE capabilities

09/2021 **The 9th Microquasar Workshop: Celebrating over 50 years of discovery**, Cagliari/Virtual conference

Poster contribution: Measuring black hole spin of GRS 1915+105 in thermal state including self-irradiation of accretion disk

05/2022 **1st Mondragone Frontiers of Astronomy Series**, Monte Porzio Catone

Oral contribution: X-ray polarimetry as a tool to measure the black hole spin in microquasars: simulations of IXPE capabilities

06/2022 **Ten years of High-Energy Universe in Focus: NuSTAR 2022**, Cagliari

Oral contribution: Coronal properties of weakly magnetized neutron stars in LMXBs

07/2022 **From the Dolomites to the event horizon: sledging down the black hole potential well**, Sesto

Oral contribution: X-ray polarimetry as a tool to measure the black hole spin in microquasars: simulations of IXPE capabilities

09/2022 **31st Texas Meeting**, Prague

Oral contribution: X-ray polarimetry as a tool to measure the black hole spin in microquasars: simulations of IXPE capabilities

09/2022 **CNOC**, Cefalù

Oral contribution: X-ray polarimetry as a tool to measure the black hole spin in microquasars: simulations of IXPE capabilities

10/2022 **RAGtime**, Opava

Oral contribution: X-ray polarimetry as a tool to measure the black hole spin in microquasars: simulations of IXPE capabilities

Prologue

Listen; there's a hell of a good
universe next door: let's go.

e. e. cummings

X-ray polarimetry has long been recognized as a valuable technique to investigate the nature and emission properties of most classes of X-ray sources. Prominently among them are X-ray binaries (XRB), where a compact object (either a black hole or a neutron star) accretes matter from a companion star. After the pioneering experiments in the '70s, which led to the discovery of the X-ray polarization of the Crab Nebula (Weisskopf et al., 1978), no polarimeters were put on board X-ray satellites till the recent launch of the Imaging X-ray Polarimetry Explorer (IXPE), which re-opened, after more than four decades, the X-ray polarimetry observing window. IXPE is providing a wealth of new and interesting results on many classes of X-ray sources, including XRB. A polarimeter is also foreseen to be on board of the enhanced X-ray Timing and Polarimetry mission (eXTP) (Zhang et al., 2016) - to be launched by the end of the decade. In this thesis, some aspects of the physics of X-ray binaries which can be studied by X-ray polarimetry will be discussed.

Regarding accreting black holes in X-ray binaries, it should be recalled that Astrophysical black holes are characterized by only two quantities: its mass and angular momentum (spin), as its electric charge is supposed to be negligible. While the mass is often reasonably well estimated by means of various techniques, measurements of the spin are much more uncertain. Different methods are currently used in order to determine the black hole spin in X-ray Binaries. Close to the horizon of the black hole, strong gravity effects takes place and manifest themselves by a broadening of the iron line emitted in the accretion disc (e.g. Fabian et al. (2000); Reynolds (2013)). The closer to the source, the larger the broadening effect will be. Due to the relation between the radius of the Innermost Stable Circular Orbit (ISCO) and the spin, the latter can be estimated. Another widely used method resides in analysing the thermal spectrum of a source. During the process of accreting matter onto a black hole, a vast amount of radiation in the form of thermal energy is released. Similarly to the previous case, the closer to the source, the higher energies are produced (McClintock et al., 2006; Narayan et al., 2008; McClintock et al., 2011). These two

techniques, however, sometimes provide inconsistent results. A third method is based on relativistic precession in KHz QPOs, but so far it has been possible to apply only in a small number of sources, and in the best studied case, GRO J1655-40, the results are at odds with those of the other two methods (Motta et al., 2014). These issues give rise to a desire for a new, completely independent black hole spin constraining technique. X-ray polarimetry offers such a method for accreting stellar-mass black holes in soft state. In fact, strong gravity effects modify the polarization properties of radiation emitted by the disk, with, in particular, a rotation of the polarization plane. The effect is larger at small radii, where the emitted radiation is also harder. As a consequence, a variation of the polarization angle with energy is expected (Connors et al., 1980; Dovčiak et al., 2008; Li et al., 2009). In addition, X-ray polarimetry can help addressing the problem of the geometry (and hence its nature and origin) of the coronal emission in sources in hard state (e.g. Zhang et al. 2022).

Weakly magnetized neutron stars in accreting low mass X-ray binaries represent another highly interesting type of astrophysical object. The neutron stars in these sources are believed to be accreting mass from their companion star through a Roche lobe. Such objects are known for their high variability on a timescale of a few milliseconds to years. The observed emission is composed of two main components: a thermal emission, such as either a blackbody originating on the surface of the NS or the boundary layer, or a multicolor emission produced by the accretion disk; and the second one being the hard component originating as a result of Compton-scattered soft photons on a corona consisting of a hot electron plasma. Two models are currently used to describe the spectral shapes observed in such sources. The Eastern-like scenario (Mitsuda et al., 1984, 1989) supposes the corona to be surrounding the neutron star and Comptonizing the emitted photons, while the disk is observed as a blackbody. The other model - Western-like - represents a reverse scenario (White et al., 1988), in which the disk photons are Comptonized by the corona surrounding the disk, and the neutron star is modeled as a blackbody. Both of these models assume two different blackbody populations of photons and one single Comptonizing region (corona). Although these two models were proposed over 30 years ago, it is still not yet clear which of them is the correct one, realistically modeling these systems. The main reason for this ambiguity is a strong spectroscopic degeneracy. There is even a possibility, that both the soft components get scattered by the corona (Cocchi et al., 2011). From the studies published so far, it seems that the first of these models is favored (Done et al., 2007). It is thanks to X-ray polarimetry, and especially the IXPE telescope, that we could be provide further information on the neutron star low-mass X-ray binaries. In fact, polarimetry is very sensitive to the geometry of the corona. Studying polarimetric properties of this kind of sources will be of a great help in resolving the coronal geometry and its properties.

The aim of my PhD research project is manifold. As a large part of the work

was done before IXPE observations were available, most of the activity concerned preparatory work. In particular, the feasibility of IXPE measurements for estimating the black hole spin was assessed. Regarding the NS XRB, the *NuSTAR* spectra of the sources to be observed with IXPE were analysed, to provide inputs for Monte Carlo simulations of the polarization properties of such systems. Fortunately, before the completion of this thesis a number of IXPE observations were actually performed, and the main results will be briefly presented.

This thesis is structured as follows: in the first chapter we outline the physics of accreting X-ray binary systems, their classification, spectral components and spectral states with specifications of transitions between them, and the contribution of X-ray polarimetric studies in this field. Next, we present results of simulated observations of a black hole XRB system GRS 1915+105 with the aim to study the black hole spin measurements with IXPE. Although the analysis was performed considering GRS 1915+105, which is currently unobservable, the results are applicable for all bright sources in thermal state. In the third chapter we present a spectral analysis of NS-LMXB systems focused on assessing the spectral components of such systems, underlining their importance in order to interpret polarimetric observations of such sources. In the fourth chapter we briefly summarize the polarimetric properties of the XRB sources that were observed by IXPE during its first year of operation. In Conclusions, we summarize the main results and future prospects of this work. Last, there is an Appendix describing the two missions - IXPE and *NuSTAR* - the data of which we used in this work.

Contents

List of publications	ix
Conferences with active participation	xi
1 X-ray Binary Systems and basic physics	1
1.1 What are XRBs?	1
1.1.1 Classification of X-ray Binaries	2
1.1.2 Spectral components	3
1.2 Black Hole XRBs	9
1.2.1 Spectral states and state transitions	10
1.3 Neutron Stars XRBs	13
1.4 Contribution of X-ray polarimetry to XRB	16
1.5 Stokes	19
2 Polarimetry of GRS 1915+105 in soft state with returning radiation	27
2.1 Polarization features from black hole accretion disk	30
2.1.1 KYNBB code	30
2.1.2 KYNBBRR code	31
2.1.3 Energy dependence of polarization features	32
2.2 Results	36
2.2.1 KYNBB	37
2.2.2 KYNBBRR	41
2.3 Discussion and conclusions	42
3 Neutron Stars - LMXB	45
3.1 Introduction	45
3.2 Studied sources	46
3.2.1 Methodology	47
3.3 Results	50
3.3.1 GS 1826-238	50
3.3.2 GX 9+9	50
3.3.3 Cyg X-2	54
3.4 Discussion and conclusions	62

4	IXPE observations of X-ray binaries	71
4.1	Black Hole X-ray Binaries	71
4.1.1	Cyg X-1	71
4.1.2	4U 1630-47, LMC X-1, Cyg X-3	72
4.2	Neutron Star Low-Mass X-ray Binaries	73
4.2.1	GS 1826-238	73
4.2.2	Cyg X-2	74
4.2.3	GX 9+9	75
5	Conclusions and future prospects	77
	List of Figures	89
	List of Tables	95
	Bibliography	97
		113

Chapter 1

X-ray Binary Systems and basic physics

We are all in the gutter, but some of us are looking at the stars.

Lady Windermere's Fan
Oscar Wilde

1.1 What are XRBs?

X-ray Binary systems consist of a compact object (a black hole, neutron star or a white dwarf) and a companion star. These two objects orbit around the common center of mass. In the case that they are close enough, mass from the companion star is being accreted onto the compact object and in this process may create a disk-shaped structure called the accretion disk. During the process of accretion, the mass in the disk changes its kinetic energy to thermal, which is radiated away. The material compounding the accretion disk reaches high temperatures, reaching usually $\approx 10^7 K$ and is caused by the friction in the disk. These systems are among the brightest x-ray sources in our Galaxy.

Microquasars

In this thesis we focus on a specific type of XRB system, called microquasars. A microquasar is a scaled-down quasar and these two sources share some common characteristics. Among those are: a very powerful emission in the radio waveband, that can be observed in a form of a radio jet, and the accretion disk surrounding a compact object. In this case, such a compact object is either a black hole or a neutron star. Unlike in the case of quasars, where the central compact object reaches the mass of millions to billions Suns (therefore, referred to as supermassive), the compact objects in microquasars can reach only a few times the solar masses. The

mass in the accretion disk comes from a companion star (also referred to as a donor) and the accretion disk tends to be reaching very high luminosities both in the optical and the x-ray wavebands. Some fraction of the emission coming from these sources originates in the relativistic jets, and for these reasons are often denoted as radio-jet x-ray binary. The jet is not present in all of the microquasars.

1.1.1 Classification of X-ray Binaries

X-ray binary systems can be sorted into different categories depending on different criteria:

The compact object

An X-ray binary can carry one of three kinds of compact objects: a white dwarf, a neutron star or a black hole. Based on what kind of a compact object is present in the system, the X-ray binary can be either a cataclysmic variable (e.g. V407 Cyg), a neutron star X-ray Binary (e.g. Cygnus X-2), or a black hole X-ray binary (e.g. GRS 1915+105), respectively.

The companion star

X-ray binary systems can be divided into two different types based on the mass of the companion star. Those are:

- **High Mass X-ray Binary (HMXB):** these systems are composed of a compact object that can be either a magnetized neutron star with its magnetic field of $\sim 10^{12}$ Gauss, or a black hole. The companion star is an early type star (usually O or B type) with a mass $\geq 10M_{\odot}$. The accretion disk in these type of systems is usually formed by capturing matter ejected from the companion star in a stellar wind. Among the discovered Galactic black hole HMXB sources are for example Cyg X-1 and Cyg X-3.
- **Low Mass X-ray Binary (LMXB):** LMXB sources harbor a neutron star or a black hole as a compact object, while the companion is a usually a K or M type star or a white dwarf of mass $\leq 1M_{\odot}$. Both the compact object and the donor star are very close to each other. In such a composition, the star will fill a Roche Lobe and the accretion onto the compact object occurs through its overflow, during the process of which, an accretion disk is created. In the LMXB systems, we have observed various kinds of variable behavior, such as X-ray outbursts (these are believed to be activated by instabilities in the accretion disk (Lasota, 2001)). In such a case, the source can increase its luminosity a thousandfold and jets might be produced (Tetarenko et al., 2017).

Persistence

X-ray binary systems can be either persistent (such as Cygnus X-1), or transient (such as 4U 1630-47). In the former case the luminosity, albeit usually highly variable, is always high, while in the latter case the source spent most of the time in a very low luminosity state (quiescence), going into outburst from time to time.

1.1.2 Spectral components

Now we briefly introduce the components we can observe in the spectra of X-ray binary systems. We discuss the components of XRB systems, as well as the process of mass accretion from the companion star onto a compact object, which is responsible for the phenomenal luminosity of these sources. We can calculate the gravitational potential energy ΔE_{acc} for a source of mass M and radius R :

$$\Delta E_{acc} = \frac{GMm}{R} = \left(\frac{GM}{Rc^2} \right) mc^2 = \eta mc^2 \quad (1.1)$$

where G is the gravitational constant, m is the accreting mass releasing the energy and $\eta = \left(\frac{GM}{Rc^2} \right)$ is the accretion efficiency in the case of spherical accretion. It is obvious from its definition, that the accretion efficiency depends on the compactness of the accreting object (M/R) and the larger this ratio, the higher the accretion efficiency will be. In the case of the sources with a neutron star as the compact object with a mass of $\sim 1.4M_{\odot}$ and a radius of 10 km, the efficiency is 0.3. For a black hole, for which there is no solid surface and spherical accretion is therefore inefficient, the efficiency ranges from 0.06 (for a static black hole) to 0.42 (for a maximally rotating black hole). It is important to note that the luminosity of an XRB source is strongly correlated to its mass accretion rate. Considering the spectral characteristics of XRBs, the radiation coming from these objects consists of emission processes of both thermal and Comptonization nature. In the following, we explain some of the most essential of those processes.

Emission by an optically thick accretion disk

Soft X-ray emission ($\lesssim 2$ keV) generally has a dominant component - thermal emission - originating in the accretion disk. The origins of the accretion model were founded by (Shakura, 1972; Shakura and Sunyaev, 1973) and later elaborated by including relativistic effects by Novikov and Thorne (1973). In this scenario, gas from the companion star falls onto the compact object and creates the accretion disk, which is (according to the cited model) assumed to be optically thick and geometrically thin, and rotating in Keplerian orbits. The properties of an optically thick, geometrically thin accretion disk is further discussed in Chapter 2.

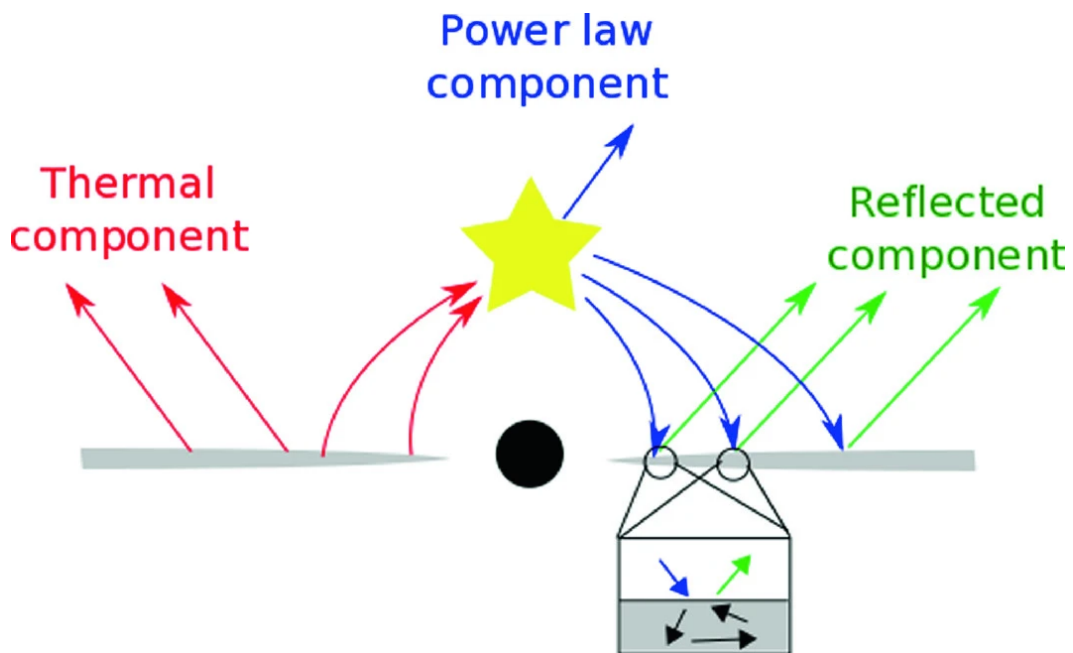


Figure 1.2. The disk-corona model for an accreting X-ray binary system containing a black hole as a compact object. The XRB contains an optically thick accretion disk described by a multi-color blackbody spectrum (red arrows). The direct contribution from the disk is thermal. However, some of the thermal photons scatter on the electrons in the corona, where they get Compton scattered and produce a power-law (represented by blue arrows), which irradiates the accretion disk and results in the reflection component (green arrows). Figure credit: Nampalliwar and Bambi (2020).

Comptonization

Some sources contain a hot cloud of electrons, named the corona (Sunyaev and Titarchuk, 1980; Syunyaev et al., 1991; Tanaka and Shibazaki, 1996). This component presents itself in the spectrum of an XRB as a power-law emission with a high-energy cut-off, which originates due to Comptonization of seed thermal photons from the accretion disk on the corona (see Figure 1.2). While the geometry of the corona still remains unknown, several models have been proposed, as shown in Figure 5.2. Among the first considered models is a "lamp post" geometry, where the corona has a shape of a single point above the center of the accretion disk (Róžańska et al., 2002). Some of the recent models tend to assume that corona might be the base of the radio jet [Skipper 2013] or in an optically thin part of the accretion flow (referred to as extended corona). Novel studies tend to prefer the latter geometry (Chauvin et al., 2018).

X-ray reflection and relativistic effects

Reflection features represent another very important and remarkable attribute of the XRB spectrum. The reflection features are composed of by two main components,

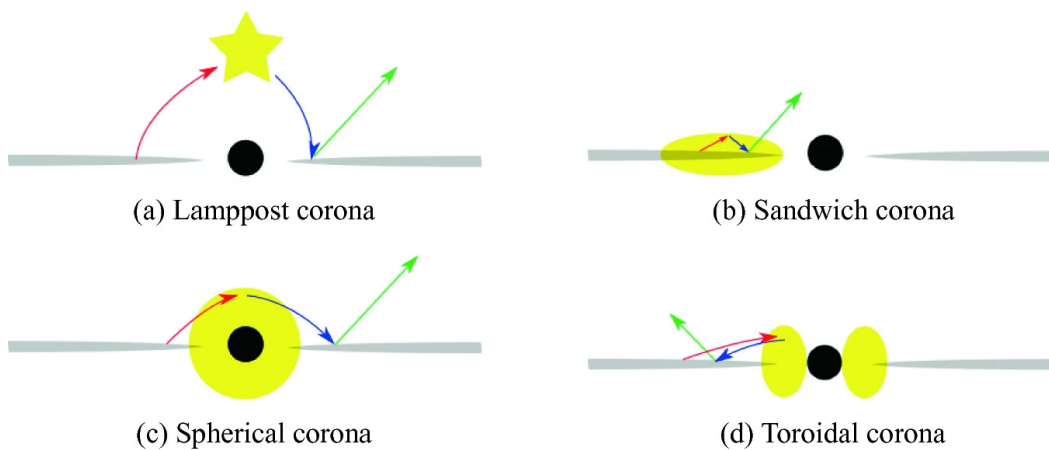


Figure 1.4. Illustration of corona geometry models: lamppost model (a), sandwich model (b), spherical model (c) and toroidal model (d). Figure credit: Nampalliwar and Bambi (2020).

iron emission lines at $\sim 6.4\text{--}7$ keV depending on the ionization state) and a broad Compton hump at ~ 30 keV.

- **Iron emission line:** A very typical component present in the reflection spectrum is the iron $K\alpha$ line present at energies ranging from ~ 6.4 keV (neutral iron) to 6.96 keV (H-like iron). The production of fluorescent emission lines occurs during the process of radiative de-excitation of atoms that previously absorbed X-ray photons. When hard X-rays illuminate atoms, most of the time they get absorbed via ejection of an electron in the K-shell in iron (or other element with a high Z , that has a high abundance in the matter in the accretion disk). After this process takes place, the K-shell of the atom is filled by an outer electron, while releasing energy equivalent to the K-shell fluorescent line. The most noticeable feature of the reflection spectrum is the Fe $K\alpha$ line, together with a much fainter $K\beta$ line if the ionization state is such that the M shell is not empty (Fabian et al., 1989; Matt et al., 1991; Fabian and Ross, 2010). For He- and H-like iron, for which there are no electrons in the L-shell, the line emission is due to recombination- Of all the elements, iron is of the highest abundance (compared to other heavy elements), therefore, the iron line is very prominent. Most X-ray observatories work with energy intervals that include 6.4 keV, therefore Fe $K\alpha$ lines are ever-present X-ray features observed in the spectra of many XRB systems.

We use the equivalent width to measure the strength of the iron line. The equivalent width depends on the following:

- geometry of the accretion disk
- the elemental abundance of iron

- inclination angle of the source: the observed equivalent width decreases with higher inclination, which is a result of additional absorption and scattering of the photon producing the iron line when leaving the surface of the accretion disk (Ghisellini et al., 1994)
- ionization parameter of the surface of the accretion disk: The ionization parameter ξ is defined as $\xi = 4\pi F_{ion}/n$, where F_{ion} is the density of the irradiating flux and n is the density of the reflector [cite Done 1992]. For $\xi < 100 \text{ erg cm s}^{-1}$ and $500 < \xi < 5000 \text{ erg cm s}^{-1}$ the line is considered strong. Then for $100 < \xi < 500 \text{ erg cm s}^{-1}$ the line is weak and finally, for $\xi > 5000 \text{ erg cm s}^{-1}$ the line is almost absent in the spectrum (Matt et al., 1993)

The broad iron line profile originates as a combination of Doppler and transverse-Doppler shift, beaming and gravitational redshift. On the left panel (a) of Figure 1.5 we see an accretion disk rotating clockwise (the blue part of the disk is moving towards the observer, causing Doppler blueshift, while the red part is moving away from the observer, resulting in Doppler redshift of the radiation coming from the disk). We consider two annuli on the disk, represented by the two dashed lines. Each of the disk annulus creates an emission line. Those are represented on the right panel (b). In the first subpanel we only see the effects of Newtonian physics for a non-relativistic disk. Both the lines are symmetric and double peaked. The effects of transverse Doppler shift together with relativistic beaming are seen on the second subpanel, then the third subpanel shows the impact of gravitational redshift on the emission lines. Lastly, we sum these effects together, which results in a broad and skewed Fe line, which is shown in the last subpanel. In Figure 1.7 we show the spectrum emitted by the NS-LMXB source GX 3+1. There is a clearly visible Fe K emission line profile between 6 - 7 keV with a peak of the line at $\sim 6.4 \text{ keV}$. Clearly, iron fluorescence lines provide a splendid opportunity to study the behavior of matter affected by strong relativity effects. Studying the iron line profile has been the leading method in measuring the spin of black holes in XRBs and AGNs, as the red tail of the line is strongly dependent on the inner edge of the accretion disk, which in turn may depend of the spin.

- **Compton hump:** Reflection due to downscattering processes of the Comptonized power-law photons from the corona causes the origin of a hump in the spectrum of the studied source. The hump is usually located in the range 20 - 100 keV with a peak at $\sim 30 \text{ keV}$ (Fabian et al., 2000). The shape is specifically dependent on the individual effects of the photoelectric absorption of the incident photons and electron scattering.

Figure 1.9 shows the individual components contributing to the spectrum of accreting black holes in the disk-corona scenario. Those are the thermal spectrum of the accretion disk, the corona-induced power-law component and the reflection component caused by the irradiation of the disk by the power-law.

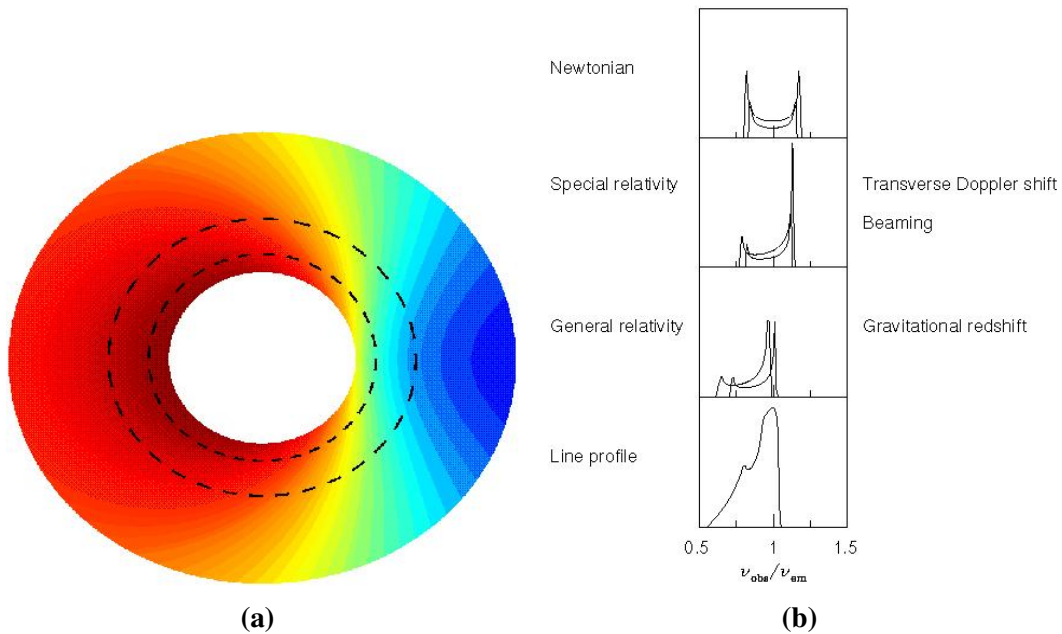


Figure 1.5. The Fe emission line profile. The line profile depends on the contribution from the Doppler and transverse-Doppler effects, relativistic beaming and gravitational redshift. The left panel shows an accretion disk with its right hand side rotating towards the observer and the left hand side away from the observer. Two annuli are marked on the disk. The right panel shows the Fe line profile of these two annuli for a non-relativistic accretion disk (upper subpanel), the transverse Doppler and relativistic beaming considered (second subpanel from top), and redshift (third subpanel). All these effects summed together in the bottom subpanel. Image credit: Fabian et al. (2000).

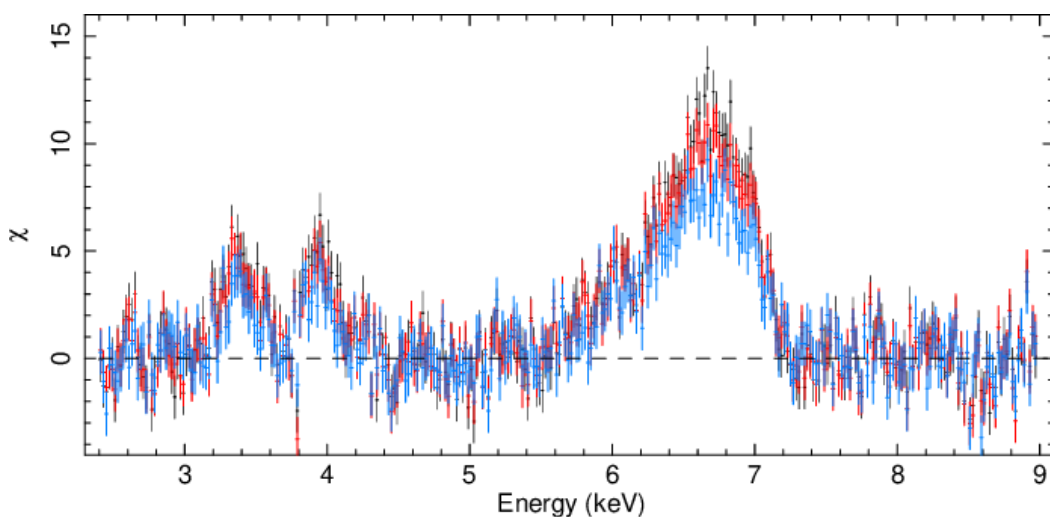


Figure 1.7. An energy spectrum of the NS-LMXB source GX 3+1, analyzed by S.Piraino et al. (2012). Between 6 - 7 keV we see a pronounced iron line.

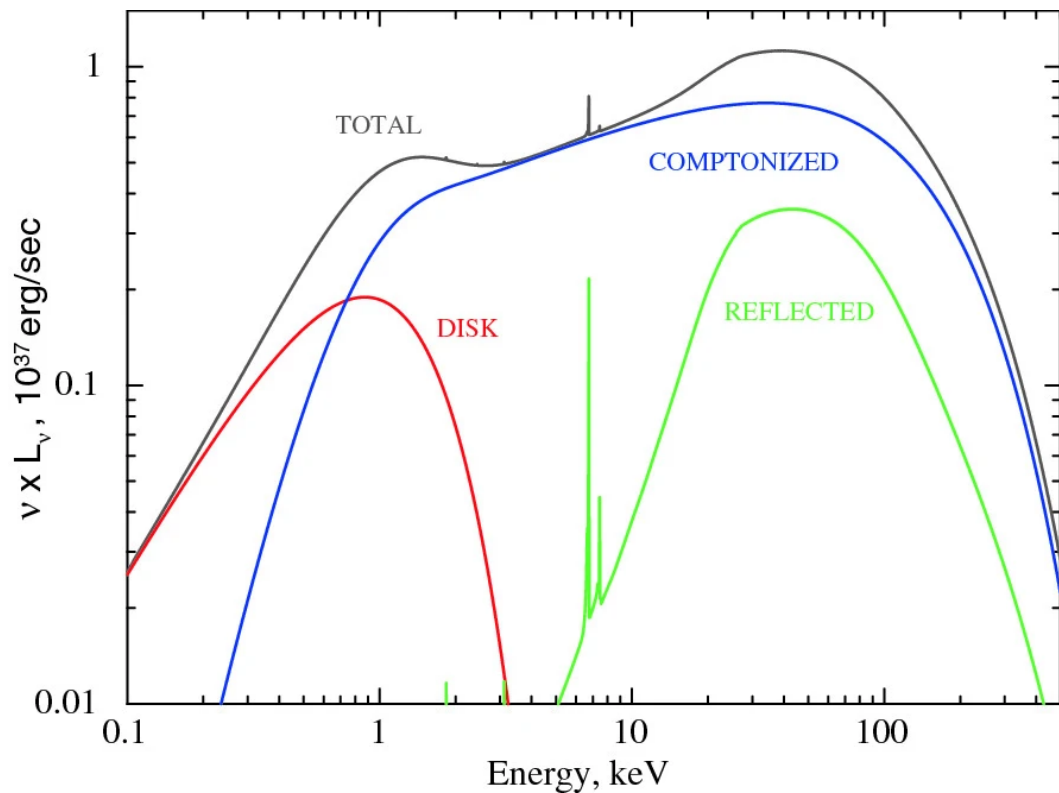


Figure 1.9. Disk-corona model of an accreting black hole in an X-ray binary source. Shown are spectral components: thermal component radiated by the accretion disk (red), power law component originated by the corona (blue) and the reflection component due to the irradiation of the accretion disk by the power law from the corona (green). Image credit: Nampalliwar and Bambi (2020).

Ionized wind

Ionized winds have been studied in the past two decades, as a result of identification of multiple highly-ionized absorbers surrounding accretion disks. Evidence for these absorbers come from the presence of absorption lines, especially Fe xxv and Fe xxvi transitions (Ueda et al., 1998; Kotani et al., 2000). These lines are often blueshifted, which implies that the hot gas is outflowing from the accretion disk, creating disk winds. These winds have been observed XRB spectra, observed in both optical and X-ray energy intervals [Miller 2008]. They are common during the soft state of XRBs, but tend to be missing during the hard states (see below). This would imply that there is a connection between the characteristics of the compact object, presence (or absence) of ejected matter and the state of the inner accretion disk (Ponti et al., 2016; Díaz Trigo and Boirin, 2016).

Relativistic jets

Relativistic jets are collimated outflows of highly energetic plasma relativistically ejected by the X-ray binary systems (Fender, 2006). The inner accretion flow accelerates these outflows and are launched from the accretion disk. Though there is currently no full understanding of how the accretion and ejection phenomena relate, these two are believed to be interlinked Markoff et al., 2003; Fender et al., 2004; Pe'er and Markoff, 2012. The primary mechanism responsible for emission in the radio jets is synchrotron. Currently, there are many open questions regarding the exact origin and collimation of the jets, however, there are models supposing that magnetic field of the accretion disk might be of extreme significance (Blandford and Znajek, 1977; Blandford and Payne, 1982).

1.2 Black Hole XRBs

The black holes are the most compact objects to be found in the Universe. They are remnants of stars with a core mass greater than 8 Solar masses. BHs can be either non-rotating and rotating. The non-rotating ones are described by the Schwarzschild metric, while the latter are described by the Kerr solution. Black holes do not emit per se (apart from the Hawking radiation). However, since the BHs are compact objects, and also among the most extreme sources in the Universe, during the process of accretion the infalling gas from an the accretion disk, which can reach very high temperatures. During this process, the accreting matter creates friction onto itself, which leads to thermal emission, which can be observed in the X-ray energy band.

So far, there have been 18 observed XRB sources which are believed to harbour a stellar-mass black hole. The source black hole typically has a mass in the range of $\approx 7 - 10 M_{\odot}$.

1.2.1 Spectral states and state transitions

Stellar-mass black holes in X-ray Binaries tend to undergo certain spectral states, differentiated mainly by their luminosity and photon index. In the following part of the section, we will be mentioning the typical luminosities of each spectral state relative to the Eddington luminosity. The Eddington luminosity (L_{Edd}) is defined as the maximum isotropic luminosity of a radiating object in hydrostatic equilibrium. In the case of accreting objects, L_{Edd} represents the theoretical isotropic luminosity at which the outward radiation pressure of the gas exactly balances the gravitational pull towards the black hole, supposing spherical accretion, and is given by:

$$L_{Edd} = \frac{4\pi G M m_p c}{\sigma_{Th}} = 1.26 \times 10^{38} \frac{M}{M_\odot} \text{ erg/s} \quad (1.2)$$

where G is the gravitational constant, M is the mass of the compact object, m_p is the proton mass, c is the speed of light and σ_{Th} is Thomson cross-section of an electron. This formula holds for a gas of protons and electron in Coulomb interaction. When we are assuming accreting black holes, we can derive the Eddington mass accretion rate \dot{M}_{Edd} from the Eddington luminosity:

$$L_{Edd} = \eta_r \dot{M}_{Edd} c^2 \quad (1.3)$$

where η_r represents the radiative efficiency of the accretion process, which is 0.06 for a static black hole, and 0.42 for a maximally rotating black hole.

In most sources, the majority of the time is spent by such a source in the quiescent state characterized by a low accretion luminosity, typically of orders $\frac{L}{L_{Edd}} < 10^{-6}$. The black hole will stay in the quiescent state usually for a few months, but also several decades. After the quiescent state, the black hole will achieve a more active state, which starts with a sudden increase in the mass accretion rate from the companion star, accompanied by turning into a brighter state with a typical luminosity $\frac{L}{L_{Edd}} \sim 10^{-3} - 1$. This state is called outburst and lasts until the black hole manages to finish the accretion of the material originated by the outburst and is on typical time scales of a few days to months. The spectrum of the source will change during this phase and this leads to several different emission states. These states (also referred to as spectral) depend on the source luminosity and the extent each spectral component contributes to the overall spectrum during the different phases of the outburst. The two major actors in this scenario are the thermal disk blackbody emission and the Comptonized power-law emission. Each of these components will be the dominant component in different spectral state, which can contribute in recovering geometry of a studied source. There have been some proposed theories correlating the spectral states with the accretion flow. However, it is not well understood whether there is any correlation, and since the spectral states classification is fully phenomenological, we can stick to a better understood theory.

When describing the outburst of a black hole XRB, it comes handy to use the

Hardness-intensity diagram (HID, Fender et al. (2004)). Such a diagram represents a model for the correlation between the hardness of the source (on the x axis) and its luminosity (y axis). The HID depends on the individual source, as well as the telescope used for its observation. The HID is usually represented by a 'q' - shaped path during the evolution of the source throughout the outburst (Fender et al., 2004). Every source follows the HID (also referred to as the 'q' - diagram) in the counter-clockwise direction and will follow its own specific path and outbursts. Figure 1.11 shows a Hardness-intensity diagram. We start from the right bottom panel, where we see two vertical lines (points A to B, and E to A). The first one (A - B) identifies the "hard branch" corresponding to the low/hard (LHS) spectral state. When the behavior of the source changes from quiescence to outburst or vice versa, we observe the LHS. The branch on the very left (C - D) represents the high/soft state (HSS). The two horizontal lines (B - C and D - E) are called the intermediate state and describe the two transitions between the LHS and HSS. Source will be characterized by different flux value at each of these two branches. Each source shifts through the HID in the counter-clockwise direction. The transition from the LHS to HSS happens at a higher flux value. On the other hand, the reverse transition back to LHS happens at a distinctly lower flux level. Finishing the path through the HID is referred to as a hysteresis cycle (Miyamoto et al., 1995). In the following, we briefly describe the major features of each spectral state.

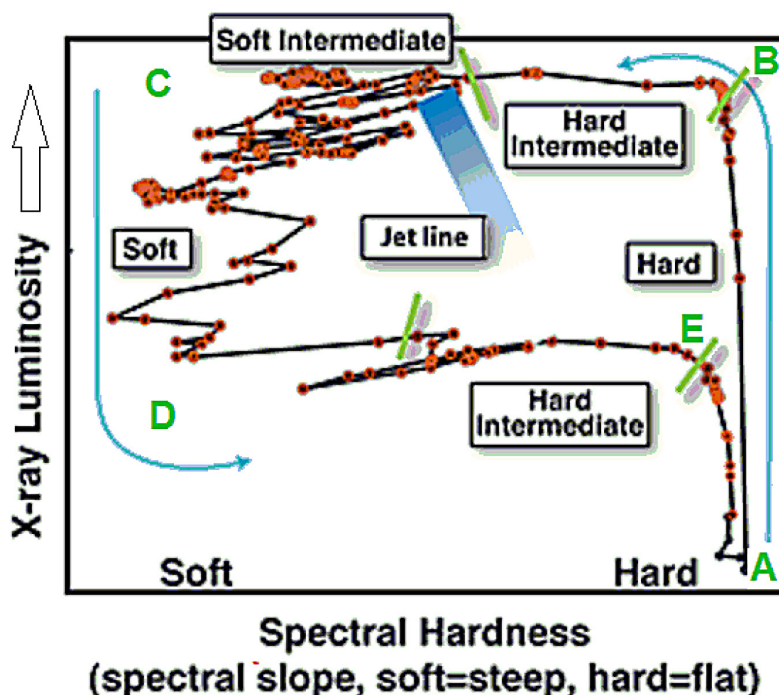


Figure 1.11. Portrayal of the typical q-shaped track that X-ray binary systems with a black hole trace throughout their evolution through various spectral states in the hardness-intensity diagram (HID). Figure credit: Kylafis et al. (2012).

As a source evolves through the hardness-intensity diagram, we can distinguish two primary spectral shapes (see Figure 1.13). We can directly observe from the figure two main spectral components, which are the broad thermal emission in the soft X-rays and the power-law with high-energy cut-off in the hard X-ray part of the spectrum. In order to distinguish between these two types of spectrum, it is common to use the power-law photon index Γ (in the part of the spectrum with no energy cut-off) (Homan and Belloni, 2005; Remillard and McClintock, 2006).

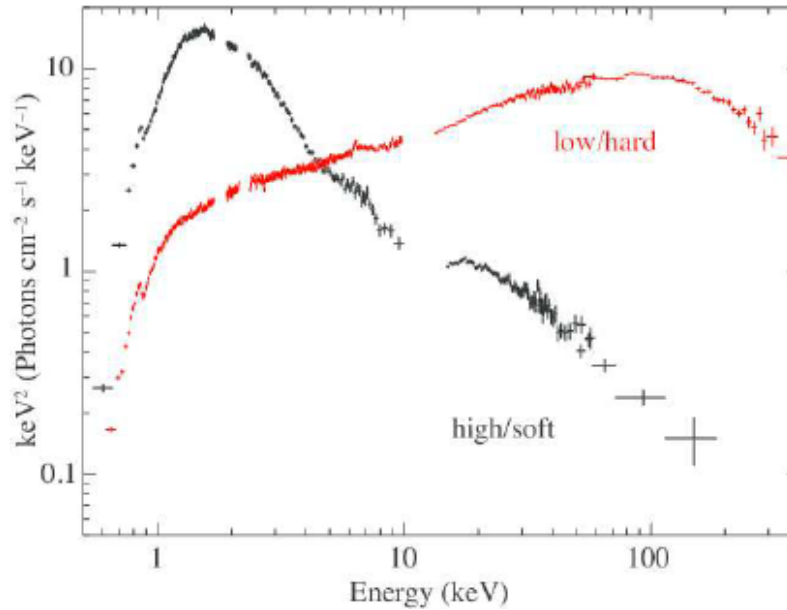


Figure 1.13. Spectral shapes of an X-ray binary system containing a black hole Cyg X-1 in the low/hard state (red) and the high/soft state (black). Figure credit: Yamada et al. (2013).

Low/Hard State

We begin by describing the characteristics of the Low/Hard State, which is the state the BH in an XRB occurs in at the start and end stage of the outburst. We can observe hard emission coming from the source, which are dominant in the higher energy of the spectrum. The X-ray spectrum is predominantly a power-law emission with a high-energy cut-off. Typical power-law photon index in this stage is $\Gamma \sim 1.4 - 2.1$. Another dominant spectral component is reflection characterized by the presence of a broad iron line at ~ 6.4 keV and Compton hump at ~ 30 keV, while the disk contribution is not as dominant. Presence of a radio jet is also characteristic for a source in the LHS. Luminosity of sources in LHS tends to moderately increase until its maximum, when the spectrum begins to become softer and the source forwards to High/Soft State. Sources such as Cygnus X-1 are most commonly occurring in this state.

Intermediate State

The source passes through the intermediate state when it transits between the LHS and the HSS. The hard power-law component will abruptly rise. Moreover, the thermal accretion disk will increase its flux during the state. These two phenomena will cause the spectra to be softer than in the LHS. We can distinguish two different states within the intermediate state: the hard intermediate state (HIMS) and the soft intermediate state (SIMS). The HIMS is responsible for the major portion of the horizontal tracks between the LHS and HSS. It arises after the initial LHS and then again just before the source transitions back to LHS at the end of the outburst. Alternatively, soft intermediate state has softer spectrum, which means in the HID, this state is located on the left from HIMS. HIMS will also present with a more prominent high-energy cut-off than SIMS. However, the soft X-ray spectra of both these states are very much alike.

What is of utmost interest, is the transition between the hard intermediate state and soft intermediate state. This transition is accompanied by the ejection of relativistic (ballistic) jets. The radio jet disappears and in exchange, a ballistic jet is observed. It is common for many XRB sources to spend a substantial time during their outburst in the HSS, which makes them appear as if they wandered back and forth in the hardness-intensity diagram. This is accompanied by shimmering of their radio jet.

High/Soft State

On the very left side of the HID, there is a vertical line representing the high-soft state. Source transitions to this state after passing through the hard and intermediate states. The spectrum of a source in the HSS is dominated by emission from an optically thick and geometrically thin accretion disk (Novikov and Thorne, 1973), which results in a soft spectrum. Typically, the spectrum is characterized by a thermal disk emission, together with a sporadic steep power-law with a photon index of $\Gamma > 2.1 - 2.4$.

1.3 Neutron Stars XRBs

Accretion-powered neutron stars are an important class of X-ray sources. In this thesis, we specifically focus in accreting, weakly magnetized neutron stars in low-mass X-ray binary systems (NS-LMXBs). They are some of the brightest observable X-ray sources. Their luminosity reaches $10^{36} - 10^{38}$ erg/s. The stellar-companion forms a Roche lobe, through which the outflow provides accretion on the NS. The donor star in these systems is usually a Main Sequence star with a relatively low mass, typically lower than the mass of the Sun. It is not uncommon for the companion star to be a dwarf evolved object. The NS-LMXB are extremely variable sources, which oftentimes vary even throughout one observation.

NS-LMXB sources are classified on the basis of the properties they present in their spectra and timing observations into two main groups the names of which have an origin depending on the shape they trace in the color-color diagram (CCD) (Hasinger and van der Klis 1989; van der Klis 1995). Figure 1.15 shows such a color-color diagram for two types of sources, namely the Atoll and Z sources. The distinction is such that atoll sources have low magnetic field and accrete at extremely low mass accretion rates compared to the Z-type NS.

There are currently $O \sim 10$ known Galactic NS-LMXBs classified as a Z-type. All of them accrete near the Eddington limit and are NS-LMXB sources with the highest luminosity in the Galaxy. In the right panel of the Fig. 1.15 we see a shape of the letter "Z", which is the track that these sources trace in their CCD. This track is derived into three branches, named the Horizontal (HB), Normal (NB) and Flaring (FB) going from top left to the bottom right. Each branch mark a different spectral state of the systems. Z-type sources are extremely variable and can pass the entire CCD in timescales of hours to days. The reason behind such a rapid variation is associated to the changes in the accretion, which causes the source to move in the Z-track from the Horizontal Branch to the Flaring one (Hasinger and van der Klis, 1989). Similar variability is observed also in the radio spectrum, where it seems to be related to the X-ray behavior (Penninx et al., 1988). The radio emission decreases with increasing accretion rate coming from HB (this represents the strongest radio emission from these sources) to FB (weakest radio emission).

On the other hand, Atoll-type neutron star low-mass X-ray binary systems share numerous X-ray spectral and timing characteristics with the black hole X-ray binaries. These type of sources present two X-ray states (hard and soft) based on their position in the CCD (Figure 1.15, left panel). These two states are unequivocally related to the hard and soft states of black holes in XRB sources. The hardest X-ray state (on the left side in the figure) is also labeled as "island", while the softest one is labeled as "banana". The Atoll sources comprise the largest group of the known XRBs, very few have a detection in the radio band, due to their very low radio luminosity (which comprises about 1/30 of that of radio-loud black hole and Z-type neutron star X-ray binary systems (Fender and Kuulkers, 2001; Migliari et al., 2003; Munro et al., 2005; Migliari and Fender, 2006).

Neutron star XRB systems in the hard state (as well as BH XRBs) present with 2 main components in their spectra, those being a thermal component and a Comptonized one (in some cases we also observe a reflection component; in the case on the NS sources self-irradiation of the accretion disk is a negligible feature, because of the larger inner disk radius). There are some models to explain the specific geometry causing the presence of these components. We will introduce the two main models considered in the case of the accreting weakly magnetized neutron star X-ray black hole binary sources:

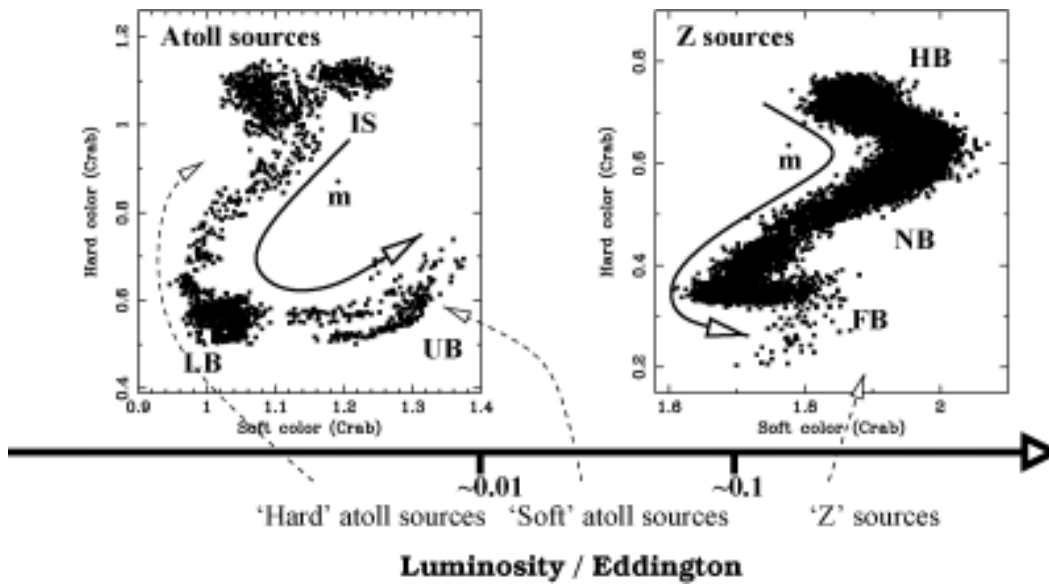


Figure 1.15. Representation of the color-color diagram (CCD) for neutron star low-mass X-ray binary systems. The sources are either Atoll or Z-sources based on the shape of the track they trace in the diagram. Atoll sources are either found in an island state (IS), lower banana (LB) or upper banana (UB). Z-sources trace horizontal branch (HB), normal branch (NB) or the flaring branch (FB). Figure credit: van Straaten et al. (2003) and Jonker et al. (2000).

- **western-like model (WM):** The NS star is observed directly and presents in the spectrum as a blackbody, while the accretion disk is obscured by the corona, which Compton-scatters the photons leaving the disk White et al. 1988. The geometry of this kind of system is pictured in the Figure 1.17
- **eastern-like model (EM):** The Eastern Model represents a reversed scenario from the WM. In this case, we observe the soft component originating in the accretion disk directly as a blackbody spectrum ((Mitsuda et al., 1984), (Mitsuda et al., 1989)). The accretion flow creates a boundary layer (BL) or a spreading layer (SL) around the NS, which prevents the accretion flow from forming a transition layer between the accretion disk and the surface of the neutron star (more specifically, BL points to the gas-decelerating part of the accretion disk, while SL is the layer of gas on the surface of the neutron star). The seed photons radiated from the surface of the neutron star/BL/SL are Comptonized by the corona. In the EM scenario, the corona can either have the shape of a thin belt or a wedge (panel (a) of the Figure 1.18), but can also extend to cover the entire surface of the neutron star (Inogamov and Sunyaev, 1999) (panel (b) of the same figure).

Although in this work we consider such theoretical models, where the photons from only one part of the NS-LMXB system get Comptonized (photons originating either in the disk or the neutron star), there is a possibility that the seed photons from both



Figure 1.17. A representation of a slab coronal geometry considered in the Western-like model, where the disk photons get scattered on the corona surrounding the disk, while the neutron star is observed directly as a blackbody. Image credit: A. Gnarini

the accretion disk and the neutron star get scattered in the corona, as predicted by Cocchi et al. (2011). The exact geometry and specific physical properties of the corona remain unresolved to this day. However, Gilfanov et al. (2003) studied the frequency-resolved spectra of the Atoll source 4U 1608 occurring at high luminosity in the banana state. It follows from their analysis, that the lower kHz quasi-periodic oscillation (QPO) occupies an identical spectral shape, as the boundary layer (i.e. Comptonized) component. Such a swift variability is more likely due the boundary layer, rather than the accretion disk. Therefore, these results highly favor the Eastern Model Done et al. 2007.

1.4 Contribution of X-ray polarimetry to XRB

In this work we focus on two specific issues:

- constraining a black-hole spin and geometry in the soft state
- studying coronal properties in neutron star low-mass X-ray systems in the hard state

In the following, we will describe how X-ray polarimetry can contribute in studying and solving these issues.

Spin of black holes in XRB systems in the soft state

Currently, there are several methods used in order to constrain the spin of black holes (Reynolds, 2019, 2021). In the section 1.1.2 we have described the origin of

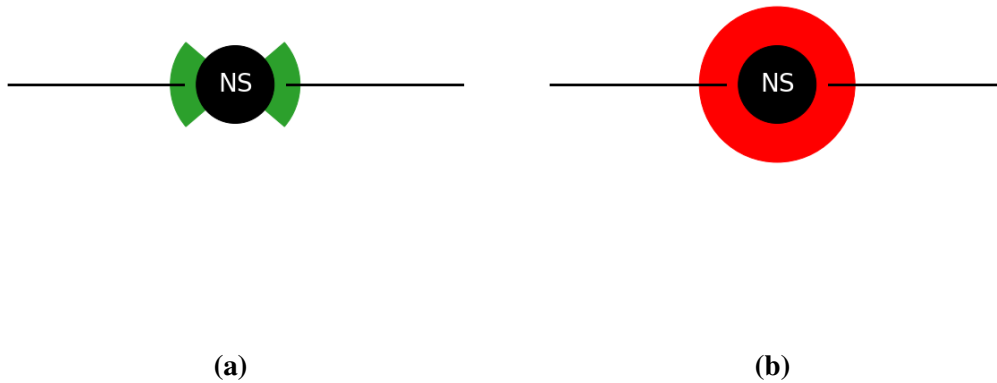


Figure 1.18. Representation of a wedge (a) and spherical (b) coronal geometry in the Eastern-like scenario, with a thermal component from the accretion disk (observed directly) and the seed photons from the neutron star scattered in the corona. Image credit: A. Gnarini.

the iron line. It is possible to constrain the black hole spin based on the broadening of the red wing of this line in the source spectra, which arises as a result of large gravitational redshift close to the black hole horizon (Fabian et al., 2000). Another method - based on kHz Quasi-Periodic Oscillations - arises from the measurement of the relativistic precession frequencies, which depends, among other parameters, on the spin of the black hole (Stella and Vietri, 1999). To be fully applied, three distinct QPOs has to be observed, which to date happened only in one source, J1655-40 (Motta et al., 2014). Last, there is a direct connection between the thermal spectrum and the spin of a BH, which might help in constraining the spin. The inner edge of the accretion disk is located at a specific distance from the BH. For a non- or slowly-rotating black hole (the spin $a = 0$), the inner accretion disk edge is located farther away from the BH, than in the case of the maximally rotating ($a = 1$) one. Moreover, each disk radius radiates at a different energy, which behaves in a way, that the closer to the black hole, the higher the energy will be. Using these two effects together, we should be able to measure the spin of the black hole (Narayan et al., 2008; McClintock et al., 2006; McClintock et al., 2011; McClintock et al., 2013).

However, the first (iron line) and the last (thermal spectrum) methods some time provide us with contradictory results. In the only source for which all three methods have been applied, J1655-40, the three results are inconsistent one another. In the case of the source GRS 1915+105, later studied in the chapter 2, the source presents with a broad iron line at the energy $E = 6.4$ keV, as follows from an analysis by Martocchia et al. (2004). In the study of Blum and Miller (2009), they

used two different methods to study an observation of the source performed by the *Suzaku* satellite: `PEXRIV` for the broadband spectral fitting, and `REFLIONX` in order to account for the soft X-ray energy interval (< 10 keV). The first method resulted in a spin of $a = 0.98$, while the latter gave them the value $a = 0.56$. The first result is consistent with the value obtained by Narayan et al. (2008) (in an analysis of thermal spectrum), however, the second is not. This gives rise to need for a new method that could provide us with the possibility of black hole spin measurement.

In this work, we focus on an XRB system in soft state containing a black hole as a compact object. The system is in the soft state, meaning there is no obscuring medium causing Comptonization (i.e. corona), therefore we observe thermal radiation coming from the source. If we want to measure the BH spin in this system configuration, we need to be very precise in the measurements of the thermal radiation coming from the accretion disk. In order to do that, it is necessary to know the mass of the black hole, the disk inclination and the distance of the source. Unfortunately, these parameters are not always precisely known (for example, it is quite difficult to measure the inclination of the system, as it is correlated with the symmetry of the system).

A method, that could help solve this situation and shed new light on the black hole spin measurement and resolving its geometry, seems to be X-ray polarimetry. Since polarization from a system is very sensitive to its symmetry, we believe to be able to constrain the source inclination. Moreover, since we study thermal radiation (the source is in the HSS), the spectral component dominating the 2 - 8 keV energy band, is coming from the accretion disk. The source of polarization in our model is the scattering of photons on the electrons in the disk. We assume that the scattered photons leaving the accretion disk are impacted by the strong relativistic effects, which will result in the change of the polarization properties in such a way. We will observe rotation of the polarization angle due to the relativistic effects, as the rotation is dependent on the emitting point on the accretion disk. The closer to the black hole the emitting point is located, the higher the resulting rotation. Studying this effect will therefore help us in constraining the black hole spin, in addition to resolving the source geometry.

Geometry of the corona

X-ray binary systems with a neutron star or a black hole as their compact object have been of an interest in astrophysics for decades. A great deal of attention has been pointed towards studying the origin and the physical properties of the Comptonizing region in these systems. Some of the unanswered questions remain whether the corona is located above the accretion disk or between the disk and the compact object; how does the nature of a compact object (event horizon of a BH or a surface of a NS) impact the geometry of the emission region; and how does mass accretion rate impact the properties of the corona.

In the previous section we have presented the current models used to describe the coronal geometry in the NS-LMXB sources, which stay of an outstanding interest in astrophysics - the corona either Comptonizes the photons originating on the surface of a NS/BL/SL, with the thermal component emitted by the disk (EM), or a reversed scenario with the disk component being Comptonized by the corona and the thermal component originating in the NS (WM). A recent study by Long et al. (2022) favors the Eastern Model, as do some other studies by Gilfanov et al. (2003); Revnivtsev and Gilfanov (2006). On the other hand, Revnivtsev et al. (2013) propose a model of a diluted blackbody in order to model the hard spectral component. However, Di Salvo and Stella (2002); Iaria et al. (2020) show that rather than a diluted blackbody, the hard emission is better explained by a Comptonization effect in the source spectra. Thus, the origin and characteristics of the hard component in the spectra of NS-LMXB sources still remain an open discussion. In this context, the method of X-ray polarimetry seems to provide with the solution to these issues and an answer to the geometry and the nature of the coronal properties that spectroscopy cannot solve.

As a matter of fact, polarimetry is sensitive to coronal geometry due to the fact that coronae of different geometry and position will have different temperature, optical depth, position with respect to the compact object and shape (shape impacts the way photons enter and leave the corona). Figure 1.20 illustrates the modeled Zhang et al. 2022 dependence of polarimetric features on the height of the corona for a spherical geometry (lamp-post) for a case of a maximally rotating (spin $a = 0.998$) black hole as a compact object. We notice that using the polarimetric properties of the corona, we can distinguish its height above the black hole in this geometry, since each high presents itself with a different polarization degree and angle in the 2 - 8 keV (which is the energy range of the IXPE detector).

Moreover, the distribution of the electrons in corona impacts the resulting polarization, so polarimetry can help give us a picture on this distribution, and, therefore, the shape of the corona in the XRB system. In Figure 1.22, we show the difference in the PD and PA for the slab (corona surrounding the accretion disk) versus shell (corona is covering the neutron star) geometry. Due to spherical symmetry, shell corona will be depolarized on high energies, while on the low energy interval we will get a contribution from the accretion disk. On the other hand, for the slab coronal geometry, we notice that the scattered accretion disk photons dominate at the lower energies, due to the fact that the disk is cold.

1.5 Stokes

Polarization is a property describing the propagation of electromagnetic waves with respect to the geometrical orientation of their components' oscillations. Electromagnetic waves are, in general, propagation of electric and magnetic field. Polarization

is specified by the behavior of electric field \vec{E} , as defined by Tinbergen (2005). In the case of un-polarized waves, the vector of electric field is random in its direction and strength. However, for the polarized radiation, the electric field vector oscillates in a specific preferred direction. For example, for linear polarization, \vec{E} propagates on the same plane at all times tracing out a sinusoidal curve. Its strength varies according to the frequency of the wave. The angle of the propagation plane is called polarization angle (PA). As another example, we might consider an elliptically polarized radiation. In this case, curve traced by the electric field vector is the shape of an ellipse. Circular polarization with a constant vector of electric field and linear polarization are special cases of elliptical polarization.

Polarization depends on the geometry of the source and its magnetic field properties and may originate in such a case where there is any kind of preferred direction in the system. Asymmetric distribution of the scattering medium induces linear polarization. Scattered emission that reaches the observer may be polarized orthogonal to the scattering plane. The number of photons scattered in the direction given by an azimuthal angle of scattering can be modulated as a square cosine of the given angle and peaks in the direction orthogonal to the direction of polarization. Therefore, if photons are scattered perpendicularly to the incident plane (azimuthal angle equals 90 deg), polarization degree will be 100%. It is possible to constrain the origin of the emission and the matter distribution around the radiating source. Magnetic field accelerates electrons along its field lines to ultra-relativistic velocities and may induce linear polarization up to 70%. Polarization angle for this process is orthogonal to the projection of the vector of magnetic induction on the sky of the observer (Longair (2011)). It is feasible to inspect the nature of the emission process, the direction and intensity of the magnetic field vector, energy of the photons and possibly prove the existence of highly energetic particles.

Stokes parameters

Let us consider a monochromatic wave propagating in the direction \vec{k} . Its vector of electric intensity holds (Rybicki and Lightman, 1979)

$$\vec{E} = E_0 e^{i(\vec{k} \cdot \vec{r} - \omega t)} = (\vec{e}_x \cdot E_1 + \vec{e}_y \cdot E_2) e^{i(\vec{k} \cdot \vec{r} - \omega t)} \quad (1.4)$$

where \vec{e}_x and \vec{e}_y are the base vectors in the direction x or y, respectively, i is a complex unit, \vec{k} is a wave vector, \vec{r} denotes the position vector, ω stands for the frequency of the propagating wave and t is denotes the time at which the wave is observed. E_1 and E_2 are generally complex numbers, which together give us amplitude and phase of the propagating wave.

$$E_1 = \varepsilon_1 e^{i\varphi_1} \quad E_2 = \varepsilon_2 e^{i\varphi_2} \quad (1.5)$$

In the laboratory frame we have:

$$E_x = \text{Re}(\vec{e}_x \cdot \vec{E}) = \text{Re}(E_1) e^{-i\omega t} = \varepsilon_1 \cos(\omega t - \varphi_1) \quad (1.6)$$

$$E_y = \text{Re}(\vec{e}_y \cdot \vec{E}) = \text{Re}(E_2)e^{-i\omega t} = \varepsilon_2 \cos(\omega t - \varphi_2) \quad (1.7)$$

The terms in equations describe an elliptical polarization. However, we cannot determine the real properties of the ellipse based on the measurements in 2 directions since we don't know the orientation of the ellipse. We now consider the major axis frame, as illustrated in the Figure 1.23

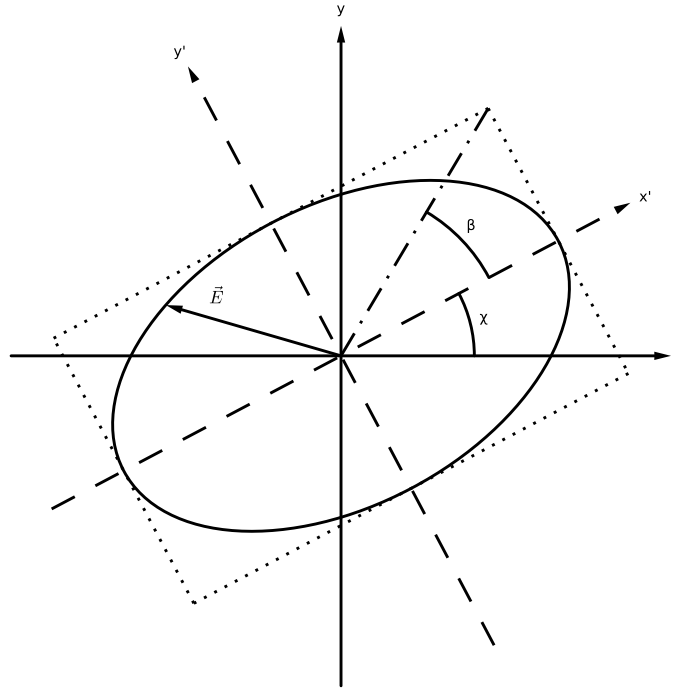


Figure 1.23. Polarization ellipse

and have a new set of equations:

$$E_{x'} = \varepsilon_0 \cos\beta \cos\omega t \quad (1.8)$$

$$E_{y'} = -\varepsilon_0 \sin\beta \sin\omega t \quad (1.9)$$

where β , describing semi-axes $\varepsilon_0 \cos\beta$ and $\varepsilon_0 \sin\beta$, within the interval $\left\langle -\frac{\pi}{2}; \frac{\pi}{2} \right\rangle$ and has the following meaning:

$|\beta| < \frac{\pi}{4}$ the main semi-axis is parallel with x'

$|\beta| > \frac{\pi}{4}$ the main semi-axis is parallel with y'

$|\beta| = \frac{\pi}{4}$ circular polarization

$|\beta| = 0$ linear polarization x'

$|\beta| = \frac{\pi}{2}$ linear polarization y'

$\beta > 0$ clockwise rotation

$\beta < 0$ counterclockwise rotation

We can now write this rotation

$$\begin{pmatrix} E_x \\ E_y \end{pmatrix} = \begin{pmatrix} \cos\chi & -\sin\chi \\ \sin\chi & \cos\chi \end{pmatrix} \begin{pmatrix} E_{x'} \\ E_{y'} \end{pmatrix} \quad (1.10)$$

where χ describes the angle of rotation of the x and y axes. Using this term together with the Equations 1.8 and 1.9 we get

$$\begin{pmatrix} \varepsilon_1 \cos\varphi_1 \cos\omega t + \varepsilon_1 \sin\varphi_1 \sin\omega t \\ \varepsilon_2 \cos\varphi_2 \cos\omega t + \varepsilon_2 \sin\varphi_2 \sin\omega t \end{pmatrix} = \begin{pmatrix} \varepsilon_0 \cos\beta \cos\chi \cos\omega t + \varepsilon_0 \sin\beta \sin\chi \sin\omega t \\ \varepsilon_0 \cos\beta \sin\chi \cos\omega t - \varepsilon_0 \sin\beta \cos\chi \sin\omega t \end{pmatrix} \quad (1.11)$$

which has to be satisfied for any time t . We now get a set of four equations

$$\varepsilon_1 \cos\varphi_1 = \varepsilon_0 \cos\beta \cos\chi \quad (1.12)$$

$$\varepsilon_1 \sin\varphi_1 = \varepsilon_0 \sin\beta \sin\chi \quad (1.13)$$

$$\varepsilon_2 \cos\varphi_2 = \varepsilon_0 \cos\beta \sin\chi \quad (1.14)$$

$$\varepsilon_2 \sin\varphi_2 = -\varepsilon_0 \sin\beta \cos\chi \quad (1.15)$$

Squaring Equations 1.12 - 1.15 and adding them together we get

$$I = \varepsilon_1^2 + \varepsilon_2^2 = \varepsilon_0^2 \text{ the first Stokes parameter}$$

Adding squares of the Equations 1.12 and 1.13 and subtracting squares of Equations 1.14 and 1.15 from them we obtain

$$Q = \varepsilon_1^2 - \varepsilon_2^2 = \varepsilon_0^2 (\cos^2\beta - \sin^2\beta) (\cos^2\chi - \sin^2\chi) = \varepsilon_0^2 \cos 2\chi \cos 2\beta$$

the second Stokes parameter

Now we multiply the Equations 1.12 and 1.14, add product of Equations 1.13 and 1.15 and multiply by 2

$$U = 2[\varepsilon_1 \varepsilon_2 \cos(\varphi_1 - \varphi_2)] = \varepsilon_0^2 \sin 2\chi \sin 2\beta$$

the third Stokes parameter

Finally, we multiply the Equations 1.12 and 1.14, subtract the product of Equations

1.13 and 1.15 and multiply by 2 to obtain

$$V = \varepsilon_1 \varepsilon_2 \cos(\varphi_1 - \varphi_2) = \varepsilon_0^2 \sin 2\beta \text{ the fourth Stokes parameter}$$

These four Stokes parameters satisfy the following

$$\varepsilon_0 = \sqrt{I} \quad (1.16)$$

$$\sin 2\beta = \frac{V}{I} \quad (1.17)$$

$$\tan 2\chi = \frac{U}{Q} \quad (1.18)$$

$$I^2 = Q^2 + U^2 + V^2 \quad (1.19)$$

Generally, I is proportional to the intensity of the radiation, U and Q describe the orientation of the ellipse and are associated with the polarization angle (PA). Finally, V relates to circular characteristics of the wave.

$V = 0$ linear polarization $V > 0$ counterclockwise rotation

$|V| = I$ circular polarization $V < 0$ clockwise rotation

So far, we have only considered coherent waves. However, for a quasi-monochromatic wave, there is a small diversion in frequency. Amplitude and wave vector change after a time period $\Delta t \gg \frac{2\pi}{\omega}$. For radiation in the frequency interval $\Delta\omega$ we observe coherent waves for a short period of time after which the waves get dispersed.

This time interval is called the coherence time and is proportional to $\frac{1}{\Delta\omega}$. We get the Stokes parameters as time-average of the terms we derived for the case of a monochromatic wave

$$I = \langle \varepsilon_1^2 + \varepsilon_2^2 \rangle_t \quad Q = \langle \varepsilon_0^2 \cos 2\chi \cos 2\beta \rangle_t$$

$$U = \langle \varepsilon_0^2 \sin 2\chi \sin 2\beta \rangle_t \quad V = \langle \varepsilon_0^2 \sin 2\beta \rangle_t$$

The Stokes parameters for the quasi-monochromatic wave satisfy a similar condition to 1.19

$$I^2 \geq Q^2 + U^2 + V^2 \quad (1.20)$$

Unpolarized photons are described as follows: $I \neq 0, Q = U = V = 0$. For a completely polarized state we would have $I^2 = Q^2 + U^2 + V^2$. The Stokes parameters are additive, so if we represent them as a vector, we can separate this vector to a unpolarized state and polarized state

$$\begin{pmatrix} I \\ Q \\ U \\ V \end{pmatrix} = \begin{pmatrix} I - \sqrt{Q^2 + U^2 + V^2} \\ 0 \\ 0 \\ 0 \end{pmatrix} + \begin{pmatrix} \sqrt{Q^2 + U^2 + V^2} \\ Q \\ U \\ V \end{pmatrix} \quad (1.21)$$

where the first term on the RHS denotes a unpolarized state and the second term stands for a polarized state.

We define polarization degree (PD)

$$\Pi = \frac{I_{pol}}{I_{total}} = \frac{\sqrt{Q^2 + U^2 + V^2}}{I} \quad (1.22)$$

It is, however, challenging to measure polarization in the case of astrophysical sources, as the net polarization is usually zero. In such case we would need to resolve different regions of the studied objects and observe just these fractions, such as spots or asymmetries in specific parts of the object.

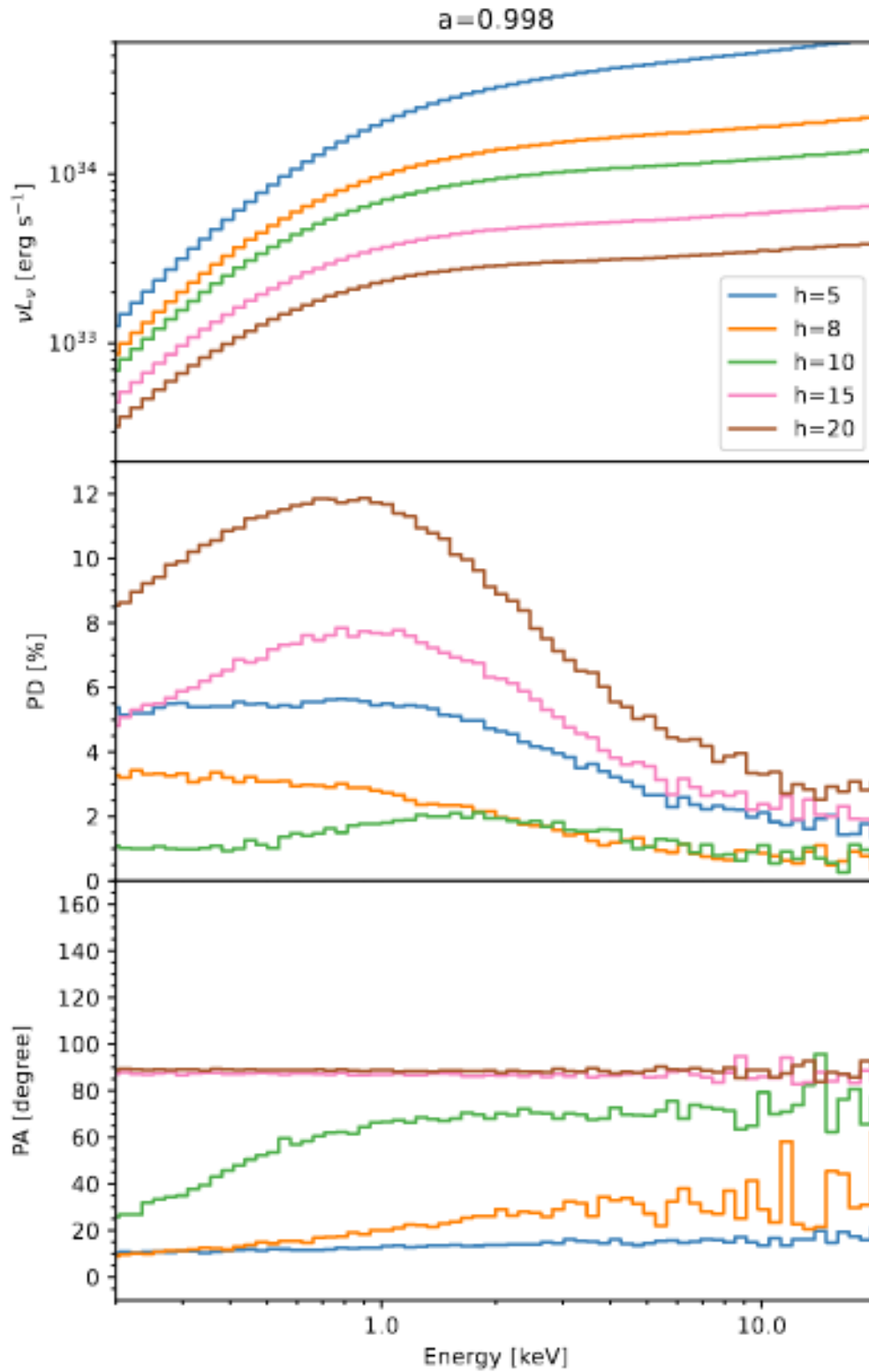


Figure 1.20. Energy dependence of the spectra (top), Polarization Degree (middle) and Polarization Angle (bottom) radiated by a spherical corona. Different coronal height results in different polarization characteristics. Image credit Zhang et al. (2022).

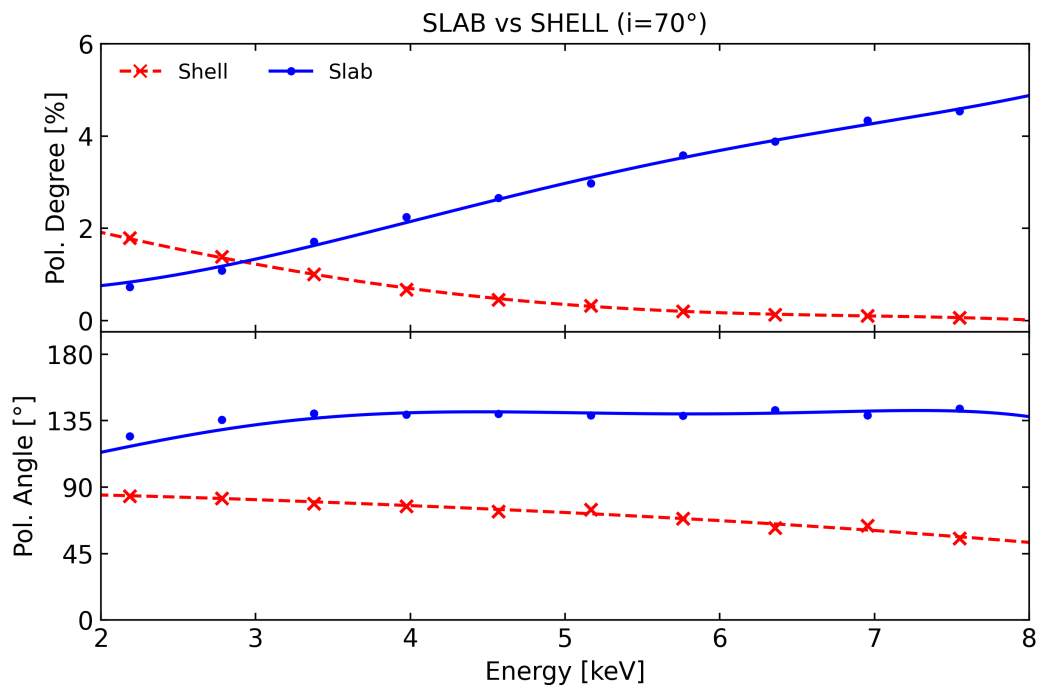


Figure 1.22. Energy dependence of Polarization Degree (top) and Polarization Angle (bottom) for an accreting neutron star low-mass X-ray binary system in the high/soft state. Represented are different polarization properties for the shell coronal geometry (red) and for slab (blue). Image credit: Gnarini et al. (2022).

Chapter 2

Polarimetry of GRS 1915+105 in soft state with returning radiation

The universe is full of magical things, patiently waiting for our wits to grow sharper.

Eden Phillpotts

X-ray observations are crucial in the study of accreting systems around a compact central object. They provide us with information on physical processes in the inner regions of such objects and are used to constrain the spin of the black holes (BHs) in Active Galactic Nuclei (AGN) and X-ray binaries (Reynolds, 2021).

BH X-ray binary systems are very variable and often transient sources, going through different spectral states. Regarding their time variability, luminosity and spectral properties, different accretion states are observed (Remillard and McClintock, 2006). Two basic states are distinguished, namely the low/hard and high/soft states. The low/hard state is characterized by a hard X-ray coronal emission with the accretion disk usually truncated at a large radius. In the high/soft case, the disk radius extends down to the Innermost Stable Circular Orbit (ISCO), and the thermal disk component dominates the spectrum in the classical 2–10 keV band. There are several methods used for determining the BH spin; in the case of BH binaries, modeling the thermal emission is one of the most common (Narayan et al., 2008). Assuming that the inner radius of the disk coincides with the ISCO as it occurs in the soft state (see e.g. Reynolds and Fabian 2008, Shafee et al. 2008, Steiner et al. 2010), spectral measurements can in fact be used to probe the BH spin. In fact, the radius of the ISCO depends on the BH spin, going from 6 gravitational radii ($R_g = GM/c^2$, where c is the speed of light) for a static black hole to 1 R_g for a maximally rotating black hole (see e.g. Novikov and Thorne 1973). This relation is depicted in the Figure 2.2. On the left panel, we see a non-rotating (Schwarzschild black hole), while on the right panel we see a maximally-rotating (Kerr) black hole.

We see that in the case of the spin $a = 0$, the inner accretion disk edge is located farther away from the BH, than in the case of the spin $a = 1$.

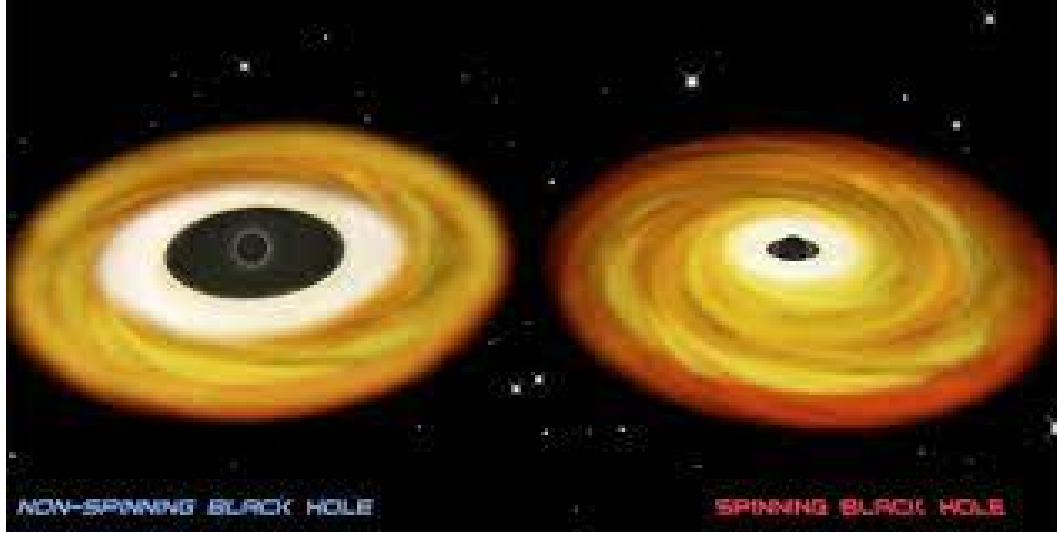


Figure 2.2. A representation of a connection between a black hole spin and the distance of the inner radius of the accretion disk. For non-rotating (or low-spin) black holes, the inner radius is at a greater distance from the black hole (left) than in the case of a maximally rotating black hole (on the right). Image credit <https://www.cfa.harvard.edu/imagelist/2006-30>

The temperature on the surface of the accretion disk depends on the radius according to the following rule of proportion (Shakura and Sunyaev 1973):

$$T_{\text{eff}} \propto R^{-\frac{3}{4}} \quad (2.1)$$

The emitted radiation at each disk radius is assumed to be a blackbody spectrum defined as (Frank et al. 2002)

$$I_{\nu} = \frac{2h}{c^2} \frac{\nu^3}{e^{h\nu/k_B T_{\text{eff}}} - 1} = B_{\nu}(T_{\text{eff}}) \quad (2.2)$$

where h is the Planck constant and k_B is the Boltzmann constant. B_{ν} is the spectral radiance density at frequency ν . This description is, however, only satisfied for a razor-thin accretion disk. In fact, an ionized layer of gas is formed above and below the accretion disk. This feature manifests itself into the observed spectrum and we also detect non-blackbody contributions. For this reason, we have to apply the color correction factor to account for the deviations from the blackbody spectrum (Shimura and Takahara 1995, Merloni et al. 2000, Davis et al. 2005)

$$f_{\text{col}} = \frac{T_{\text{col}}}{T_{\text{eff}}} \quad (2.3)$$

For the color-corrected blackbody spectrum, we then obtain:

$$I_\nu = f_{\text{col}}^{-4} B_\nu(f_{\text{col}} T_{\text{eff}}) \quad (2.4)$$

Determining the ISCO from the thermal spectrum allows one to estimate the BH spin (Zhang et al. 1997, Gierliński et al. 2001). However, in order to get a reliable BH spin constraint, we must know precisely the BH mass, inclination of the accretion disk and the distance of the system from the observer (Zhang et al. 1997).

X-ray polarimetry provides an alternative method to measure the black hole spin of X-ray binaries in soft state. In fact, strong gravity effects modify the polarization properties of radiation emitted by the disk, with, in particular, a rotation of the polarization plane. The effect is larger at small radii, where the emitted radiation is also harder. As a consequence, a variation of the polarization angle with energy is expected (Connors et al., 1980; Dovčiak et al., 2008; Li et al., 2009).

On January 2017, the Imaging X-ray Polarimetry Explorer (IXPE, Weisskopf et al., 2022) was selected in the framework of the NASA Small Explorers program. This mission, a collaboration between NASA and the Italian Space Agency (ASI), was successfully launched on December 9, 2021. Furthermore, the Chinese Academy of Sciences plans to launch the enhanced X-ray Timing and Polarimetry (eXTP) mission (Zhang et al., 2016) in 2027. These instruments will observe X-ray polarization in the 2-8 keV energy band, very well suited for observing thermal radiation in accreting black holes in X-ray binary systems. In fact, measuring black hole spin using the thermal radiation method via X-ray polarimetry is one of the core scientific goals of both missions.

In this thesis, we investigate the polarization properties of an X-ray binary system, GRS 1915+105, in the soft state and the robustness of measuring BH spin, inclination and orientation of the source on the plane of the sky using simulated X-ray polarimetric measurements with IXPE. Even if the source has been in an obscured state after a transition in 2018 (Ratheesh et al., 2021, and references therein), we use its former, well studied soft state as representative of an X-ray binary system (possibly a new transient) in such state. In Section 2.1 we discuss the modeling of multicolor blackbody and introduce the numerical codes we used to reproduce the polarimetric properties of the observed radiation. In particular we simulate both the simple case in which all photons arrive directly to the observer (using the code `KYNBB`) and a more complex one in which photons can return to the disk due to strong gravity effects and then reach the observer after reflection (using the code `KYNBBRR`). In Section 2.2 we analyze the simulated data with the aim to reconstruct spin and geometry of the source. Discussion and Conclusions follow in Section 2.3.

2.1 Polarization features from black hole accretion disk

In this section we first summarize the methodology used to perform our study and then review the codes used (KYNBB and KYNBBRR) in order to have a detailed understanding of the simulations presented later in this chapter.

2.1.1 KYNBB code

For the sake of simplicity, we start considering only the contribution of radiation which arrives directly to the observer without interacting with the disk after emission (i.e. direct radiation). To this aim we used the code KYNBB¹ code (Dovčiak et al., 2008), which is part of the relativistic model package KYN (Dovčiak et al., 2004; Dovciak, 2004). The theoretical framework is based on a few assumptions, namely the Kerr metric to describe the space-time around the central BH and an optically thick, geometrically thin Keplerian accretion disk, characterized by the Novikov-Thorne (Novikov and Thorne, 1973) surface temperature profile. The disk surface is then assumed to be covered by a geometrically-thin, optically-thick atmosphere, in which the main source of opacity is electron scattering (see e.g. Chandrasekhar 1960, Dovciak 2004, Dovčiak et al. 2008).

For the purpose of this work, we used the following model parameters: spin a , inclination i , BH mass M_{BH} , accretion rate \dot{M} , Thomson optical depth of the disk atmosphere τ , orientation of the system on the plane of the sky χ (i.e. orientation of the projected axis of the system, $-90 < \chi < 90$) and normalization factor N defined as $1/D_{10}^2$ (where D_{10} is the distance in units of 10 kpc). The model allows for the possibility to use some additional parameters (e.g. to define an obscuring structure). However, we did not operate with those in our analysis. The full list of the KYNBB model parameters can be found in Table 2.1.

The local polarization properties of the accretion disc emission were computed assuming different optical depths of the scattering atmosphere. In particular, the infinite optical depth approximation by Chandrasekhar (1960) is applied when values of $\tau \gtrsim 10$ are considered² and pre-calculated tables, obtained with the Monte Carlo code STOKES (Goosmann and Gaskell 2007; Marin et al. 2012; Goosmann et al. 2014), are used for smaller τ .

Thomson scattering is used to compute the polarization properties, while the variation as a function of the photon energy is accounted for using the color correction factor f_{col} . Due to symmetry reasons, the emerging polarization is either

¹<https://projects.asu.cas.cz/stronggravity/kyn/tree/master#kynbb>

²It has indeed been found (see Dovčiak et al. 2008) that the result for an infinite slab is already reached for $\tau = 10$.

Table 2.1. Model parameters of KYNBB

Model Parameter	Value	Free/Frozen
Black Hole Spin	(see Table 2.2)	Free (see Section 2.2.1)
Inclination Angle	70	Free (see Section 2.2.1)
r_{in}	1	Frozen
Switch for r_{in}	1	Frozen
r_{out}	1000	Frozen
ϕ	0	Frozen
$d\phi$	360	Frozen
M_{BH}	14	Frozen
\dot{M}	(see Table 2.2)	Frozen
f_{col}	1.7	Frozen
α	-6	Frozen
β	0	Frozen
r_{cloud}	0	Frozen
Redshift	0	Frozen
n <table></table>	80	Frozen
nrad	150	Frozen
Division	1	Frozen
$n\phi$	180	Frozen
Smooth	0	Frozen
Stokes	1	Frozen
χ	0	Free
τ	11	Frozen
nthreads	2	Frozen
Normalization	0.826	Frozen

parallel or perpendicular to the sky projection of the disk symmetry axis. We define the polarization angle to be zero for polarization parallel to the system axis (i.e. $U = 0$ and $Q > 0$ in terms of Stokes parameters), and 90° for the orthogonal case (i.e. $U = 0$ and $Q < 0$). The Stokes parameter V , which denotes circular polarization, is zero in all cases discussed in this study, since Thomson scattering does not generate circular polarization (and the current X-ray polarimeters cannot even measure it).

2.1.2 KYNBBRR code

A complete description of spectral and polarization properties of radiation coming from X-ray binaries in the soft state cannot ignore the contribution of returning radiation, i.e. photons which are bent by strong gravity effects and forced to return to the disk surface, where they can be reflected and eventually reach the observer. We can also use the term self-irradiation of the accretion disk which is an interchangeable term (Connors and Stark 1977; Stark and Connors 1977). We show a brief general representation of the observation of the source with marked angles of

inclination Θ , orientation of the system on the sky of the observer χ and the source distance towards the IXPE telescope (alternatively, the observer) d in the Figure 2.4. Modeling returning radiation features first requires to calculate the photon trajectories in the vicinity of the central BH, where general relativistic effects are more important. To this aim we used the ray-tracing based, SIM5 code SELFIRR (Bursa 2017; Zhang et al. 2019). This code calculates all the null geodesics which end up on a given point on the disk surface from different incidence directions, starting from a different disk location. The disk surface is, then, divided into a number \bar{N}_r of incident points, each characterized by the distance \bar{r}_i from the central BH, while the possible incidence directions are sampled through a discrete $\bar{N}_\Theta \times \bar{N}_\Phi$ angular mesh, according to the polar angles $\bar{\Theta}_i$ and $\bar{\Phi}_i$ they form with the disk normal. For each geodesic, SELFIRR returns the central distance \bar{r}_e and the emission direction angles $\bar{\Theta}_e, \bar{\Phi}_e$, tracing back in this way all the possible returning photon trajectories. Alongside the numbers $\bar{N}_i, \bar{N}_\Theta$ and \bar{N}_Φ , which provide the grid dimensions, input parameters for each run are the BH mass M and spin a . The output of the code is a fits file, containing all the geodesic parameters, which can be used inside the KYN package.

First simulations including returning radiation contributions assumed that returning photons were all reflected to the observer, i.e. with a 100% disk albedo (Schnittman and Krolik, 2009). However, as shown in subsequent works (Taverna et al., 2020), in realistic conditions absorption may not be negligible and the albedo will be reduced correspondingly. As noted by Schnittman and Krolik (2009), considering 100% albedo would mean having a switch between PA values. At lower energies, direct radiation is more important, but at higher energies returning radiation becomes prevalent and has higher polarization degree. On the other hand, a constant albedo of 50% would shift the switching energy to higher values. Following the work by Taverna et al. (2020), where a self-consistent simulation for the albedo profile as a function of the energy was obtained using the software CLOUDY (Ferland et al., 2017), we fixed the albedo at the value of 50%, which closely resembles that simulation (see their Figure 12).

While we observe a substantial change in PA across the 1–10 keV band for all the inclinations for the highest spin values (bottom right panels of Figures 2.5 and 2.6), this is only true for lower inclinations in the case of $a = 0$. Similarly, we observe a change in the behavior of PD, which tends to decrease at low energies, but then, starting at ≈ 2 keV starts getting constant or slightly increasing. For the lowest inclination (10°) we see a very pronounced minimum in PD, which is shifted towards lower energies for higher spins.

2.1.3 Energy dependence of polarization features

The numerical code we used integrates the emission over the entire accretion disk, allowing us to shift from local to global polarization properties. At large distances from the black hole, the polarization degree is high (as represented by the length of

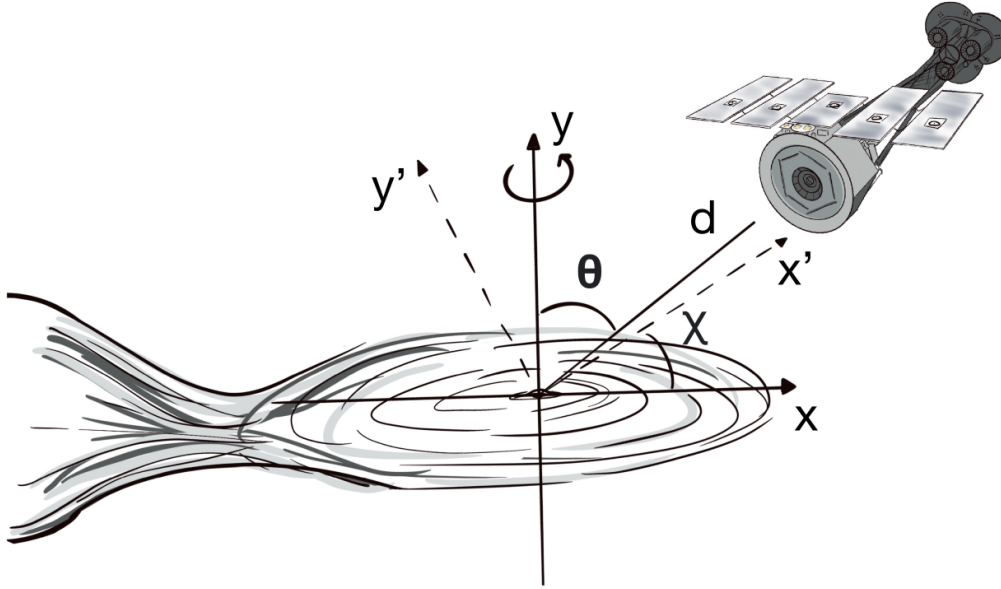


Figure 2.4. A visual representation of an x-ray binary system as observed by IXPE with marked angles for inclination Θ , orientation of the system χ and its distance d towards the observer. Figure credit: Anastasia Yilmaz.

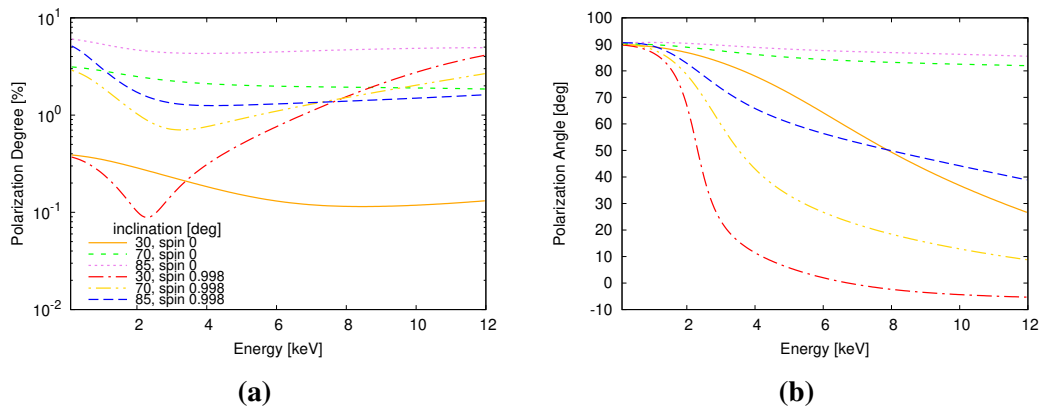


Figure 2.5. Polarization degree (left) and polarization angle (right) dependence on energy for different inclination cases for GRS1915+105 with BH mass $M = 14 M_{\odot}$ and spin $a = 0$ (orange, green and violet lines) and $a = 0.998$ (red, yellow and blue lines). The accretion rate is considered in such a way, that it would correspond to the observed luminosity $L = 0.45 L_{\text{Edd}}$. The plots were created using the KYNBBRR model.

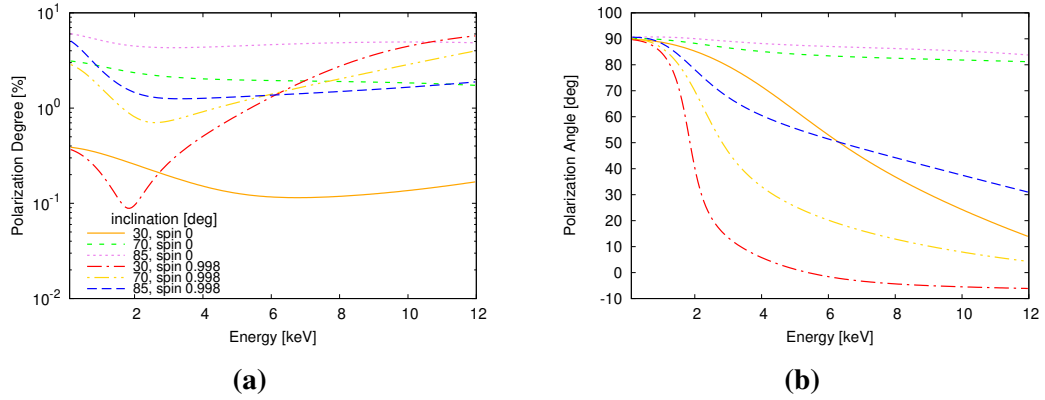


Figure 2.6. Same as in Figure 2.5, but with the accretion rate corresponding to the luminosity $L = 0.185 L_{\text{Edd}}$. The plots were created using the KYNBBRR model.

the blue line on the bottom right subpanel of Figure 2.7), the polarization vector is parallel to the disk, and the emission is soft. Nearing close to the black hole, the emission is much harder and we observe a change in the direction of the polarization vector by about 30° (blue line on the bottom right subpanel). The polarization degree, represented by the length of the line, is smaller due to the superposition of different polarization vectors. These relativistic effects play an important role, as it can be observed in Figure 2.7.

Figures 2.8 and 2.9 (and similarly also Fig. 2.5 and Fig. 2.6, but with the effects of returning radiation taken into account) show the dependence of the polarization degree (PD) and angle (PA) on energy for various inclination angles, two different values of the BH spin ($a = 0$ and 0.998) and for different accretion rate values. These accretion rate values are set in such a way that the corresponding luminosity is $L = 0.446 L_{\text{Edd}}$ (Fig. 2.8) and $L = 0.204 L_{\text{Edd}}$ (Fig. 2.9) for the model without the returning radiation (KYNBB) and luminosities $L = 0.45 L_{\text{Edd}}$ (Fig. 2.5) and $L = 0.185 L_{\text{Edd}}$ (Fig. 2.6) for the model with the effects of returning radiation into account (KYNBBRR); L_{Edd} denotes the Eddington luminosity.

In the 2–8 keV energy band the PD stays almost constant for both the spin and luminosity values sampled when returning radiation is not included, and for spin $a = 0$ with returning radiation. However, this is not the case for spin 0.998 when the impact of the returning radiation is taken into account (panels (c) in Figures 2.5 and 2.6). In these two cases, we see a rise of PD by $\approx 1.5\%$, accompanied by the steepest change in PA.

Generally, we observe very pronounced changes of PA in the cases of the highest spin value ($a = 0.998$) and for the modeled systems with lower inclination. This rapid change corresponds to the lowest PD, which is in agreement with the theoretical

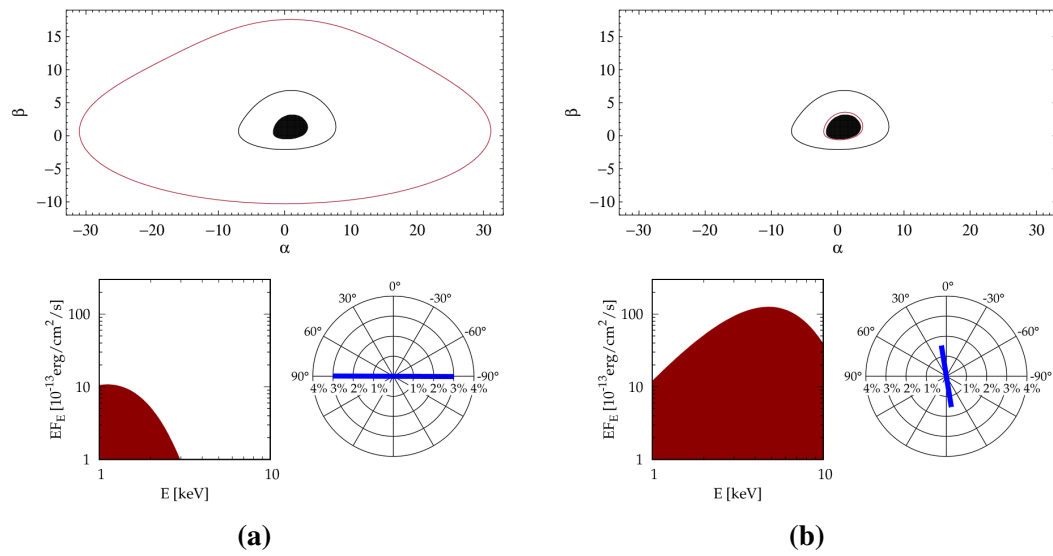


Figure 2.7. Upper panel: representation of a black hole accretion disk on the sky of the observer. Bottom: flux and the polarization direction of collected radiation. The effects of variation of the polarization angle due to strong gravity are shown going from left to right. The figures represent a maximally rotating black hole. Starting from a region distant from the black hole, at $r = 30r_g$, (a), emission peaks at lower temperatures (≈ 1 keV) and the polarization is horizontal. Then, going very close to the black hole, at $r = 1.285r_g$, (b), the energy flux peaks at a higher energy (≈ 5 keV) and the polarization (blue line on the bottom right subpanel) is close to vertical. The length of the blue line represents the polarization degree, which gets lower closer to the source.

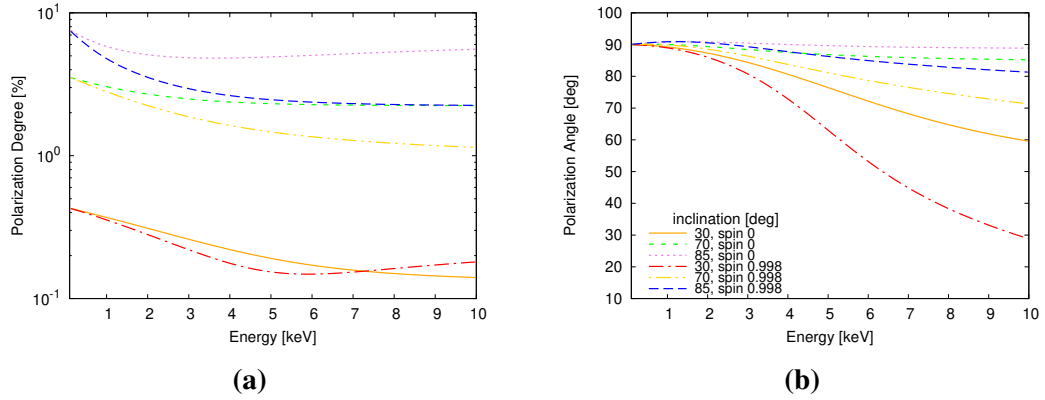


Figure 2.8. Same as in Figure 2.5, but with the accretion rate corresponding to the luminosity $L = 0.446 L_{\text{Edd}}$. The plots were created using the KYNBB model.

prediction (as described in the Figure 2.7).

The polarization angle has a clear decreasing trend for $a = 0.998$, even for high inclination cases. On the other hand, it is nearly constant for higher inclination values over the 2–8 keV band for spin $a = 0$ and both the accretion rate values in both models, while for low-inclination systems, it is distinctly decreasing. In the case of a non-rotating BH, the most pronounced change in PA is for $i = 10^\circ$ and $i = 30^\circ$ (all considered accretion rate values). The most prominent change is from 90° down to $\sim 15^\circ$ or $\sim 0^\circ$ (Fig. 2.6) and to $\sim 55^\circ$ and $\sim 20^\circ$ in the Fig. 2.9 for the source with and without returning radiation, respectively. Moreover, a slightly higher polarization is observed for a lower BH spin. This is caused by the rotation of the polarization angle in the strong gravitational field.

To summarize, for a non-spinning BH, where the inner disk radius is large, the polarization angle does not rotate much. For a spinning BH, where the inner disk radius is small, the polarization angle of the photons coming from the inner parts of the disk is much rotated, causing depolarization. Therefore, the net polarization is lower in the case of a higher BH spin.

2.2 Results

To see whether we can reliably reconstruct model parameters from polarization signatures, we inspected the simulated polarization properties. We started exploring the effects of varying the BH spin and the inclination and orientation of the disk for direct radiation, using the KYNBB code.

Then, we considered in addition returning radiation effects with simulations based on KYNBBRR. In the latter case, to better highlight the effects of returning radiation, we assumed the inclination and orientation of the source to be known parameters.

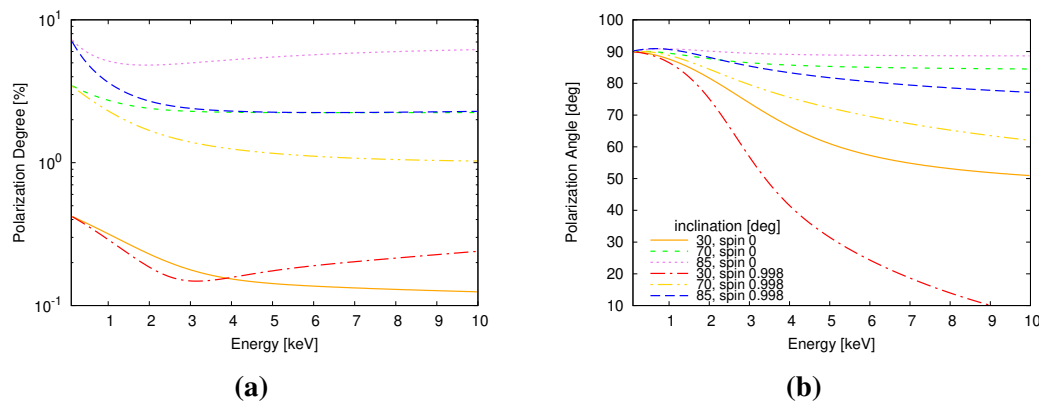


Figure 2.9. Same as in Figure 2.5, but with the accretion rate corresponding to the luminosity $L = 0.204 L_{\text{Edd}}$. The plots were created using the KYNBB model.

We chose to work with the Stokes parameters instead of PD and PA. Stokes parameters are independent quantities, while PD and PA are not, being derived from the Stokes parameters I , Q and U by the following relations (for linear polarization):

$$\text{PD} = \frac{\sqrt{Q^2 + U^2}}{I} \quad (2.5a)$$

$$\text{PA} = \frac{1}{2} \arctan\left(\frac{U}{Q}\right) \quad (2.5b)$$

which are non-linear and, therefore, PD and PA will bear non-gaussian errors.

2.2.1 KYNBB

We studied the capability in constraining the spin of the black hole and the inclination of the accretion disk from the simulated observations by fitting the Stokes spectra leaving free these two parameters, as well as the orientation of the system.

The input and the best fit values for all of studied cases are reported in Table 2.2. We produced contour plots of spin versus inclination for all of the reported cases. We show contours for 1σ (red), 2σ (green) and 3σ (blue) confidence levels in the Figure 2.10 panel (a), obtained for a 500 ks simulation.

The input parameters were correctly reconstructed, as the gray cross (marking the original value) and black "plus" signs (best-fit) almost overlap for all four of the studied spin cases. The interval of good-fit values (considered here and later for 1σ) for inclination is spread out through $\Delta i \approx 20^\circ$ ($20^\circ/70^\circ \sim 29\%$) for the cases of spin $a = 0.7, 0.9$ and 0.998 , while the spin is constrained within $\Delta a \lesssim 0.12$ ($\sim 12\%$). The case of $a = 0$ seems to be the most problematic to reconstruct, as we obtained

Table 2.2. Best-fit values for the spin (a), inclination (i) and orientation of the source on the sky of the observer (χ) for simulated exposure times 500 ks, 250 ks and 125 ks, modeled and fitted with KYNBB. (u) - errors that were unconstrained during the fitting procedure.

	Model	500 ks	250ks	125 ks
$\dot{M}[M_{\odot}/yr] = 2.43 \times 10^{-7}$				
a	0	$0.017^{+0.383}_{-0.017}$	$0.0^{+0.11}_{-u}$	$0.0^{+0.16}_{-u}$
$i[^{\circ}]$	70	71^{+6}_{-21}	76^{+4}_{-28}	77^{+5}_{-34}
$\chi[^{\circ}]$	0	0^{+3}_{-2}	0^{+1}_{-3}	-3 ± 3
$\chi^2/d.o.f.$	–	946.51/897	919.7/897	873/897
$\dot{M}[M_{\odot}/yr] = 8.92 \times 10^{-8}$				
a	0.7	$0.7^{+0.09}_{-0.05}$	$0.82^{+0.11}_{-0.16}$	$0.7^{+0.08}_{-0.06}$
$i[^{\circ}]$	70	68^{+7}_{-8}	59^{+20}_{-8}	77^{+5}_{-21}
$\chi[^{\circ}]$	0	0^{+3}_{-2}	6^{+4}_{-6}	-5^{+7}_{-4}
$\chi^2/d.o.f.$	–	841.21/897	905.04/897	873.03/897
$\dot{M}[M_{\odot}/yr] = 4.70 \times 10^{-8}$				
a	0.9	$0.91^{+0.068}_{-0.064}$	$0.988^{+u}_{-0.09}$	$0.858^{+0.06}_{-0.05}$
$i[^{\circ}]$	70	66^{+12}_{-8}	58^{+11}_{-4}	79^{+7}_{-25}
$\chi[^{\circ}]$	0	4^{+5}_{-3}	9^{+4}_{-7}	-1^{+14}_{-5}
$\chi^2/d.o.f.$	–	900.7/897	847.9/897	980.8/897
$\dot{M}[M_{\odot}/yr] = 1.98 \times 10^{-8}$				
a	0.998	$0.998^{+u}_{-0.021}$	$1.0^{+u}_{-0.020}$	$0.988^{+u}_{-0.020}$
$i[^{\circ}]$	70	69^{+8}_{-3}	71 ± 10	79^{+8}_{-12}
$\chi[^{\circ}]$	0	1^{+4}_{-6}	1^{+4}_{-7}	-8^{+9}_{-6}
$\chi^2/d.o.f.$	–	915.2/897	860.29/897	865.5/897

$\Delta i \sim 30^\circ$ ($\sim 43\%$) and $\Delta a \sim 0.4$ ($\sim 40\%$). We show the strength of the spin and inclination constraints in Figure 2.11 (panels (a) and (b), respectively) as a function of the modeled values for these two parameters. The function is represented by the green dashed line. The reconstructed values lay on the green line for all the studied spin cases within their corresponding errors, which manifests the strength of the used method. We simulated the same case for different exposure times of 250 ks and 125 ks, shown in panels (b) and (c) of the Figure 2.10. It is clear from the plots that, as expected, the lower the simulated exposure time, the higher the uncertainty in the spin and inclination reconstruction.

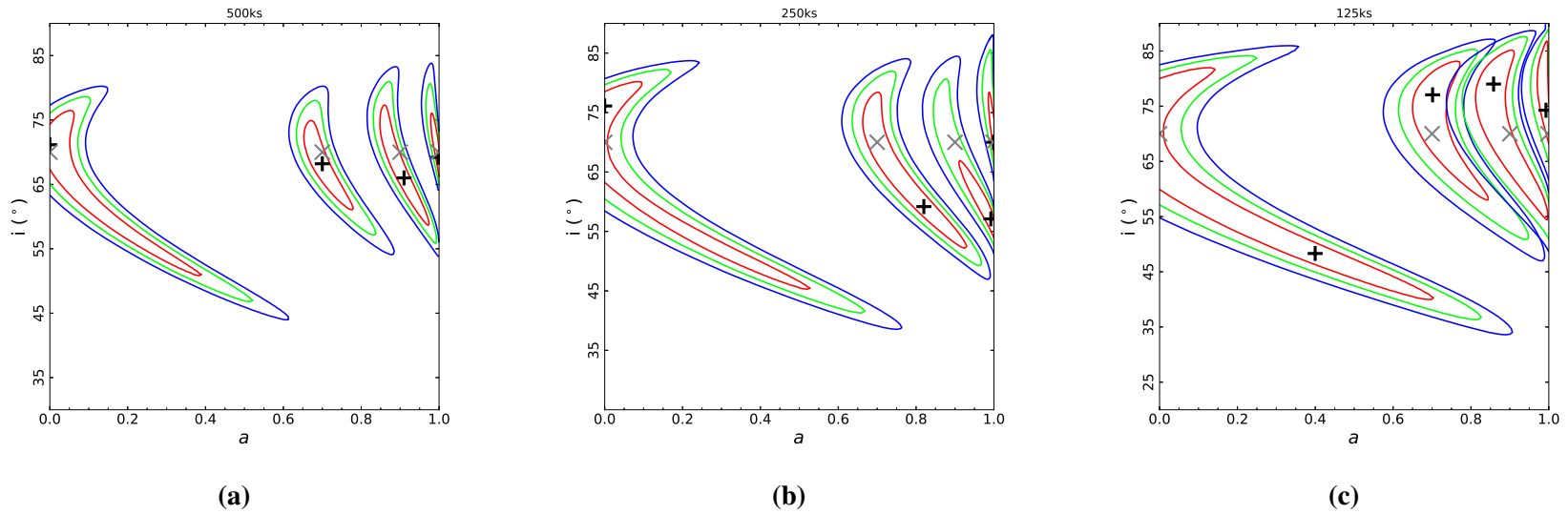


Figure 2.10. Contour plots of spin vs inclination resulting from the fit the simulated Stokes parameters Q and U obtained for $a = 0, 0.7, 0.9, 0.998$ for various exposure times: (a) $t = 500$ ks, (b) $t = 250$ ks and (c) $t = 125$ ks. Confidence contours at 1σ (red), 2σ (green) and 3σ (blue) are also shown. The gray cross marks the original values, which were (left to right, for each panel) spin $a = 0, 0.7, 0.9$ and 0.998 and $i = 70^\circ$ for all the plotted cases. The black "plus" sign shows the best fit value, which is (again, left to right) $a = 0, 0.7, 0.91$ and 0.998 (a), $a = 0, 0.82, 0.992$ and 0.999 (b) and $a = 0.4, 0.7, 0.86$ and 0.993 (c). Data are plotted for a model without returning radiation (KYNBB).

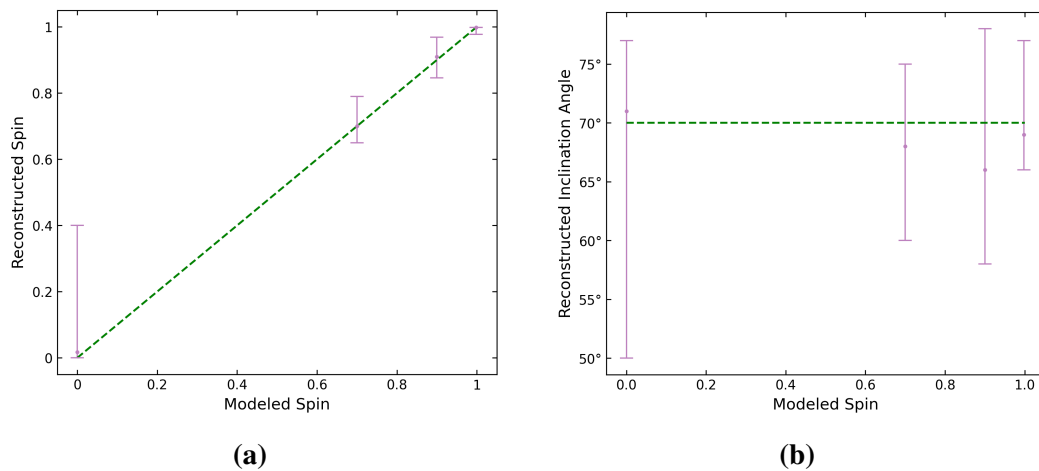


Figure 2.11. Spin (a) and inclination (b) constraints with the `KYNBB` model versus input values. Green dashed line represents the 1:1 relation for reconstructed and input spins (a) and the input value for the inclination (b).

2.2.2 `KYNBBRR`

In this part, we inspect the effects of returning radiation on the observed polarization properties of source radiation. We first had to use the `SELFIRR` code calculating the null geodesics through the accretion disk. We used a grid of dimensions $\bar{N}_i = 500$, $\bar{N}_\Theta = 100$ and $\bar{N}_\Phi = 100$, as described in Section 2.1.2. Then, we used the code `KYNBBRR` in order to model the returning radiation effects of the source. To study this process, we treat the inclination and the orientation of the source as known parameters which, as discussed above, is a solid assumption for GRS 1915+105. We simulated observations of GRS1915+105 for IXPE, as in the previous section and used the data of the Stokes parameters Q and U in 2–8 keV interval.

We considered the presence of a less than 100% albedo of the disk surface. In our simulations, we considered an energy-independent 50% albedo. The Stokes parameters spectra, simulated for $a = 0.998$ and for each of the three IXPE detector units and fit with theoretical model are shown in Figure 2.12. To address the capabilities in reproducing the observations, the contour plots of spin versus albedo were created. Since the code that we use for this study does not interpolate within spin values yet, the fitting procedure is as follows: we freeze all the parameters to their original (modeled) value, with the exception of albedo of the source. We perform a fit and thaw the spin parameter afterwards. We produce a contour plot of spin versus albedo. When a better fit for albedo is found, we change its value to the current best fit, freeze spin and perform fit followed by a contour spin-albedo calculation. We iterate this procedure until we find the fit with the lowest chi square statistics. Due to the interpolation issue, we used three different grids in spin for the calculation of the contour plots. They are as follows: 0–1 interval with step 0.005 (subplots (a) and (b) of Figure 2.13), 0.7–1 with step of 0.01 (subplot (c) and the

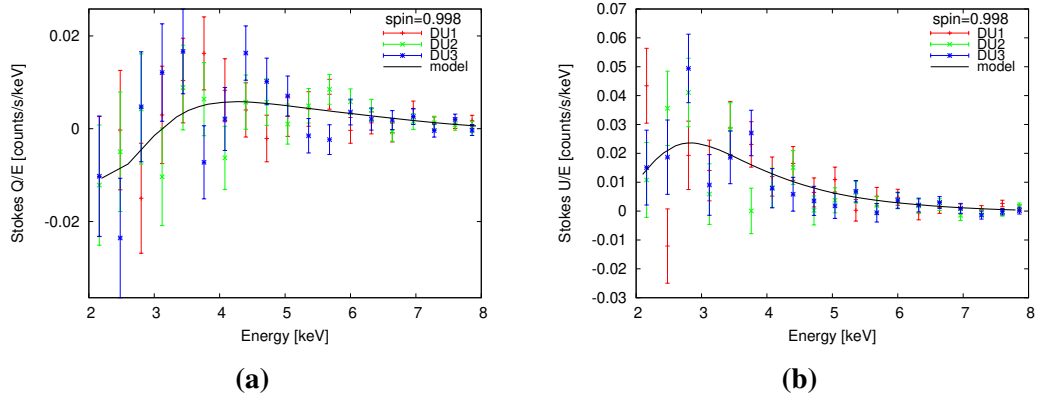


Figure 2.12. Energy dependence of Stokes Q/E (a) and U/E (b) data simulated for spin 0.998 and for each of the three IXPE detector units fitted with the theoretical model. Response matrix was applied on the models. The data were simulated using a model with returning radiation (KYNBBRR).

part 0.9–98 of subplot (d)), and 0.98–1 with the step of 0.002 (0.98–1 interval in the black rectangular area of the subplot (d)). We were able to successfully reconstruct the spin in all four of the studied cases (Figure 2.13) - the gray cross (original value) and black "plus" signs (best-fit) overlap in spin (for $a = 0$ and 0.998), or lay only a slight distance from one another (cases $a = 0.7$ and 0.9). Similarly, albedo reconstruction was quite successful, although with rather large errors. Within 1σ , the interval of satisfactorily fitting albedo values is approx. Δ albedo = 0.45 for $a = 0$ and 0.9 and approx. Δ albedo = 0.3 for the cases $a = 0.7$ and $a = 0.998$.

2.3 Discussion and conclusions

We studied the robustness of constraining BH spin from the simulated Stokes parameters spectra. For a simulated exposure time of 500 ks, we were able to successfully recover spin and inclination of the studied system for spin cases of $a = 0.7, 0.9$ and 0.998, for both the models with and without returning radiation. On the other hand, there is a strong degeneracy between the system inclination and the BH spin particularly for $a = 0$ in the model without the returning radiation. It will be therefore crucial to obtain inclination of the studied source independently, e.g. from spectroscopic observations.

Constraints on spin and inclination presented in this work were performed assuming distance, mass and accretion rate as known parameters. It is difficult to determine spin and inclination with either distance, mass or mass accretion rate as variable quantities, and this is the reason why we obtain a wider interval of possible values for the examined parameters and some spin cases might become indistinguishable.

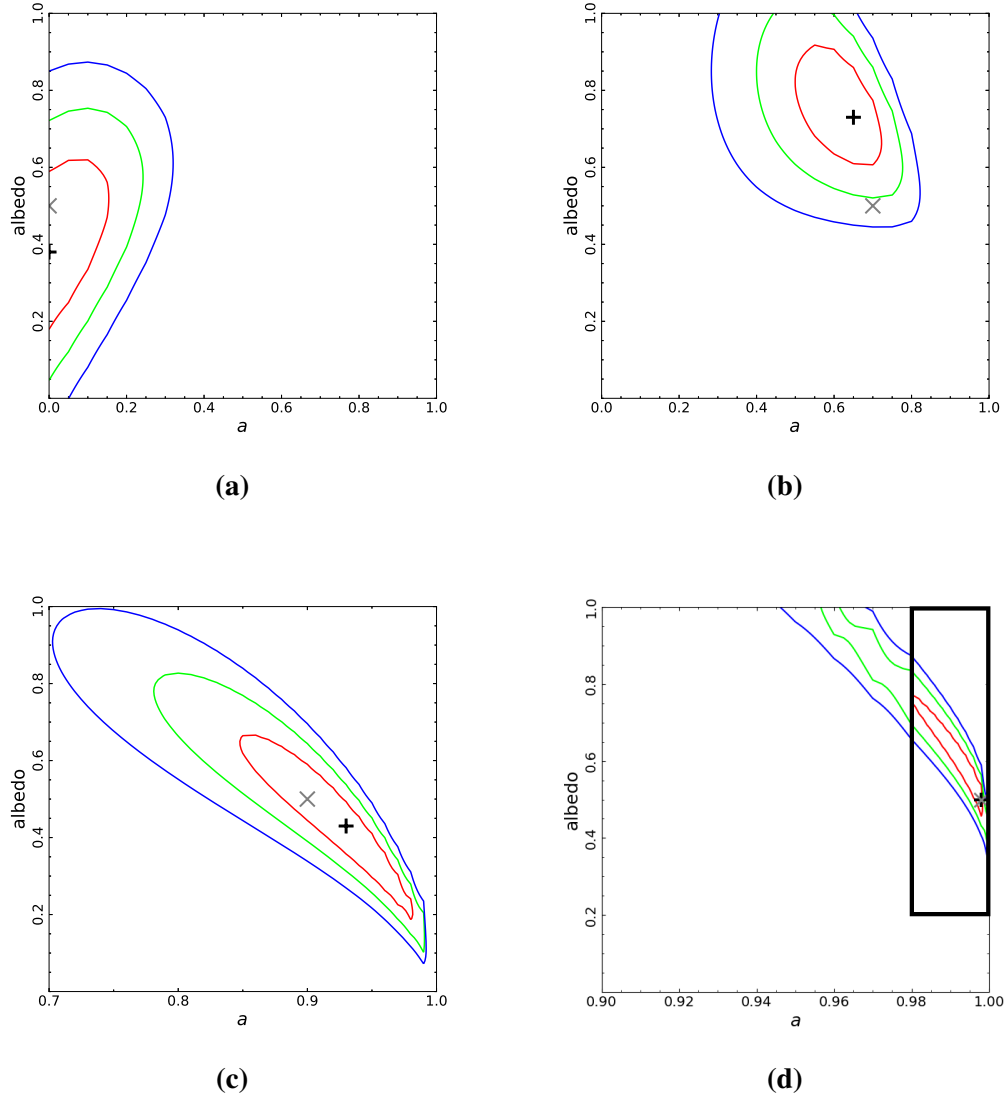


Figure 2.13. Contour plots of spin vs albedo for spin values $a = 0$ (a), 0.7 (b), 0.9 (c) and 0.998 (d) using simulated Stokes Q/E and U/E dependence on energy data. Plot in (d) is composed of two different grids divided by the black rectangular area, with the interval in spin 0.90 – 0.98 having a step of 0.01 and the interval 0.98 – 1.00 with the step of 0.002 . In red 1σ , green 2σ and blue 3σ contours. Similarly to the previous case, the grey cross sign marks the original value, which was 50% albedo in all the shown cases and spin $a = 0$ (a), $a = 0.7$ (b), $a = 0.9$ (c) and $a = 0.998$ (d). The black "plus" sign marks the best-fit value, which is as follows: $a = 0$, albedo = 38% (a), $a = 0.65$, albedo = 73% (b), $a = 0.93$, albedo = 43% (c), $a = 0.998$, albedo = 50% (d). Plots are calculated using a model with returning radiation (KYNBRR).

In our initial studies we did not obtain a satisfactory fit for a spin - accretion rate case, suggesting \dot{M} may not be sensitive on the polarization properties. However, we expect that the value of \dot{M} will be constrained by the complementary information on the flux spectral shape that will be automatically provided by spectral analysis, which can be performed as well using the data collected by polarimetric observatories (like IXPE) or by coordinated observations with other facilities. This information, together with the polarimetric observations, will allow one to infer more precisely the fundamental X-ray Binary properties. X-ray polarimetry represents a highly desirable tool that will be beneficial when studying strong gravity effects of compact objects because it provides independent constraints on some of the parameters.

It is apparent from our results that considering the returning radiation effects adds more degeneracy to the problem, for example with the addition of the albedo parameter. In this case, to make things simpler, we treated the inclination as a known parameter. We obtained an acceptable fit for both $a = 0$ and 0.9 , although with large errors, as the corresponding contours cover almost half of the $0-1$ interval for the albedo. This implies that the detection of the albedo is strongly influenced by the spin of the black hole; this indicates that ignoring the albedo value will manifest itself in unconstrained spin. For $a = 0.7$ and 0.998 we do not observe this degeneracy.

It is important to note that in this study we considered a constant albedo value across the energy spectrum. This can be fulfilled under the condition that the material in the accretion disk is fully ionized. In the recent work by Taverna et al. (2021), this issue is generalized through studying the top layer of the accretion disk and computing its ionization profile, for which the polarization properties are obtained. Considering varying albedo profile thus allows for studying absorption, alongside scattering, as a process responsible for polarization. They find higher absorption linked to higher polarization degree. We plan to include all the above calculations in future version of the code.

Finally, it is worth to remark that eXTP will have on board a polarimeter with characteristics very similar to that of IXPE, but with an effective area 4-5 times larger. Our results can then be considered valid also for eXTP, once the exposure time has been rescaled accordingly.

Chapter 3

Neutron Stars - LMXB

Ever tried.
Ever failed.
No matter.
Try again.
Fail again.
Fail better.

Samuel Beckett

3.1 Introduction

In weakly magnetized Neutron Stars in Low-mass X-ray binaries (NS-LMXBs), in addition to that from the accretion disk, another thermal emission originates from the neutron star surface. In the western-like model (White et al. 1988) the hot photons emitted by the NS are observed directly and described using a black-body profile, while a corona obscures the accretion disk and is responsible for Compton scattering of the photons coming from the disk. On the other hand, the eastern-like model (Mitsuda et al. 1984, Mitsuda et al. 1989) considers a reversed scenario with the NS population being almost fully Comptonized due to the presence of corona, and the accretion disk is observed directly as a blackbody. The two models are degenerate spectroscopically, but polarimetry can help distinguish the actual shape and physical properties of the corona, because X-ray polarization is extremely sensitive to the coronal geometry (Gnarini et al., 2022). The goal of this study is to constrain the physical parameters of the corona, as well as the contribution from reflection. Both are of prime importance when it comes to interpreting the results of polarimetric studies. The physical parameters of the corona and the reflecting medium are of crucial importance in order to perform realistic numerical simulations (Gnarini et al., 2022). Moreover, the contribution from reflection is needed to help us understand the actual origin of polarization in the studied sources. Can it be the corona alone, or reflection itself, or a mixture of the two? A spectroscopic study is essential to help

us answer these questions. We look into observations of three weakly magnetized NS-LMXB sources, that were observed by IXPE in its first year of observations: GS 1826-238 observed by the NuSTAR telescope in June 2014, GX 9+9 observed in April 2019 and a January 2015 observation of Cyg X-2, with the aim of using the results of these analyses as an input for theoretical simulations that are later applied on the IXPE data of these three sources.

3.2 Studied sources

We studied the spectral properties of three accreting NS-LMXB sources: GS 1826-238, GX 9+9 and Cyg X-2. In this part we briefly summarize their properties based on their previous observations. We chose to work with observations of these sources performed using the NuSTAR observatory, since, owing to its broad bandpass, it is the best instrument to probe both corona and reflection. It is worthwhile to notice, that this is the first time the GX 9+9 observation from April 2019 is studied, as a data analysis from this observation has never been published before.

GS 1826-238

In this section, we look at spectral properties of an accreting NS-LMXB source GS 1826-238. The source is known for its precise regularity of X-ray bursts present throughout the span of multiple years (Cocchi et al., 2000; Zamfir et al., 2012). The bursts would last $\gtrsim 100$ s with a periodicity of 3.56 - 5.74 hr (Galloway et al., 2004). This behavior has earned the source the moniker "clocked burster". The occurrence of these highly regular bursts was present while the source was in the low-hard state accompanied by a strong power law. The bursts were present also during the short transitions of the source to the high-soft state, however, were way shorter and considerably less regular (Chenevez et al., 2016). GS 1826-238 was in the hard spectral state and classified as an atoll source until 2016, when the source underwent a transition into high-soft state and has remained as such since. The source is presumed to have an inclination below 70° according to Homer et al. (1998). Some later studies suggest the inclination to be even lower: a value of $69_{-3}^{+2^\circ}$ was obtained by Johnston et al. (2020) and an inclination of $(62.5 \pm 5.5)^\circ$ measured in a study by Mescheryakov et al. (2011). In a recent study of GS 1826-238 observed by AstroSat, Agrawal et al. (2022) conclude that can be well described by a combination of a thermal component (multi color accretion disk or a blackbody radiation) and a Comptonized element. The corona of the source changed its optical depth τ from ≈ 5 to ≈ 21 .

GX 9+9

GX 9+9 is a bright atoll source (Hasinger and van der Klis, 1989). The binary source is composed of a neutron star accreting mass from a star with $M = 0.2 -$

0.45 M_{\odot} measured by (Hertz and Wood, 1988). They also discovered the orbital period of GX 9+9 to be 4.19 ± 0.02 hr analyzing an observation by HEAO-1. They assumed the neutron star in this system to have a mass $M = 1.4 M_{\odot}$, and constrained the inclination of the source to be lower than 63° . Vilhu et al. (2007) estimate the distance of 5 - 7 kpc. On the other hand, Savolainen et al. (2009) argued that the distance of the source is 10 kpc. Iaria et al. (2020) studied the source using the BeppoSax and XMM-Newton observations. In their work, a model composed of thermal emission component originating in the inner region of the accretion disk and a component accounting for Comptonization provides a good fit. They also calculated the inclination of the source being $43_{-4}^{+6\circ}$ for the Eastern Model and $51_{-2}^{+9\circ}$ for the Western Model. They also estimated that the corona should have a compact structure and should be located in the vicinity of the innermost region of the central neutron star.

Cyg X-2

The last NS-LMXB we studied is Cyg X-2. The source has been drawing attention especially due to its high X-ray flux $F_X \sim (1 - 3) \times 10^{-8}$ erg cm $^{-2}$ s $^{-1}$. The binary contains a star with a mass $M = 0.4 - 0.7 M_{\odot}$ (Cowley et al., 1979) and a neutron star with a mass $M = 1.71 \pm 0.21 M_{\odot}$ (assuming an inclination of the binary $i = 62.5 \pm 4^{\circ}$), as measured by Casares et al. (2010). Cyg X-2 is classified as a Z-source, as in the color-color diagram (CCD) it follows a shape of the letter Z (Hasinger and van der Klis, 1989). Wijnands et al. (1997) report having observed the source variations on the Z-track. There has been some substantial variability in the X-ray light curve observed during its 2015 NuSTAR observation (Mondal et al., 2017). Di Salvo et al. (2002) report the presence of a soft multicolor disk component together with a thermal Comptonization of a low-temperature plasma and the optical depth $\tau \sim 5 - 10$. This model points towards the preference of the Eastern Model with the accretion disk being observed directly and therefore described by the soft model component and the Comptonization arising in the vicinity of the NS, either in the boundary or spreading layer (BL/SL). The boundary layer is the gas decelerating part of the accretion disk surrounding the NS (Popham and Sunyaev, 2001), while the spreading layer represents a layer of gas on the surface of the neutron star. It is possible for this layer to extend to high latitudes on the NS surface (Inogamov and Sunyaev 1999; Suleimanov and Poutanen 2006). In a recent paper by Ludlam et al. (2022) a NICER and NuSTAR spectral analysis is reported. They describe the source via reflection model for reprocessed emission in the accretion disk. They were able to derive the location of the inner radius of the accretion disk to be rather close to ISCO and remain quite stable during the source state transitions.

3.2.1 Methodology

We used mainly two models to perform the analysis of the studied sources. Those are the following:

- EM: calibration constant, Galactic absorption, accretion, blackbody component and thermally comptonized continuum
constant*TBabs*(diskbb+nthComp)
- WM: calibration constant, Galactic absorption, accretion, blackbody component and thermally comptonized continuum
constant*TBabs(bbodyrad+nthComp)

In all the models used in this section, the column density nH of the TBabs model component had the value of $0.2 \times 10^{22} \text{ atoms/cm}^2$. When considering the Eastern Model scenario, we are observing the accretion disk directly, therefore we use the diskbb model to fit this part of the spectrum. The NS is covered by a shell-structured corona and the photons emitted by the star are Comptonized by the corona. In such a case, the corona is fit by the nthComp model. A reverse scenario happens when considering the Western model. Here, we observe the NS directly as a blackbody spectrum, hence the usage of the bbodyrad model component. The corona surrounds the accretion disk and scatters its photons, in this case nthComp fits disk and the corona.

For all the three sources, we use observations that are available in the NuSTAR public archive as of 02/2022. For the first source, GS 1826-238, we analyzed observations (see Table 3.1) with IDs 80001005002 (further referred to as obsid02) and 80001005003 (obsid03), that took place in June 2014 and had exposure time of 13.2 ks (obsid02) and 38.7 ks (obsid03). We analyzed the spectra as follows: we applied the model on obsid02 and obsid03 separately, fit the data and checked for the variable parameters between the two obsids (variable parameters are not consistent within the errors between the two obsids). Then, we applied the model on the whole data set, while the following was applied:

- obsid02_A with free parameters T_{in} and normalization (diskbb) in the case of EM and kT and normalization (bbodyrad) in the case of WM; power law photon index Γ , temperatures kT_e and kT_{bb} and normalization (nthComp)
- obsid02_B with only the cross-calibration constant free
- obsid03_A having the variable parameters that were identified before are free and untied
- obsid03_B where all parameters are tied to obsid03_A, except for the cross-calibration constant, which is linked to obsid02_B

For this source and both models (EM and WM), the only parameter that was not variable between obsid02 and obsid03 was the electron temperature kT_e .

Table 3.1. Log of the observations of the studied sources

Source	Date	Observation ID	Exposure (ks)
GS 1826-238	June 27, 2014	80001005002	13.2
		80001005003	38.7
GX 9+9	April 30, 2019	30401015002	30.232
Cyg X-2	January 7, 2015	30001141002	23.737

As for GX 9+9, the observation we study took place in April 2019 with exposure time of 30.232 ks and has the ID 30401015002. We applied the EM and WM, respectively, using a similar strategy, as for the previous source: obsA had as free parameters the temperatures of the accretion disk, the corona and the NS and normalizations of `diskbb/bbodyrad` and `nthComp`. All the parameters of obsB were tied to those of obsA, with the exception of the cross-calibration constant, which was left free to vary.

We analyzed the observation of Cyg X-2 with the ID 30001141002, which took place in January 2015 and had an exposure time of 20.737 ks. We selected this particular observation for Cyg X-2 due to the fact that the source was in the spectral state closer to the one that was observed with the IXPE satellite Farinelli et al. 2023. Again, we used both Eastern and Western models, respectively. We applied a similar method in order to analyze the source spectrum, as in the case of the first source.

The Eastern and the Western Models that we use consist of the following parameters:

- EM: calibration constant, Galactic absorption, accretion, blackbody component and thermally comptonized continuum
`constant*TBabs*(diskbb+relxill(Cp)+nthComp)`
- WM: calibration constant, Galactic absorption, accretion, blackbody component and thermally comptonized continuum
`constant*TBabs(bbodyrad+relxill(Cp)+nthComp)`

The reason for adding the `relxill` or `relxillCp`¹ component is explained later, in the 3.3 section.

¹<http://www.sternwarte.uni-erlangen.de/~dauser/research/relxill/>

3.3 Results

3.3.1 GS 1826-238

We report the best-fit parameters for both the EM and WM in the Table 3.2 and in the Fig. 3.1. The residuals of both fits are similar; however, there are differences in the two fits, mainly regarding the fit statistic and the values of the studied parameters.

The EM fit has a statistic $\text{chisq/d.o.f.} = 593/470$. The temperature of the corona is $kT_e = 9.65$ keV (same for both observations), the disk temperature $T_{in} = 0.663$ keV and $T_{in} = 0.738$ keV (obsid02 and obsid03, respectively), the temperature of the NS is $kT_{bb} = 1.14$ (obsid02) and $kT_{bb} = 1.28$ (obsid03) and, lastly, the photon index $\Gamma = 2.95$ and $\Gamma = 3.33$ (respectively for obsid02 and obsid03).

The fit using the Western Model has a statistic $\text{chisq/d.o.f.} = 578/470$, so it appears that the WM is statistically favored. The coronal temperature is higher than in the case of the Eastern Model and has a value of $kT_e = 13.12$ keV, the temperature of the accretion disk is $kT_{bb} = 1.61$ keV and $kT_{bb} = 1.76$ keV (obsid02 and obsid03), the NS temperature is $kT \approx 0.49$ keV and ≈ 0.5 keV. The photon measured index value is $\Gamma = 3.12$ and $\Gamma = 3.56$ (obsid02 and obsid03).

3.3.2 GX 9+9

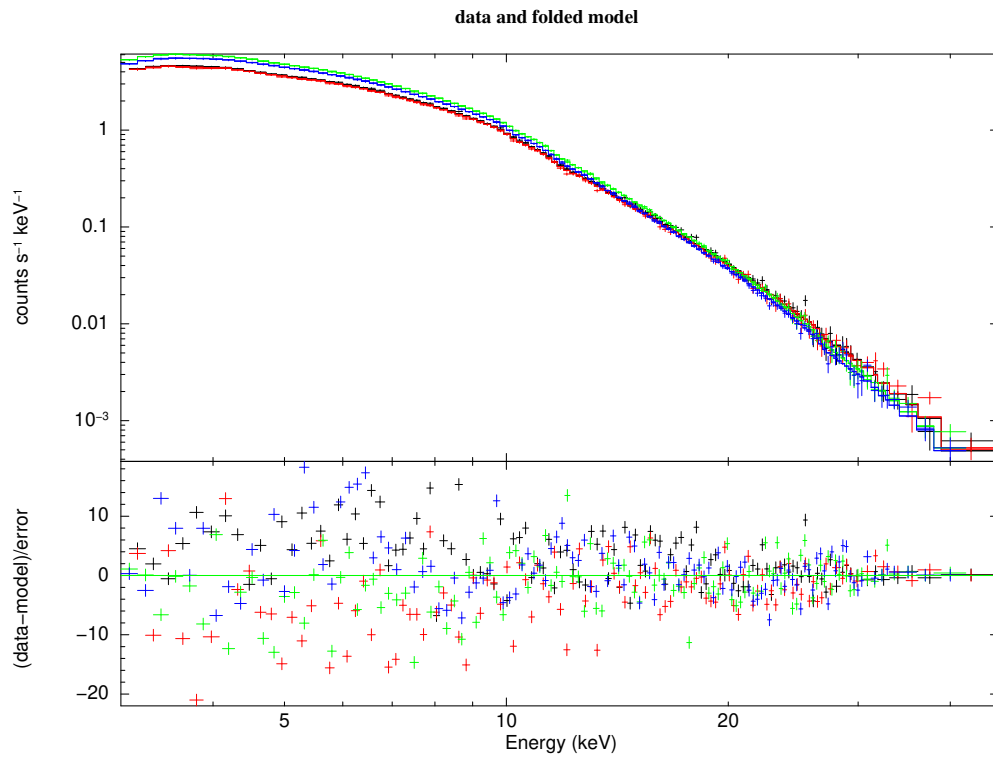
The best-fit parameters for both the Eastern and Western Models are reported in Table 3.3. In the case of the EM, we obtained a fit with a statistic $\text{chisq/d.o.f.} = 404/227$. From this fit we obtained the following values for the temperatures of the source's individual components: temperature of the corona $kT_e = 2.92$ keV, the accretion disk temperature $T_{in} \approx 0.72$ keV and the NS temperature $kT_{bb} = 1.16$ keV. We obtained a photon index of $\Gamma = 2.42$.

As for the Western Model, the fit gives us the coronal temperature is $kT_e = 2.81$ keV, the temperature of the accretion disk is $kT_{bb} \approx 0.3$ keV and $kT \approx 1.6$ keV, the NS temperature is $kT \approx 0.49$ keV, while the photon index is $\Gamma \approx 2$ and the fit statistic $\text{chisq/d.o.f.} = 418/227$. We show the best fit model together with data residuals in the Figure 3.2.

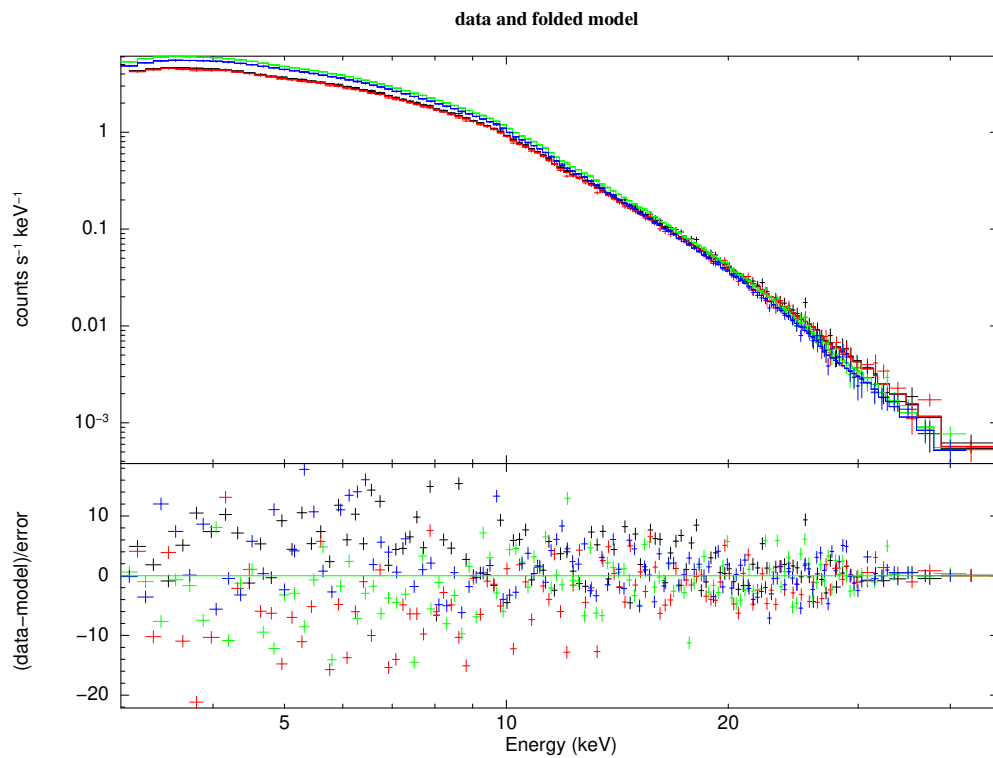
The fit has a reduced χ^2 almost 2 for both the EM and WM, which is statistically not acceptable. This could be due to the presence of an iron line, as apparent from the data residuals (on the $\sim 6 - 7$ keV energy range). We, therefore, add a Gaussian line profile to the used models to account for the presence of the Fe line. The fit obtained using this model has a statistic $\text{chisq/d.o.f.} = 361.71/225$ for the EM and $\text{chisq/d.o.f.} = 367.86/225$ for WM, which is an improvement in both the cases. Despite the χ^2 value not being particularly low, we do not see any obvious features in the residuals (Figure 3.3). Hence, the derived parameters are good enough for the goals of this

Table 3.2. Best-fit values of the accretion disk, corona and neutron star temperatures and the photon index of the GS 1826-238 spectra using the Eastern (EM) and Western Models (WM). Column density nH of the TBabs model component has the value of $0.2 \times 10^{22} \text{ atoms/cm}^2$.

		EM	WM
		obs2 (A)	
const	factor	1	1
diskbb	T_{in}	$0.663^{+0.035}_{-0.034}$	–
	norm	441^{+149}_{-106}	–
bbodyrad	kT	–	$0.486^{+0.022}_{-0.023}$
	norm	–	$1266^{+0.022}_{-0.023}$
	Γ	$2.95^{+0.086}_{-0.074}$	$3.12^{+0.13}_{-0.11}$
nthComp	kT_e	$9.65^{+1.83}_{-1.18}$	$13.12^{+5.85}_{-2.74}$
	kT_{bb}	$1.14^{+0.05}_{-0.04}$	1.61 ± 0.064
	norm	0.027 ± 0.003	$0.013^{+0.006}_{-0.005}$
		obs2 (B)	
const	factor	1.014 ± 0.002	1.014 ± 0.002
		obs3 (A)	
const	factor	1	1
diskbb	T_{in}	0.738 ± 0.017	–
	norm	277^{+34}_{-30}	–
bbodyrad	kT	–	0.515 ± 0.011
	norm	–	966^{+121}_{-102}
	Γ	$3.33^{+0.09}_{-0.08}$	$3.56^{+0.14}_{-0.12}$
nthComp	kT_e	$9.65^{+1.83}_{-1.18}$	$13.12^{+5.85}_{-2.74}$
	kT_{bb}	1.28 ± 0.026	1.76 ± 0.04
	norm	0.023 ± 0.001	0.129 ± 0.003
		obs3 (B)	
const	factor	1.014 ± 0.002	1.014 ± 0.002

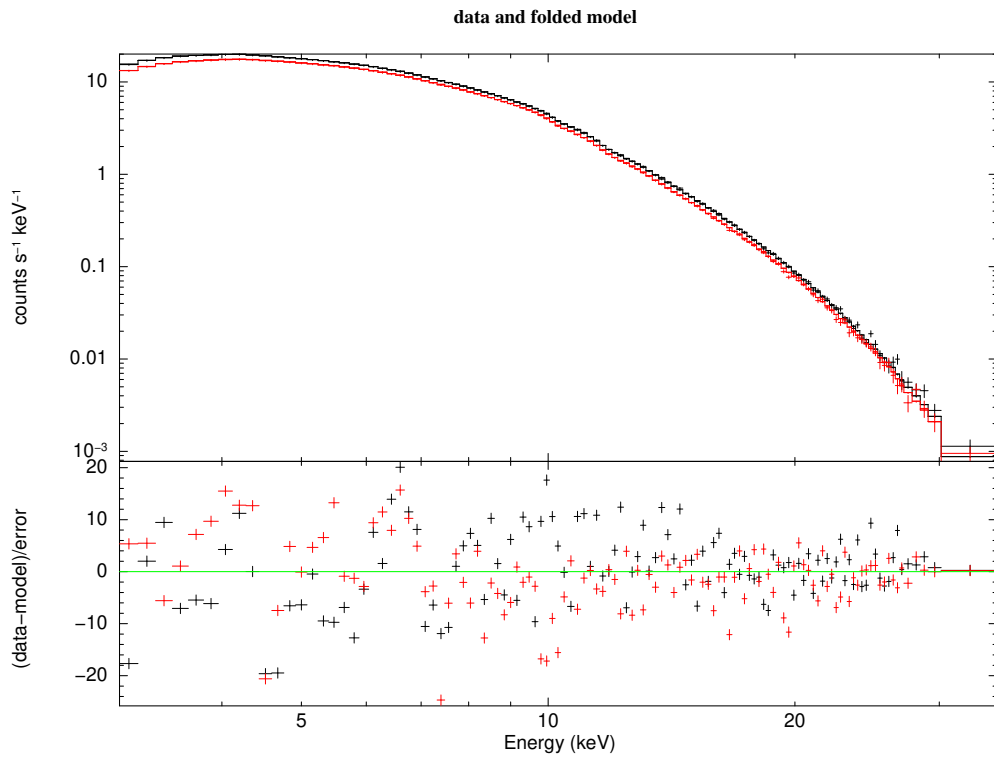


(a)

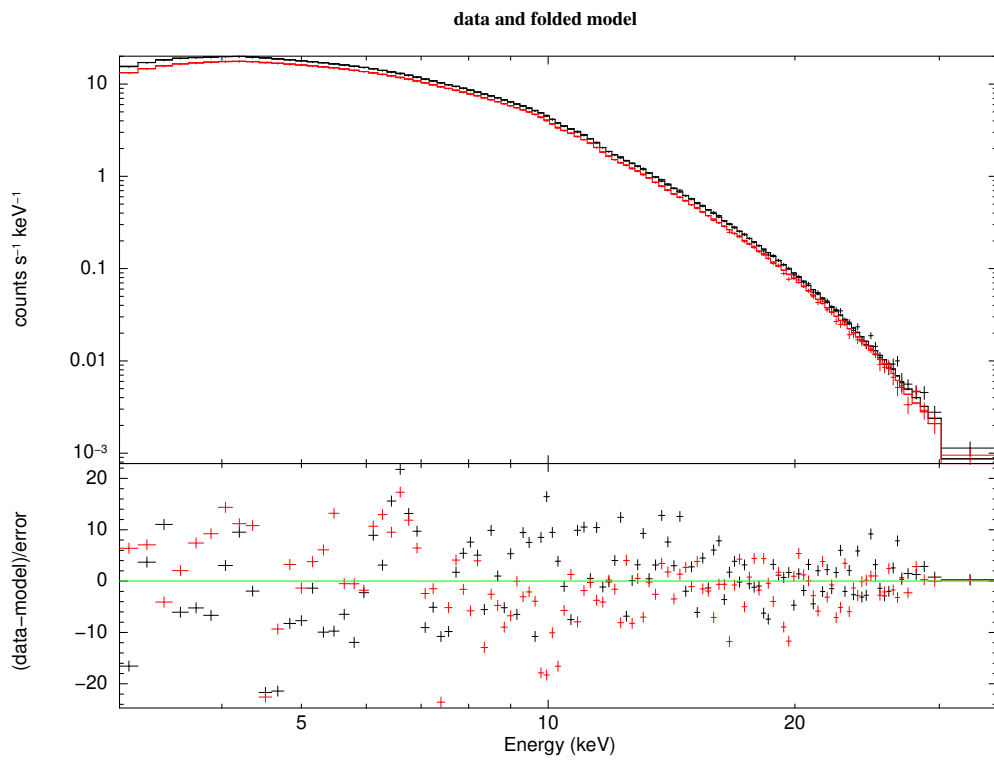


(b)

Figure 3.1. Best fit of the GS 1826-238 source observation using Eastern (a) and Western (b) models (upper panels of both plots) and their data residuals in the sigma units (in the bottom part).



(a)



(b)

Figure 3.2. Best fit of the GX 9+9 source observation using Eastern (a) and Western (b) models (upper panels of both plots) and their data residuals in the sigma units (in the bottom part). We notice an iron line in the data residuals in the 6 - 7 keV band.

study. For the EM, we obtained the coronal temperature $kT_e = 2.92$ keV, disk temperature for the EM is $T_{in} \approx 0.75$ keV, the NS temperature of $kT_{bb} = 1.18$ keV, and the photon index $\Gamma = 2.43$. On the other hand, in the case of WM, we obtained the following: the temperature of corona $kT_e = 2.8$ keV, disk temperature $kT = 1.56$ keV, the NS temperature of $kT_{bb} = 0.42$ keV, and the photon index $\Gamma = 2.4$. We also show the incident model spectrum in the Figure 3.4 (panel (a) showing the model of the EM and in (b) the model of the WM). The best-fit values are reported in the Table 3.3 (the two columns on the right).

3.3.3 Cyg X-2

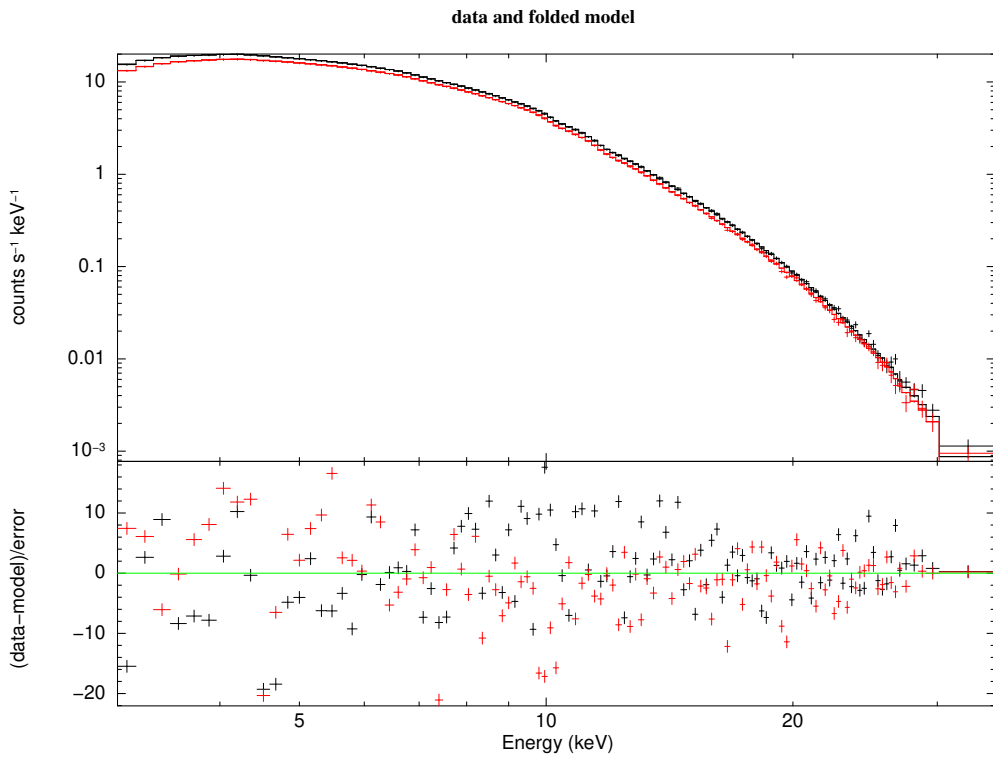
If we fit the data using the same models as in the previous two sources, we notice significant residuals in the interval of $\approx 5.5 - 7.5$ keV (bottom panel of Figure 3.6). This suggests to add another model component in order to account for reflection produced by the Fe $K\alpha$ line. We adjust the previous models by adding the RELXILL or RELXILLCp component (García and Kallman, 2010; García et al., 2011). so the full model we used is either of the following:

- `constant*TBabs*(diskbb+relxill(Cp)+nthComp)`
- `constant*TBabs*(bbodyrad+relxill(Cp)+nthComp)`

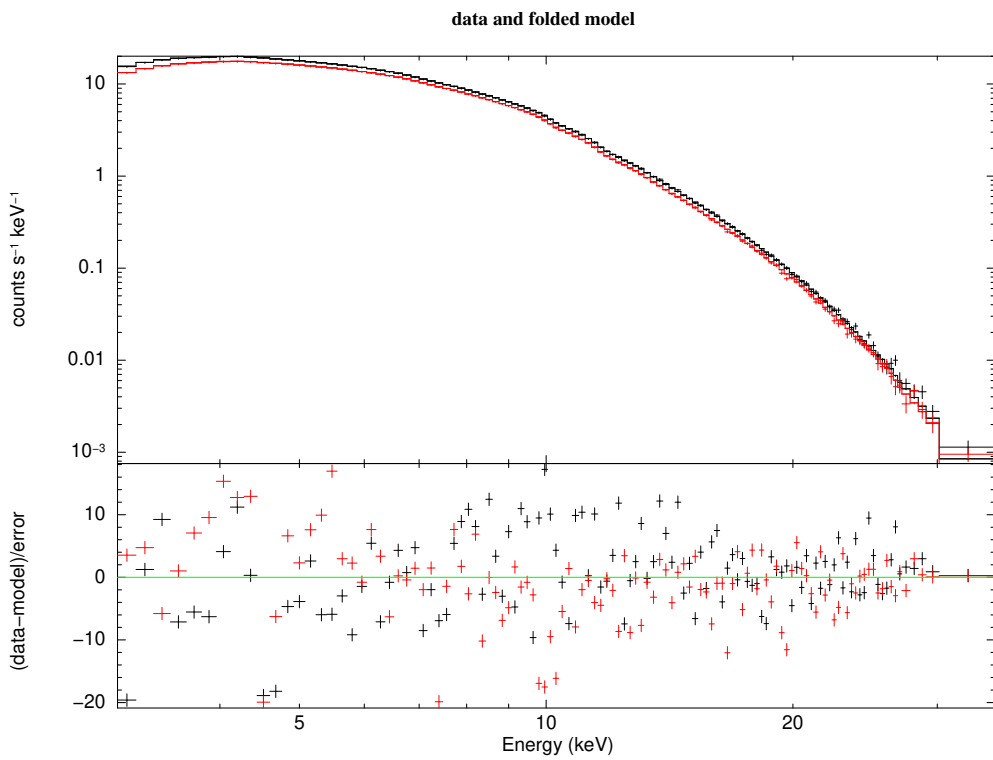
The `relxill` model assumes illumination from a power-law, while `relxillCp` presumes an `nthComp`-like Comptonization continuum with fixed temperature $kT_{bb} = 0.1$ keV.

As our first attempt to fit the data we use the EM with `relxill`. The best-fit we obtained had a statistic $\text{chisq/d.o.f.} = 837.24/456$. The best-fit parameters are reported in Table 3.4 and we show the fit on data together with data residuals in Figure 3.7 (a). Similarly to the first source (WM), the results obtained using this model are rather unusual in the sense that the disk and the NS temperatures are switched. We modified the current model, changing `RELXILL` for `RELXILLCp`. The best-fit parameters are reported in Fig. 3.8 (a). The fit had a statistic $\text{chisq/d.o.f.} = 923.02/454$. Since the reduced chisq is greater than 2, this model is not acceptable to fit the data with and we therefore will exclude it from our considerations.

We again try also the Western Model to see if such a scenario would give us a better fit. The best-fit parameters are reported in Table 3.4 for `relxill` and in Table 3.5 when using the `relxillCp` model. We obtained a fit with a statistic of $\text{chisq/d.o.f.} = 907.03/457$ and $\text{chisq/d.o.f.} = 887.22/474$ for `relxill` and `relxillCp`, respectively. The best-fit and data residuals are reported in the Fig. 3.7 (b) for fit with `relxill` and 3.8 (b) for the fit performed using `relxillCp`. While these results are more promising, than in the previous case, the fact that neither of these models has been successful to fit the reflection Fe line stays bothersome.



(a)



(b)

Figure 3.3. Best fit of the GX 9+9 source observation using Eastern (a) and Western (b) models (upper panels of both plots) and their data residuals in the sigma units (in the bottom part). An additional component fitting the iron line was used.

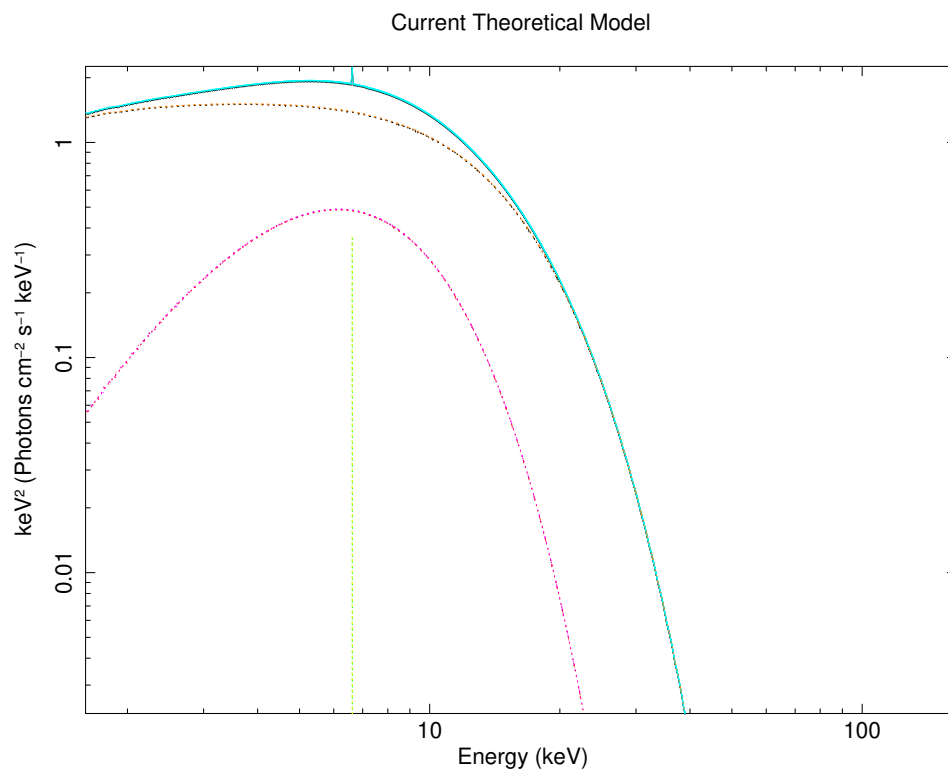
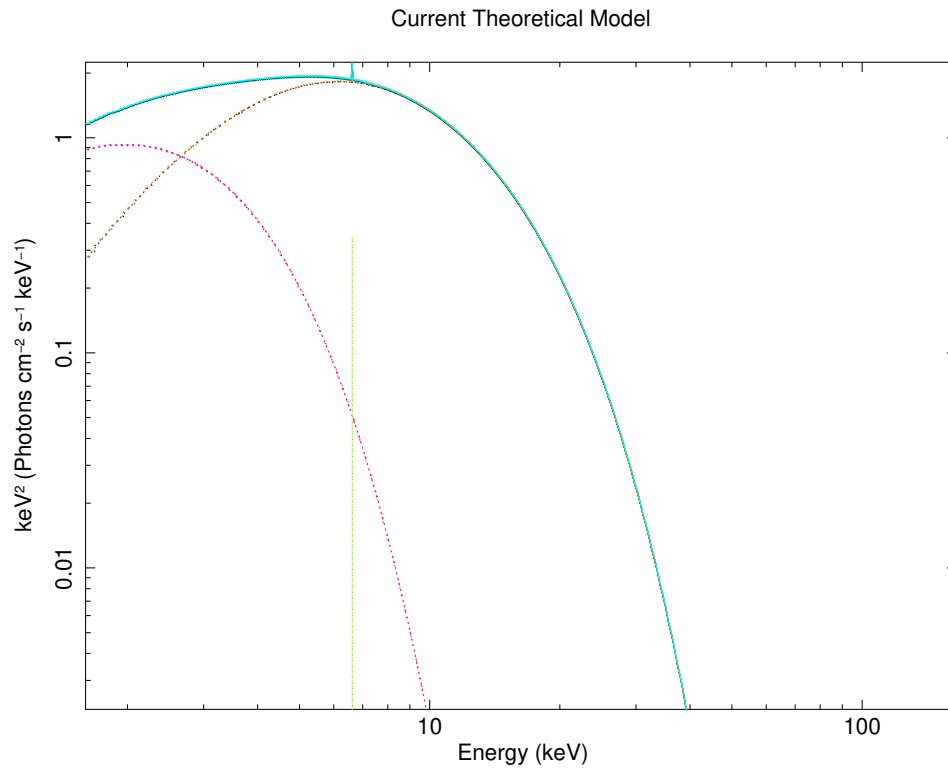


Figure 3.4. Incident model spectrum used to fit the data from an observation of GX 9+9 with the additional model component accounting for the iron line profile. Disk emission or the neutron star blackbody (pink), Comptonization (brown), Gaussian line (green) and the total spectrum (blue).

Table 3.3. Best-fit values of the accretion disk, corona and neutron star temperatures and the photon index of the GX 9+9 spectra using the Eastern (EM) and Western Models (WM). Column density nH of the TBabs model component has the value of $0.2 \times 10^{22} \text{ atoms/cm}^2$.

		EM	WM	EM	WM
		obs2 (A)			
const	factor	1	1	1	1
diskbb	T_{in}	$0.717^{+0.029}_{-0.037}$	–	$0.749^{+0.045}_{-0.032}$	–
	norm	592^{+161}_{-97}	–	484^{+104}_{-103}	–
bbodyrad	kT	–	1.563 ± 0.001	–	$1.574^{+0.04}_{-0.03}$
	norm	–	17 ± 0.05	–	16 ± 1
gauss	linE	–	–	6.6 ± 0.1	6.6 ± 0.1
	norm	–	–	$(3.2 \pm 1) \times 10^{-4}$	$(3.4 \pm 1) \times 10^{-4}$
nthComp	Γ	$2.42^{+0.06}_{-0.07}$	1.9878 ± 0.0004	2.4 ± 0.1	1.99 ± 0.02
	kT_e	2.92 ± 0.05	$2.8131^{+0.0007}_{-0.0003}$	$2.92^{+0.08}_{-0.05}$	$2.81^{+0.03}_{-0.04}$
	kT_{bb}	$1.16^{+0.03}_{-0.04}$	0.2803 ± 0.064	$1.82^{+0.06}_{-0.04}$	$0.42 \pm u$
	norm	$0.108^{+0.009}_{-0.007}$	1.342 ± 0.001	0.1 ± 0.01	0.96 ± 0.1
		obs2 (B)			
const	factor	1.007 ± 0.001	1.007 ± 0.001	1.007 ± 0.001	1.007 ± 0.001

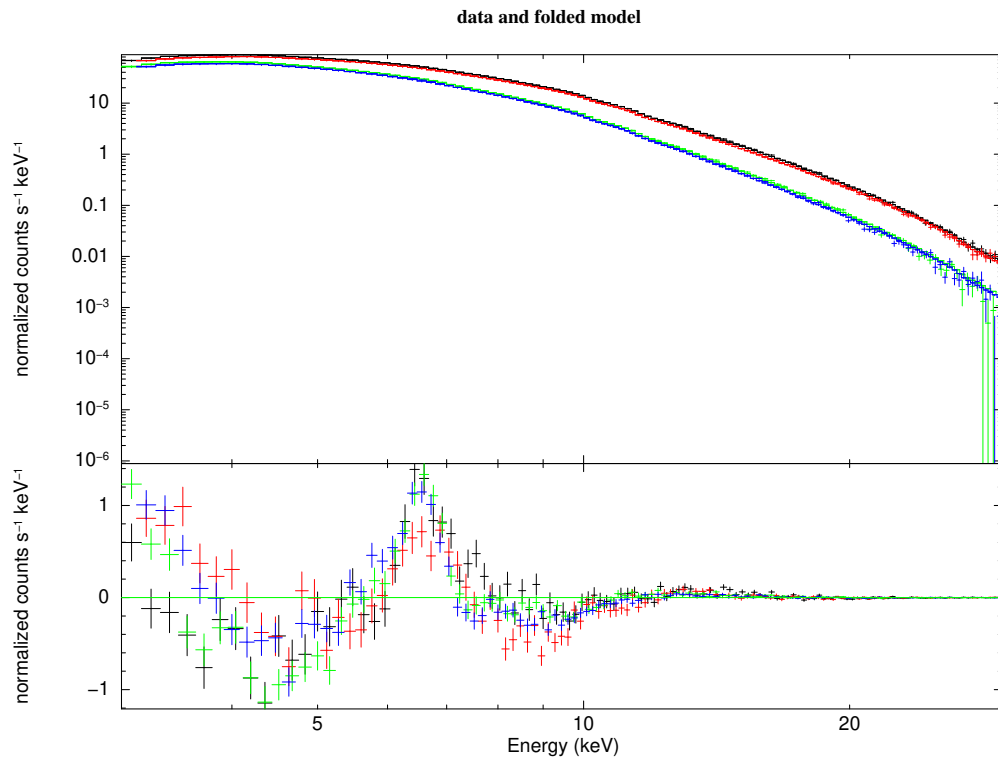


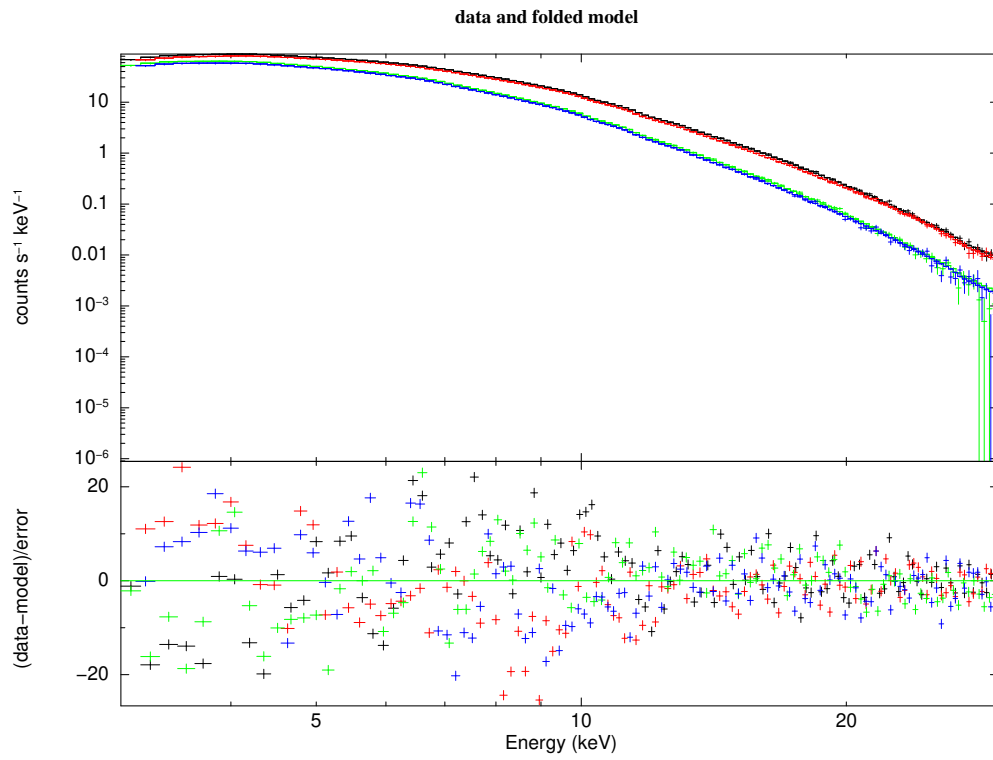
Figure 3.6. Cyg X-2 fit (upper panel) and its data residuals (bottom) using a model without relativistic reflection. We observe strong residuals around the energy of $\approx 5.5 - 7.5$ keV.

We will try using another variation of the model named `relxillNS` (García et al., 2022), which considers reflection of a blackbody spectrum (with temperature kT_{bb}). The main advantage of the model and its applicability is the fact that it is created in order to specifically suit to model X-ray radiation emitted from the vicinity of the neutron stars. In this case for simplicity, we use an EM-like model. There is some spectral variability, as seen in Figure 1 in Ludlam et al. (2022), therefore we do not perform a joint fit of the two intervals. We studied the observation in two intervals (hereafter referred to as `int1` and `int2`). During the analysis we used the following model:

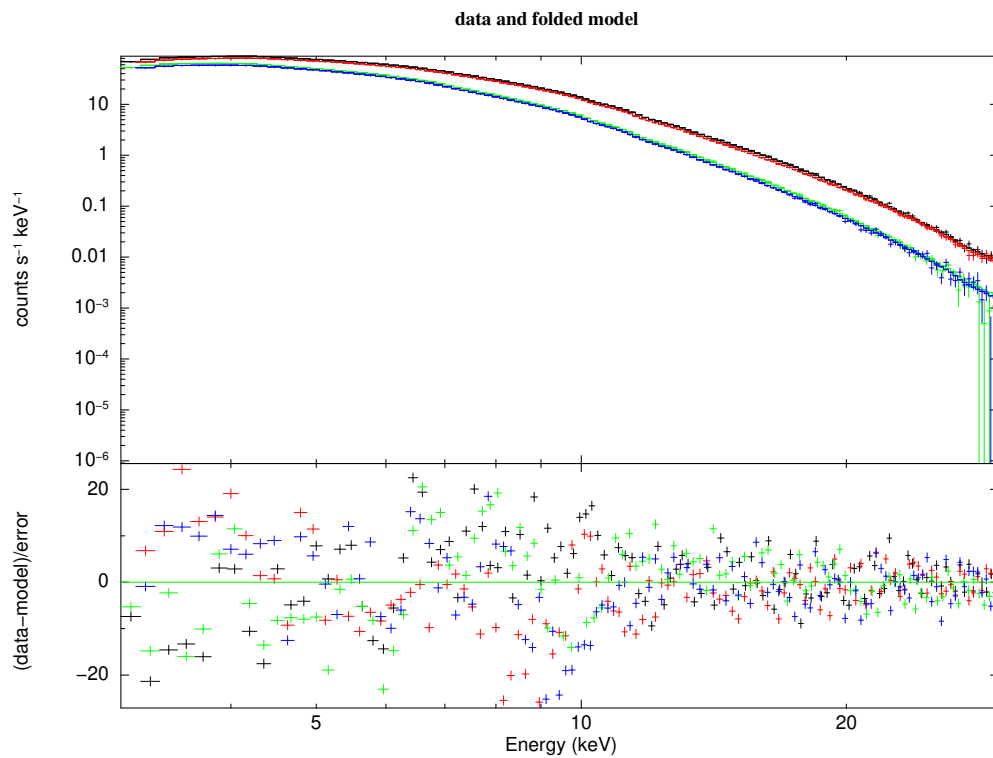
- `int1: constant*TBabs(diskbb+relxillNS+nthComp)`
- `int2: constant*TBabs(diskbb+relxillNS+gaussian+nthComp)`

Now we explain the reason behind the slight difference between the two used models. Generally, omitting the `gaussian` component will result in an improper fit of the Fe line, therefore seems to be an important constituent. While for the `int2` such a model works very well and gives us the goodness of the fit $\text{chisq/d.o.f.} = 303.45/221$, the `int1` is much more difficult to fit. Such a model results in a fit of chisq greater than 2, which is not acceptable. Deleting this component from the model, we are able to converge to an improved fit of $\text{chisq/d.o.f.} = 444.7/230$ (see panel (a) of the Figure 3.9 for `int1` for the best fit and the data residuals, and panel (b) of the same figure for `int2`). In this case, unfortunately, the Fe line is not well fit, which can be seen on the plotted incident model spectrum in the panel (a) of the Figure 3.10, as solely `relxillNS` does not fit this part of the spectrum well. We show a similar plot of the `int2` in panel (b) of the same figure. Here, we see a clear iron line at ≈ 6.5 keV being fit in the second interval of the observed spectrum (we used a Gaussian profile for this data set, as was previously mentioned). The best fit parameters for both the intervals are reported in the Table 3.6.

For the sake of modeling the reflection spectrum, we make use of `RELXILLNS`, which studies illumination from a blackbody spectrum, and for the temperature of the blackbody, we assume the same, as for the seed photons from the corona. Therefore, we tie the two kT_{bb} temperatures to each other (in `RELXILLNS` to the one in `NTHCOMP`). Moreover, it follows from the results above, that the temperature is unconstrained, so we cannot leave this parameter as entirely free. It is clear from the panel (a) of the Figure 3.9, that there is a discrepancy present in the residuals, especially in the 3 - 4 keV band of the `int1`. As there might be some issue related to the calibration of the two instruments, we excluded this part from the analysis. We report the results of the two intervals fit separately in the two right columns of the Table 3.6 and in the Figures 3.11. From the first interval we obtained a fit of $\text{chisq/d.o.f.} = 305.48/216$ and for the second one $\text{chisq/d.o.f.} = 305.21/222$. Both of these fit statistics represent a significant improvement with respect to the previous

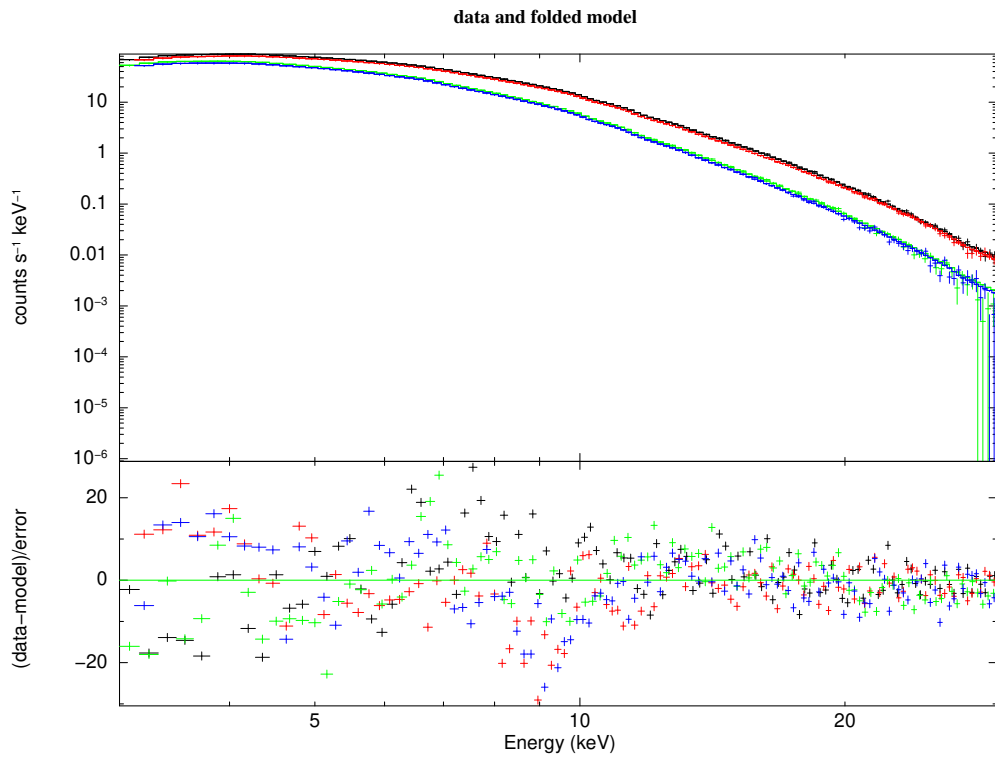


(a)

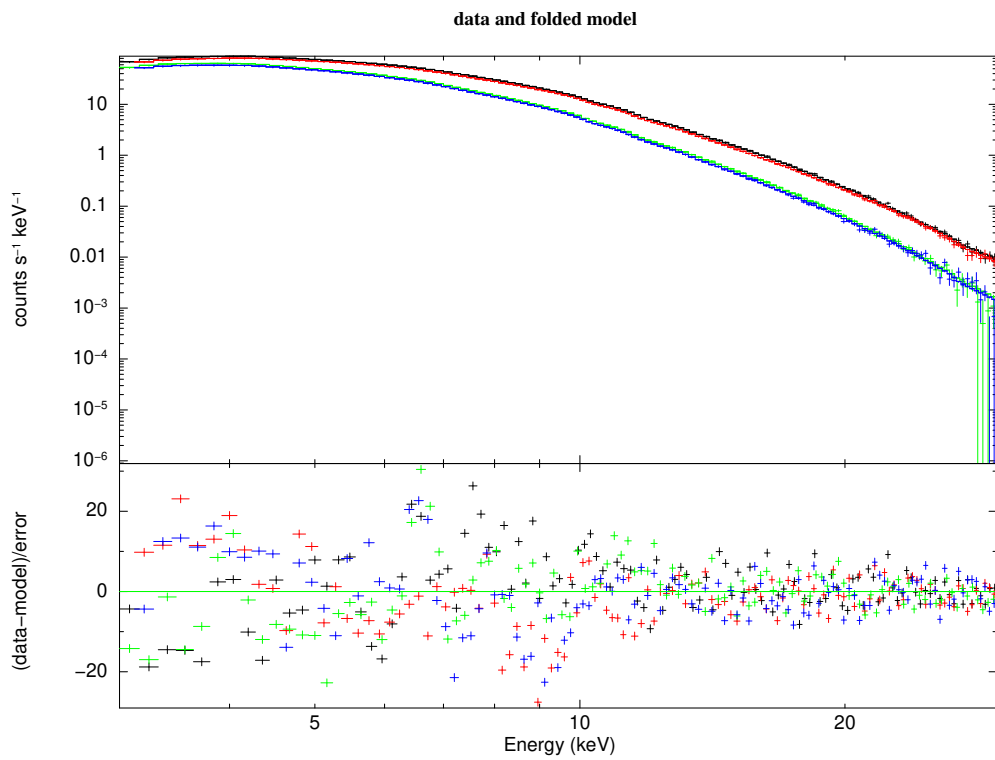


(b)

Figure 3.7. Best fit of the Cyg X-2 source observation using Eastern (a) and Western (b) models (upper panels of both plots) and their data residuals in the sigma units (in the bottom part). The fit was performed using the relativistic reflection model `relxill`.



(a)



(b)

Figure 3.8. Best fit of the Cyg X-2 source observation using Eastern (a) and Western (b) models (upper panels of both plots) and their data residuals (in the bottom part). The fit was performed using the relativistic reflection model `relxillCp`.

fits. Despite the fit not being completely satisfactory, we do not recognize any other spectral components in the data residuals. For example, the model presented in Ludlam et al. (2022) contains more spectral components than the model we used, which is probably the reason behind the better fit. Moreover, we have tried using different models, for example `relconv * nthComp` instead of `relxillNS`, but were not successful in obtaining a better fit. Nevertheless, the analysis of these observations is still a work in progress.

3.4 Discussion and conclusions

We obtained acceptable fits with both the Western and Eastern models in the case of GS 1826-238. While the Western Model gives us statistically a slightly better fit of $\text{chisq/d.o.f.} = 578/470$ (compared to $593/470$ in the case of EM), there are several issues with the results obtained. First, the NS temperatures are a bit too low. Here, we would expect the temperature of $\approx 1 - 1.5$ keV, but are only getting ≈ 0.5 keV in both observations. Moreover, the temperatures obtained for the accretion disk and the NS are switched. Naturally, we are expecting the NS to have a higher temperature than the accretion disk. If we try switching these two temperatures for one another, we obtain statistically a worse fit of $\text{chisq/d.o.f.} = 971/474$, with higher residuals, as can be seen in the bottom panel of the Figure 3.13 (energy interval $\lesssim 7$ keV). For these reasons, we conclude that the Western Model is not suitable for fitting this source, while the Eastern Model is more favored.

The two models (Eastern and Western Models) in the case of GX 9+9 are quite similar in the characteristics of the source, as well as the goodness of the fit we obtained. However, the disk temperature of $kT_{bb} \approx 0.3$ keV is a little low for what we would expect in the case of the Western Model. Nevertheless, since we get similar results from the two models, we are not able to confidently conclude the geometry of the corona in the studied source.

Cyg X-2 was a source quite difficult to fit. We used a model containing a relativistic reflection component (`relxill` and its variations). While this is still a work in progress, the most promising scenario seems to be using `relxillNS` in combination with the Gaussian line profile for the second studied interval (`int2`). In the first interval of the analyzed observation (`int1`) we did not obtain a statistically satisfactory fit using an additional `gauss` component (the best-fit has a `chisq` greater than 2). Removing this component from the model will result in an acceptable fit statistically. However, such a model fails to correctly fit the Fe line. A significant improvement for both the intervals is achieved when we tie the blackbody temperature kT_{bb} between `relxillNS` and `nthComp`. In this case, we are able to fit the Fe line also in the `int1`. Statistically, this last case offers the best fit, albeit with quite a high photon index and the coronal temperature (`int1`).

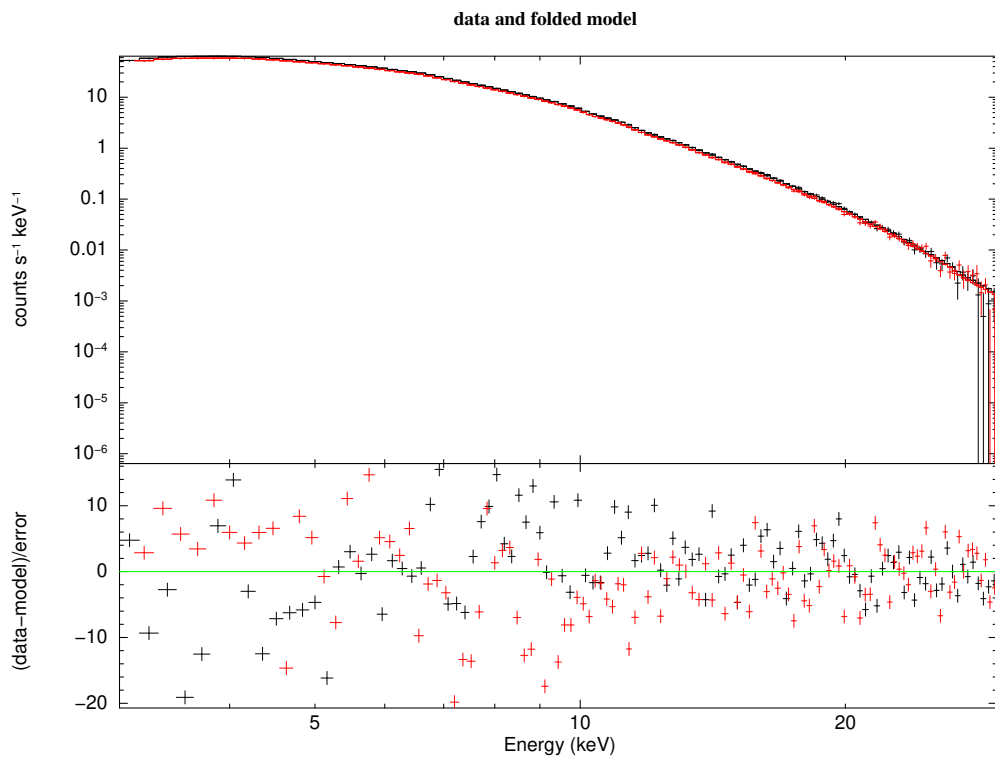
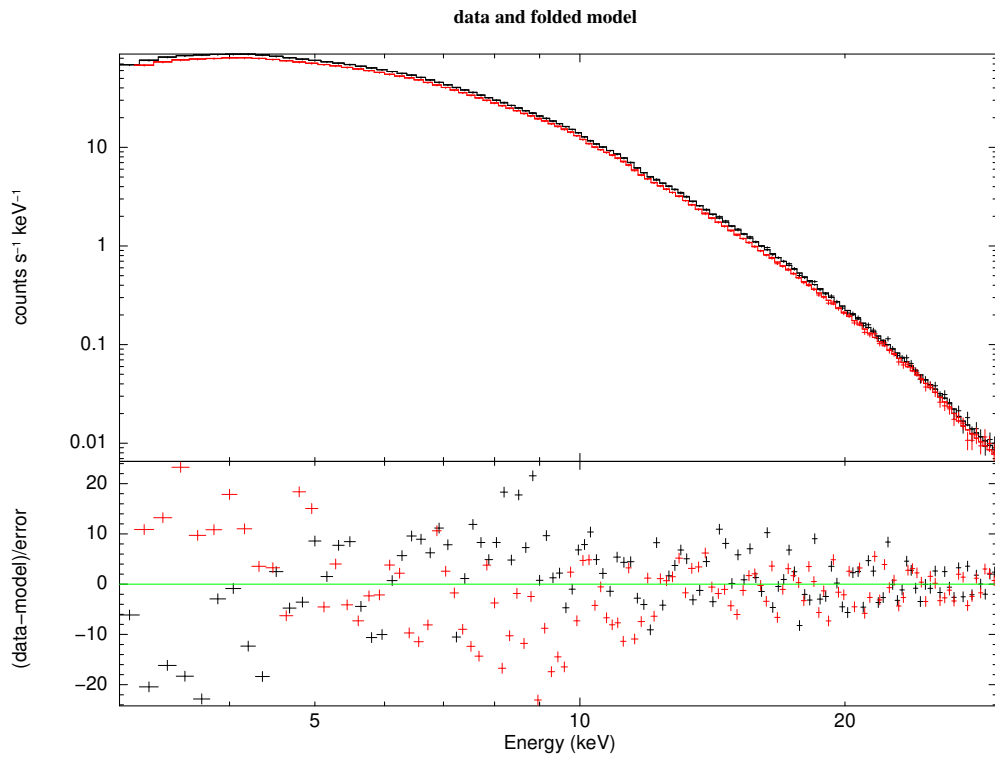


Figure 3.9. Best fit of the Cyg X-2 source observation in the upper panel and data residuals in the sigma units in the bottom panel for int1 in (a) and int2 in (b). The fit was performed using the relativistic reflection model `relxillNS`.

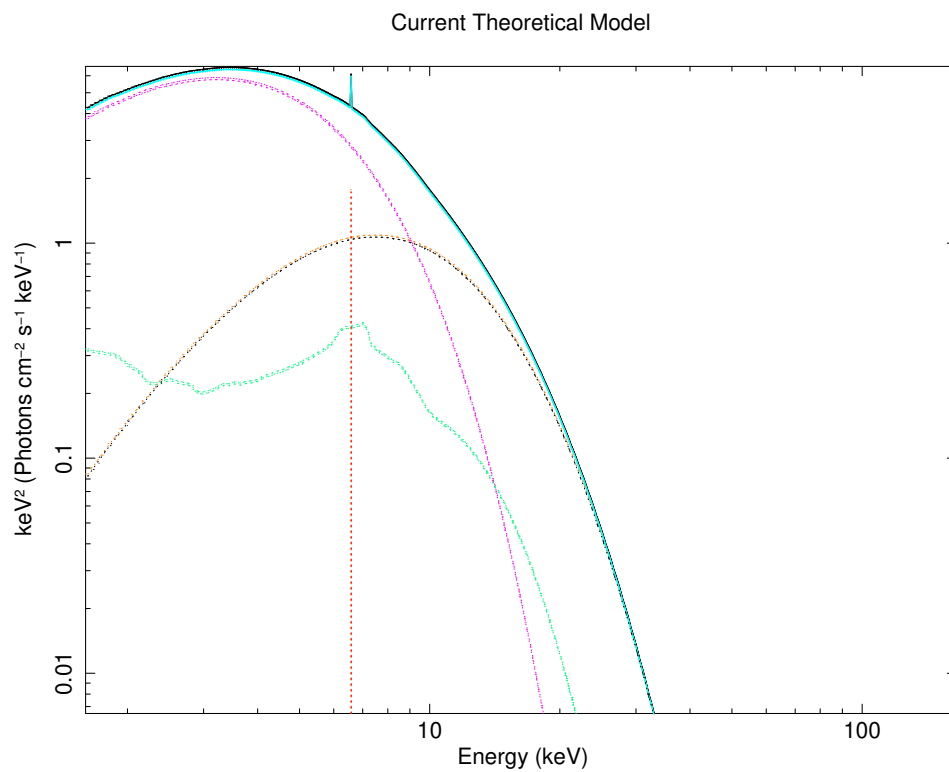
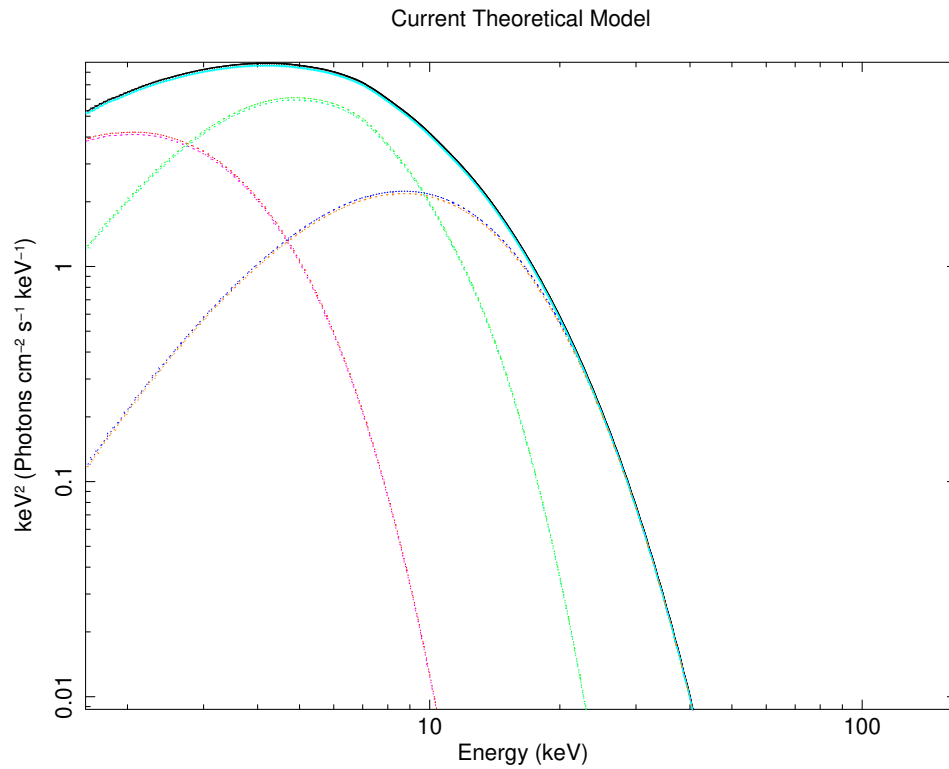
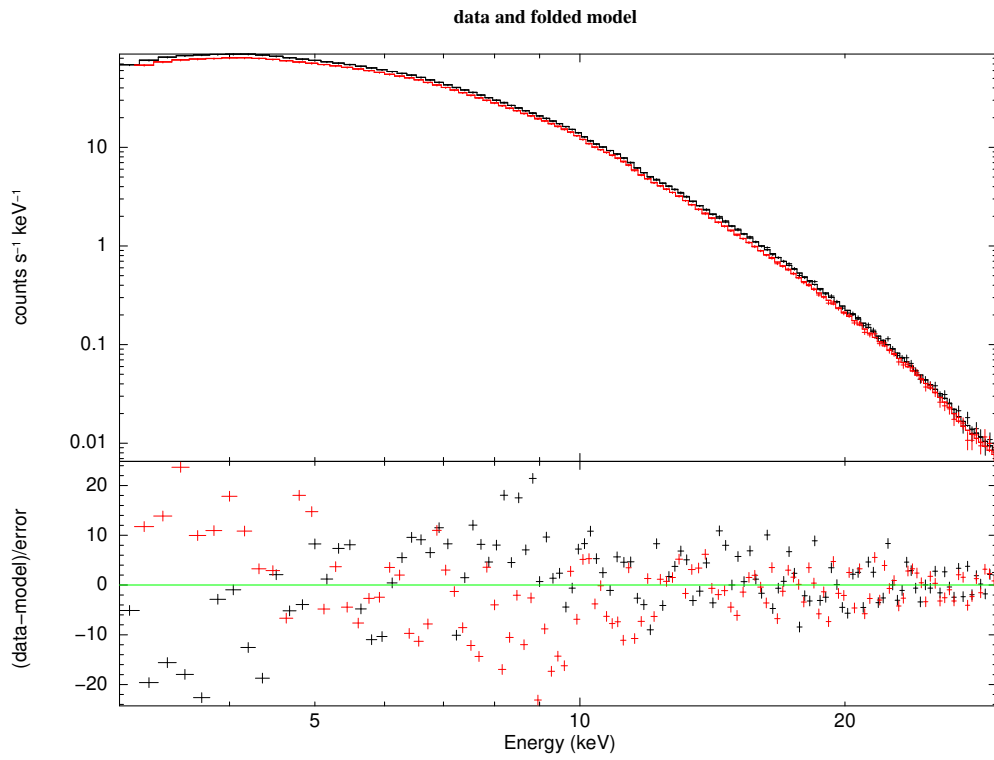
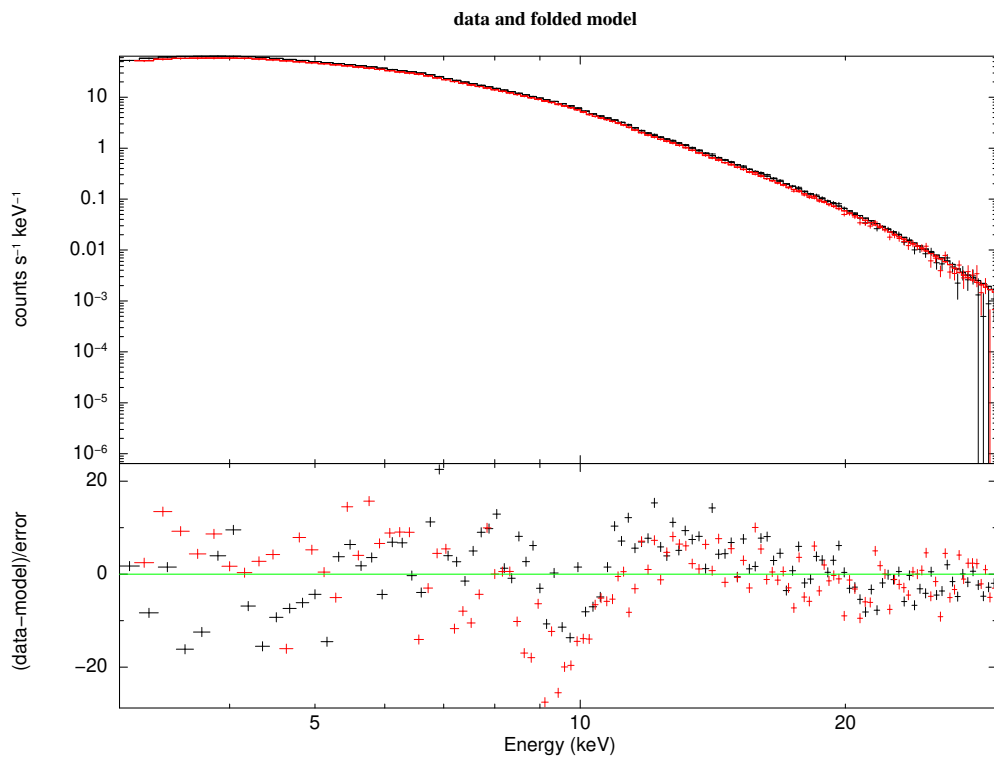


Figure 3.10. Incident model spectrum used to fit the int1 (a) without the Gaussian line profile and int2 (b) including the gaussian line profile in order to fit the relativistic Fe line. The fit was performed using the relativistic reflection model `relxillNS`. Disk emission (pink), Comptonization (orange/dark blue), `relxillNS` (green), Gaussian line (red) and the total spectrum (black/blue).



(a)



(b)

Figure 3.11. Best fit of the Cyg X-2 source observation in the upper panel and data residuals in the sigma units in the bottom panel for int1 in (a) and int2 in (b). The fit was performed using the relativistic reflection model `relxillNS` with the blackbody temperatures tied together.

Table 3.4. Best-fit values of the accretion disk, corona and neutron star temperatures, inner radius of the accretion disk and its ionization, and the photon index of the Cyg X-2 spectra using the Eastern (EM) and Western Models (WM). The fit was performed using the relativistic reflection model `relxill`. Column density nH of the `TBabs` model component has the value of $0.2 \times 10^{22} \text{ atoms/cm}^2$. u - error is unconstrained.

		EM	EM	WM	WM
		int1 (A)	int2 (A)	int1 (A)	int2 (A)
const	factor	1	1	1	1
diskbb	T_{in}	1.872±0.001	2.656±0.012	–	–
	norm	31.24±0.06	0.39±0.01	–	–
bbodyrad	kT	–	–	1.25±0.03	2.156±0.002
	norm	–	–	166 ⁺²⁸ ₋₂₁	7.65±0.03
	R_{in}	94 ^{+u} ₋₂₇	100 ^{+u} ₋₃	100 ^{+u} ₋₂₄	84 ^{+u} ₋₁₅
relxill	$\log \xi$	4.35±0.02	3.855±0.005	4.24±0.01	2.69±0.03
	norm	0.0613±0.0002	0.98±0.01	0.0360±0.0001	2.37±0.03
	Γ	2.276±0.001	3.181±0.001	2.072±0.001	9.3±0.1
nthComp	kT_e	2.70±0.04	2.555±0.005	2.467±0.003	2.60±0.04
	kT_{bb}	0.8278±0.0003	0.8084±0.0002	0.909±0.001	1.3489±0.0005
	norm	0.565±0.001	0.904±0.001	2.152±0.002	2.6870.002
		int1 (B)	int2 (B)	int1 (B)	int2 (B)
const	factor	0.976±0.001	0.976±0.001	0.976±0.001	0.976±0.001

Table 3.5. Best-fit values of the accretion disk, corona and neutron star temperatures, inclination of the source, inner radius of the accretion disk and its ionization, and the photon index of the Cyg X-2 spectra using the Eastern (EM) and Western Models (WM). The fit was performed using the relativistic reflection model `relxillCp`. Column density nH of the `TBabs` model component has the value of $0.2 \times 10^{22} \text{atoms/cm}^2$. f - parameter was frozen for the fit. u - error is unconstrained.

		EM	EM	WM	WM
		int1 (A)	int2 (A)	int1 (A)	int2 (A)
const	factor	1	1	1	1
diskbb	T_{in}	1.100 ± 0.001	0.01_{-u}^{+u}	–	–
	norm	214 ± 1	10^{24+u}_{-u}	–	–
bbodyrad	kT	–	–	1.073 ± 0.001	0.996 ± 0.003
	norm	–	–	363 ± 1	750 ± 1
	$i [^\circ]$	77 ± 1	23_{-3}^{+4}	60^f	60^f
relxillCp	R_{in}	100_{-10}^{+u}	100_{-16}^{+u}	$63.6_{-15.8}^{+22.6}$	$100_{-2.48}^{+u}$
	$\log \xi$	3.478 ± 0.005	3.456 ± 0.004	3.717 ± 0.006	3.97 ± 0.01
	norm	0.332 ± 0.002	0.69 ± 0.01	0.114 ± 0.001	0.292 ± 0.002
	Γ	$2.6230.001$	3.257 ± 0.001	2.520 ± 0.001	3.009 ± 0.002
nthComp	kT_e	2.727 ± 0.003	$2.7240.004$	2.590 ± 0.003	2.37 ± 0.01
	kT_{bb}	1.0579 ± 0.0003	0.8361 ± 0.0002	1.731 ± 0.001	2.017 ± 0.002
	norm	0.5212 ± 0.0004	$0.8870.001$	1.331 ± 0.001	0.479 ± 0.001
		int1 (B)	int2 (B)	int1 (B)	int2 (B)
const	factor	0.977 ± 0.001	0.977 ± 0.001	$0.9770.001$	$0.9770.001$

Table 3.6. Best-fit values of the accretion disk, corona and neutron star temperatures, inner radius of the accretion disk and its ionization, Fe line energy, and the photon index of the Cyg X-2 spectra. The fit was performed using the relativistic reflection model `relxillNS`. Column density nH of the `TBabs` model component has the value of $0.2 \times 10^{22} \text{ atoms/cm}^2$. u - error is unconstrained, t - parameter is tied to the kT_{bb} parameter of the `nthComp` model.

		M1	M1	M2	M2
		int1 (A)	int2 (A)	int1 (A)	int2 (A)
const	factor	1	1	1	1
diskbb	T_{in}	0.7 ± 0.1	$1.27^{+0.05}_{-0.04}$	1.45 ± 0.04	$1.01637^{+0.15}_{-0.14}$
	norm	2376^{+1293}_{-1145}	309^{+7}_{-10}	230^{+19}_{-18}	522^{+267}_{-142}
	R_{in}	$10.3^{+1.5}_{-1.7}$	100^{+u}_{-13}	$12.65^{+2.69}_{-2.06}$	100^{+u}_{-13}
relxillNS	kT_{bb}	$1.37^{+0.05}_{-0.04}$	$1.09960^{+0.05}_{-0.03}$	1.86706^t	1.05235^t
	$\log \xi$	$4.66^{+u}_{-4.66}$	$2.14720^{+0.08}_{-0.06}$	1.7 ± 0.1	$2.17^{+0.09}_{-0.07}$
gauss	norm	0.0224 ± 0.001	$0.085^{+0.001}_{-0.001}$	$(3.74 \pm 1) \times 10^{-3}$	0.990 ± 0.001
	linE	–	$6.57^{+0.05}_{-0.01}$	$6.48001^{+0.08}_{-0.04}$	$6.59^{+0.04}_{-0.03}$
	norm	–	$0.0011^{+0.0002}_{-0.0001}$	$(1.26 \pm 0.3) \times 10^{-3}$	$(1.1 \pm 0.2) \times 10^{-3}$
nthComp	Γ	$7.16428^{+0.85}_{-1.20}$	$5.9^{+3.2}_{-1.1}$	$6.33^{+0.46}_{-1.88}$	$2.89^{+0.14}_{-0.31}$
	kT_e	918^{+u}_{-917}	$5.1^{+0.7}_{-1.2}$	$57.97^{+u}_{-56.97}$	$2.75529^{+0.09}_{-0.08}$
	kT_{bb}	$2.11^{+0.06}_{-0.04}$	1.8 ± 0.1	$1.91^{+0.02}_{-0.12}$	$1.05^{+0.08}_{-0.06} x$
	norm	$0.037^{+0.005}_{-0.007}$	0.03 ± 0.01	0.06 ± 0.02	$0.25^{+0.11}_{-0.12}$
		int1 (B)	int2 (B)	int1 (B)	int2 (B)
const	factor	0.975 ± 0.001	0.978 ± 0.001	0.972 ± 0.001	0.978 ± 0.001

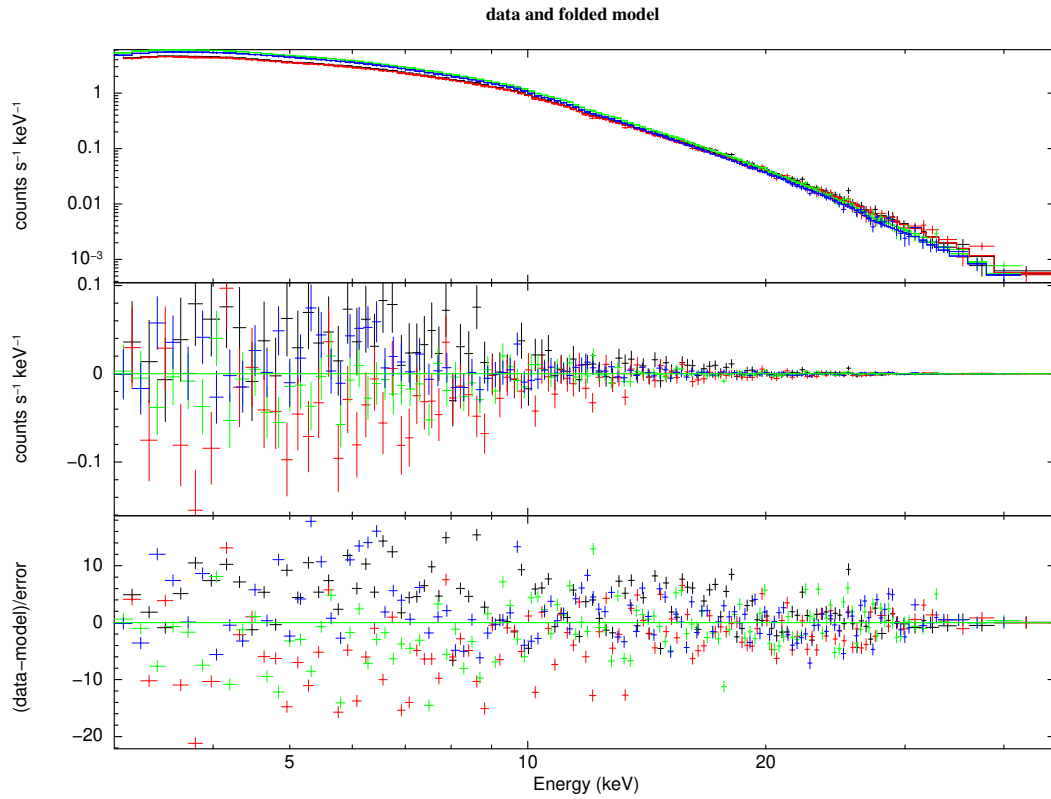


Figure 3.13. Fit of the GS 1826-238 source observation using the Western model after switching the accretion disk and NS temperatures. We notice very apparent residuals (middle sub-panel) from the model on energies $\lesssim 10$ keV. In this scenario we do not obtain an acceptable fit, which is also apparent from the residuals in sigma units (bottom sub-panel).

In this chapter we have presented the spectral properties of these sources, which is essential to interpret the polarimetric data. In Chapter 4 we will discuss the results of the IXPE observations of these sources.

Chapter 4

IXPE observations of X-ray binaries

.non est ad astra mollis e terris via

The launch of the Imaging X-ray Polarimetry Explorer on December 9, 2021 has truly opened a new window for studying X-ray astrophysical sources. So far, the telescope performed 64 observations of 46 sources ¹. Out of these, there have been several X-ray binary system observations, that we will summarize below.

4.1 Black Hole X-ray Binaries

4.1.1 Cyg X-1

Cyg X-1 is a persistent source very bright in the X-ray energy band. It was observed with the IXPE telescope on May 15 - 21, 2022 for a total of 242 ks, then on June 18 - 20, 2022 for 86 ks as a target of opportunity observation. The measured polarization degree of the source is $PD = 4.01 \pm 0.20\%$ and the polarization angle $PA = -20.7 \pm 1.4^\circ$ (Krawczynski et al., 2022). Both of these results are consistent with the previous measurement performed by the *OSO-8* satellite (Long et al., 1980), albeit that result was also marginally significant statistically. There is a evidence that the PD increases with energy, as well as with the source flux. In Krawczynski et al. (2022) they also report that the PA is in alignment with the radio jet (within 5°), which implies a direct relation of the inner X-ray emitting region to the radio jet. As a matter of fact, this supports the hypothesis that jets in both quasars and microquasars are perpendicular to the inner accretion flow. The source was in the LHS during the observations, with a photon index of $\Gamma = 1.6$. The polarimetric observations give the possibility to reach some conclusions regarding the geometry of the system. Two models are allowed by the data:

¹as of January 31, 2023

- The hot corona surrounds the accretion disk in a "sandwich" model (see Figure 1.17 in the Section 1.3)
- An outer cold, truncated, optically thick and geometrically thin accretion disk is present, together with an inner optically thin and geometrically thick, extended region of hot plasma

In the case that the jet would be launched from the inner region of the disk, it would be possible for the jet to create conditions for an optically thin and radially extended corona. The polarimetric observations exclude the possibility for the coronal geometry to be a narrow cone of plasma along the axis of the jet, nor can it comprise of two compact regions above and below the black hole. In such cases, the PD would be much lower than the measured value. Moreover, the PA would be perpendicular to the jet (Figure 3 (a) in Krawczynski et al. (2022)). The measured PD is also higher than predicted ($\sim 1\%$) from the measured orbital inclination of 27° , which suggests either a higher inclination (and, therefore, a more edge-on view), or some unknown phenomena leading to the formation of the X-ray emission from accreting X-ray BH sources (Krawczynski et al., 2022).

4.1.2 4U 1630-47, LMC X-1, Cyg X-3

Three XRB sources with a black hole as a compact object have recently been observed with IXPE: 4U 1630-47, LMC X-1 and Cyg X-3. Since the data analysis and interpretation is still ongoing, we will only mention here some preliminary results.

4U 1630-47: IXPE observed this XRB on August 23, 2022 - September 2, 2022 with the duration of the observation of 460 ks. It was a Target of Opportunity observation, after this transient source went into outburst. The analysis of the data is still in progress. Nevertheless, the preliminary results report the source being in thermal state with a clear measurement of polarization, likely increasing with energy in the 2 - 8 keV band (Ratheesh et al., in prep.). The interpretation of this measurement (whether the high polarization is due to disk emission, returning radiation, or some other mechanism) is still not finished, but the conclusion that 4U 1630-47 is a source with high inclination seems inescapable due to the high PD.

Cyg X-3: The observation of the persistent source Cyg X-3 took place on October 14, 2022 for a duration of 275 ks and on December 25, 2022 for 198 ks (the latter observation was carried out as a target of opportunity, as the source was reported to be brighter. The source was found in reflection-dominated state, due to the presence of a strong iron line, and, unsurprisingly, presents a very high polarization degree (Veledina et al., in prep.).

LMC X-1: This persistent source was observed on October 19, 2022 with the observation duration of 562 ks. The source was found in the hard state. While

no polarization was measured, the upper limit to the polarization degree is very tight, $\sim 1\%$ (Podgorny et al., in prep.), strongly suggesting that LMC X-1 is a low-inclination source.

4.2 Neutron Star Low-Mass X-ray Binaries

4.2.1 GS 1826-238

On March 29 - 31, 2022, the IXPE satellite observed the first weekly magnetized NS-LMXB, the atoll source GS 1826-238, for an exposure time of 85 ks. The source was found in the high/soft state. The observation provided only an upper limit, which is $PD = 1.3\%$ (in the 2 - 8 keV channel), $PD = 1.6\%$ (in the 2 - 4 keV channel) and $PD = 2.4\%$ (in the 4 - 8 keV channel) (Capitanio et al., 2022). The polarization angle for this observation was unconstrained in all three of those channels. As we don't have an information on the direction of the jet, we cannot put constraints on the PA and disk orientation. There are also no suggestions of a time variability of the Stokes parameters. Based on the upper limit on the polarization degree, some assumptions on the geometry can be drawn based on simulations performed using the best-fit parameter from spectral analysis:

- Corona in a shape of a pseudo-torus (Gnarini et al., 2022): a torus of a rectangular shape with similar scale in the vertical and horizontal directions, rotating together with the accretion disk. Gnarini et al. (2022) report this coronal geometry to only cover the accretion disk up to $\sim 15r_g$, but the vertical thickness covers almost the entire surface of the NS
- Wedge geometry of the corona: a conically-shaped part of a torus surrounding the equator of the NS and located between the accretion disk and the surface of the neutron star. The torus section is connected to both the surface of NS and the inner part of the accretion disk (extending 6 - 8 r_g) (see Figure 1.18, panel (a))
- Shell geometry of the corona: a spherically shaped corona surrounding the neutron star (see Figure 1.18, panel (b))

Since in the first considered case (pseudo-toroidal geometry), the accretion disk photons only dominate on the lower energies, and, therefore, its potential polarization would not have a significant effect on the net polarization of the source. Consequently, a limit on the system inclination could be derived: $i \lesssim 47^\circ$ ((Capitanio et al., 2022), right panel of Figure 6). For this type of geometry, the PA would be misaligned and non-perpendicular to the accretion disk. In the case of the wedge-shaped corona, the polarization degree only somewhat changes based on the presence/absence of intrinsic polarization. In this case, the inclination should be $i \lesssim 42^\circ$ and $i \lesssim 39^\circ$, respectively. PA should be misaligned by $\approx 25^\circ$ for this coronal geometry. As for the shell geometry of the corona, PD should considerably change depending on the

presence or absence of intrinsic polarization, and the PA would always be parallel to the accretion disk. As a matter of fact, the PD should be below 1% for unpolarized disk seed photons irrespective on the system inclination. In the reverse scenario, with the seed photons being intrinsically polarized, the inclination should have a limit of $i \lesssim 62^\circ$.

Previous observations suggest the inclination of $i = (69_{-3}^{+2})^\circ$ (Johnston et al., 2020) and $i = (62.5 \pm 5.5)^\circ$ (Mescheryakov et al., 2011). Comparing these results with the simulations of Capitanio et al. (2022), it seems that the first two geometries (pseudo-toroidal and wedge) should be excluded from further considerations. It is important to bear in mind, that the simulation were performed using the best-fit parameters obtained from simultaneous observations with NICER and INTEGRAL telescopes, and are not taking into account the errors of these parameters. This might result in some variation of the constraints put on the inclination parameter. This means, that either the source has some spherical symmetry or has a lower inclination that previously measured.

4.2.2 Cyg X-2

Cyg X-2 was observed from April 30, 2022 to May 2, 2022 for a total of 75.5 ks exposure time. Farinelli et al. (2023) reports Polarization Degree in the 2 - 8 keV energy band of $PD = 1.85 \pm 0.29\%$ and the Polarization Angle $PA = 140^\circ \pm 4^\circ$ (which is consistent with both the measurement by the OSO-8 observatory Novick et al. (1977) and the observation of the radio jet direction). The study reports a slight increase of PD with energy.

The source spectrum is composed of a low-energy component (emitted by the accretion disk) and a Comptonized one, radiated by thermal plasma of temperature $kT_e \sim 3$ keV and polarization of $PD > 2\%$ and PA aligned with the radio jet (presumed to be perpendicular to the accretion disk), while the IXPE observations did not provide a good constraint on the accretion disk contribution. Within the first order approximation, we can assume, that the SL is perpendicular to the plane of accretion disk, which means the PA would be rotated by 90° with respect to that of polarized emission originating in the disk atmosphere with a dominant electron-scattering process. It follows from this observation, that there is a strong preference of the source of polarization to be the spreading layer and the surface of the neutron star, but excluding the accretion disk. However, the source of reflection could also be Comptonized emission from the spreading layer reflecting from the inner radius of the accretion disk. Nevertheless, it is worth mentioning, that the case of initial radiation emerging from the bottom of a scattering medium with $\tau \gg 1$ would be in agreement with the classical Chandrasekhar's results. Polarization might even be perpendicular to the disk plane, with higher PD for the case of disk optical depth of $\tau \lesssim 2$ with a semi-infinite atmosphere

An iron line was present in the Cyg X-2 spectrum (following from the spectroscopic study carried out using simultaneous observations with NICER and *INTEGRAL* satellites). This indirectly points towards the presence of a reflection component, which was, unfortunately, not possible to be studied in greater detail due to the data statistics. Further observations will be required.

The PA value might be explained by the photon reflection radiated by the surface of SL of the NS on the accretion disk. It follows from numerical simulations of accretion disk emission in the case of black holes in soft state, that self-irradiation of accretion disk with scattering as the polarization inducing process induces a PA rotation of 90° . Photons scatter once or twice on the disk and thus, create reflection spectrum. These photons get highly polarized due to the scattering process and significantly contribute to the net polarization of the source. A SL illuminating the accretion disk can result in a polarization of 6 % if we consider an inclination of the source of 70° for X-ray bursters in between bursts. However, such a model does not take into account the direct contribution from the disk, which would lower the PD.

A recent detection of Scorpius X-1 (Long et al., 2022) in the 4 - 8 keV band using the PolarLight instrument (Feng et al., 2019) shows similar polarimetric features as those of Cyg X-2, mainly the fact that the PA is aligned with the jet of the source, and perpendicular to the accretion disk.

4.2.3 GX 9+9

This source belongs in the group of NS-LMXB systems. The observation of GX 9+9 took place on October 9, 2022 with the exposure of 92.5 ks. The analysis of the data is currently ongoing. However, some preliminary results show that there is a detection of polarization with PD $\sim 2\%$. We do not know the orientation of this object, because there is no radio jet present (unlike in the case of Cyg X-2). Hence, we cannot conclude anything about the Polarization Angle. The preliminary results (Ursini et al., in prep.) suggest that the spectro-polarimetric properties are very similar to those observed in Cyg X-2. In essence, this means that there was a detection of polarization, with an indication of higher polarization at higher energies. In addition, the spectrum of GX 9+9 looks similar to that of Cyg X-2 - there are two main spectral components and reflection.

Chapter 5

Conclusions and future prospects

The new dawn blooms as we free it
 For there is always light
 If only we're brave enough to see it
 If only we're brave enough to be it

Amanda Gorman
 The Hill We Climb

In this thesis, we studied X-ray binary systems containing either a black hole or a neutron star as a compact object. We carried out simulations to assess the capability of X-ray polarimetry to constrain spin and geometry of a X-ray binary system with a black hole in thermal state, and studied coronal properties of accreting, weakly magnetized neutron stars in low-mass X-ray binaries.

In Chapter 2, we studied the bright accreting black hole GRS 1915+105 in thermal state, with main interest in the polarimetric properties of the source. We performed simulated observations of the source with the duration of 500 ks using the IXPE telescope, with the aim to study the robustness of spin constraints based on the properties of radiation polarized due to scattering on the electrons in the accretion disk. In this work, we considered two main cases: direct radiation only, and direct plus returning radiation. In the case of direct radiation only, we were able to successfully recover the spin and inclination of the source for all the studied spin cases ($a = 0, 0.7, 0.9$ and 0.998). When the returning radiation was added, it resulted in the emission getting reflected on the accretion disk and adding additional polarization. For this study, we assumed the inclination and orientation of the source on the sky of the observer as known parameters, since adding returning radiation adds substantial degeneracy to the studied problem. In the case of GRS 1915+105, considering known inclination and orientation is a reasonable assumption, as both have been measured based on the properties of the radio jet of the source. We treated spin and albedo as unknown parameters. It follows from our analysis that also in this case we are able to successfully recover the spin and put some reasonable limits on the albedo.

This analysis was carried out under the simplifying assumption that the albedo of the source is energy-independent. This would only allow us to consider scattering as the polarization-inducing process. In Taverna et al. (2021) it is demonstrated that considering a model of a top layer (or an atmosphere) of the accretion disk and studying its ionization profile would allow for the albedo profile to be calculated. This would result in the possibility of taking absorption as a polarization-inducing effect into account. It is important to remark that apart from the currently operating IXPE satellite, there is another polarimetric mission currently under development - the enhanced X-ray Timing and Polarimetry mission (eXTP). This observatory will carry detectors with effective area 4 - 5 times larger than those of IXPE. Therefore, the results of this study will be applicable to those of eXTP, after taking the effective area into consideration. Lastly, it is important to notice, that GRS 1915+105 is currently unobservable, as it is in an obscured state. However, the results obtained in this study are applicable, with due scaling, to any bright source in thermal state.

We also studied XRB sources with an accreting, weakly magnetized neutron star as the compact object. Assessing the properties of the corona and the contribution of the reflection in the spectra of these sources are of utmost importance, as understanding the properties of such components helps with interpretation of the data obtained from the polarimetric observations. In this thesis, we performed an analysis of archival NuSTAR observations of three sources that were planned to be observed with IXPE: GS 1826-238, GX 9+9 and Cyg X-2. We considered two traditionally used models: the Eastern and Western Models, assuming either a blackbody generated by the disk and the neutron star photons Comptonized on the corona (EM), or the reverse scenario (WM). The Eastern Model seems to be more suitable in fitting the data of all the three sources, than the Western Model. The Western Model provided with a good statistical fit when applied to the data of GS 1826-238 and GX 9+9 (for the latter source we also used a Gaussian line profile component, as we see a reflection Fe line at ~ 6.4 keV). However, in the case of GS 1826-238, the WM resulted in the temperature of the accretion disk higher than that of the neutron star, which is rather unusual, while in the case of GX 9+9, we obtained a temperature of the accretion disk ($kt_{bb} \approx 0.3$ keV), which is somewhat low for this model. More difficult to analyze was the last source we studied, Cyg X-2. We used the traditional Eastern and Western Models, as well as `relxill` and its variations `relxillCp` and `relxillNS`. Apart from the last model (using `relxillNS` to model the NS blackbody that is scattered on the corona), the other models did not provide satisfactory fits. In the latter case, we used an Eastern-like model modified by the additional Gaussian line profile, which provided with the statistically best fit out of the used models. The high χ^2 statistics of the used models might be caused as a combination of the fact that the models are degenerate, and due to the instrumental imprecision. We cannot confidently conclude the specific geometry of each source solely based on spectroscopic observations, which is why polarimetry is a crucial tool in answering this question. Nevertheless, this is still a work in progress.

X-ray polarimetry has certainly opened a new window into studying astrophysical objects. It is important to connect the observational contribution (as we have shown in this thesis), numerical simulations, as well as the theoretical understanding of the astrophysical processes. The results presented in this work provide a contribution to a new path, paved by the possibilities that X-ray polarimetry offers. X-ray polarimetry represents a new method that will help in constraining the black hole spin (as shown in Chapter 2). Additionally, studying polarimetric properties of corona is a great tool in understanding the coronal geometry and its specific properties (Chapter 3). These results are of a high importance in order to understand the results from the IXPE observations accreting black holes and weakly magnetized neutron stars, as mentioned in Chapter 4.

Appendix A

Sometimes seeing life through a different lens opens a new world to possibilities.

Meredith Grey

X-ray astrophysics is a difficult field to study, due to the complications accompanying the construction of such observatories. X-ray radiation is absorbed in the atmosphere of the Earth, which made developments in this field much behind those of optical and radio astronomy. Any X-ray telescopes must be placed at a very high altitude, above $\approx 99\%$ of the atmosphere. Another difficulty arises due to the fact that it is extremely challenging to focus X-ray photons. They are usually absorbed by the materials composing the mirrors in the IR, optical and UV telescopes.

A mirror reflecting X-ray photons is used in a Wolter type telescopes. Such a mirror can be built, however, solely if the angle from the plane of reflection is very low ($\sim 10'$ up to 2°). The first telescope using this technology was the rocket-borne experiment used to obtain the X-ray images of the Sun, launched in 1965 (Giacconi et al., 1965). Ever since this historic event, several technological breakthroughs have followed in the X-ray astronomy, as well as the persistent striving to improve on those technologies and build better satellites, several orders of magnitude more sensitive than the previous ones. Each X-ray satellite consists of the light gathering aperture and detectors. It was only a few years after the first X-ray telescope was built, that collimators were added to the payload, and then focusing X-ray optics were developed. The first satellite to use this technology was the Einstein Observatory (HEAO 2; Giacconi et al. (1979)). Thanks to these advancements, focusing optics are now commonly used in telescopes operating in the X-ray energy band.

In this work, we focused on simulation and analysis of data from two currently operating X-ray observatories: IXPE and *NuSTAR*. In the following, we will briefly discuss their main properties.

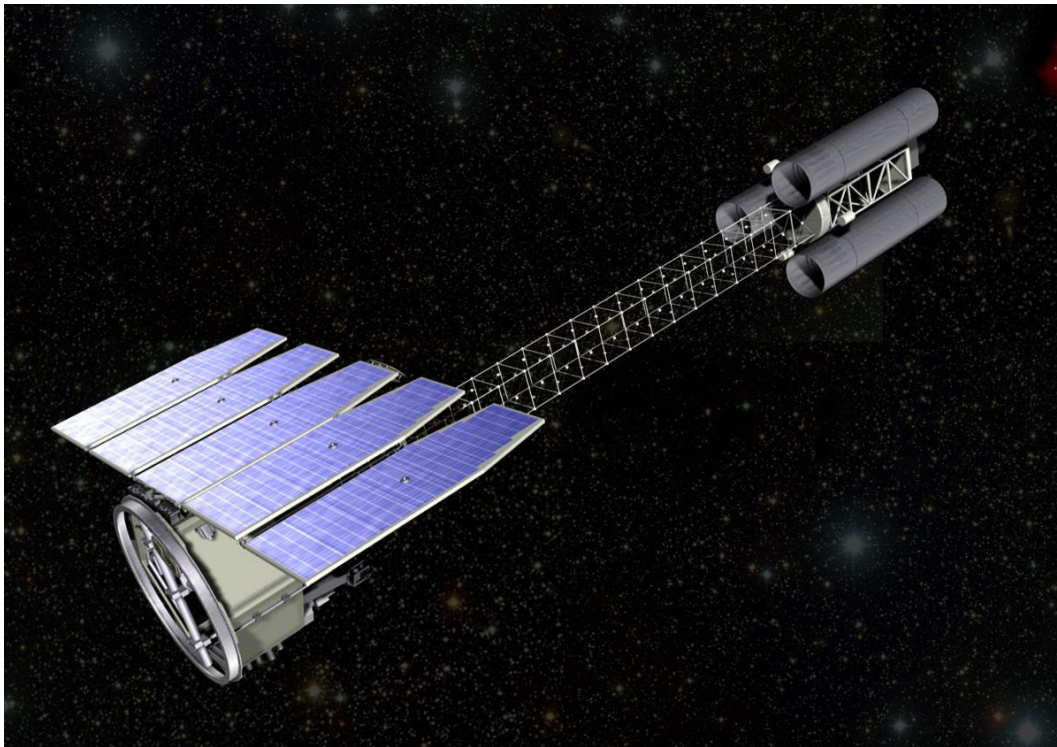


Figure 5.2. Imaging X-ray polarimetry Explorer. Figure credit: Weisskopf et al. (2008).

IXPE: Imaging X-ray Polarimetry Explorer

The Imaging X-ray polarimetry Explorer (IXPE, see Figure 5.4) is a NASA Small Explorer (SMEX) mission selected in January 2017, as a collaboration with the Italian Space Agency (ASI). The telescope has a 2-year baseline program. IXPE (Weisskopf et al., 2022) is set to carry out observations of multiple sources during the mission's first year, with more detailed follow-up observations during the second year of operation. IXPE was launched on December 9, 2021 from the Kennedy Space Center on board the Falcon-9 rocket. The IXPE telescope is 5.2 m long and 1.1 m in diameter, weighs 330 kg and is placed at the equatorial orbit at the inclination 0° and altitude of 600 km.

The sources of interest are observed over a duration of multiple orbits, until the telescope completes the observation. Polarimetry requires a large number of photons, and, therefore, long observing times are usually required, ranging from a few hours to several days. It is possible to observe the targets of observation usually during a 50 day window, twice a year, while each source can be observed continuously for a minimum of 57 minutes.

IXPE is equipped with 3 identical telescopes. Each of the telescopes contains a Mirror Module Assembly (MMA), with a detector unit (DUs) at its focus. The

DUs are sensitive to the X-ray photons in the 2 - 8 keV energy band with a combined effective area of $\sim 600 \text{ cm}^2$.

Mirror Module Assembly

During the construction of the satellite, four Mirror Module Assemblies (MMAs) were built, three of them for flight, the remaining is spare. Each MMA consists of 24 centrally nested mirror shells. The shells are made of an electromorped nickel and cobalt composite, which provides a higher strength than pure nickel. The shells are separated by only about 2 mm, which is done in order to maximize the effective area. The length of each individual shell is 600 mm. The inside part of the shells does not have any additional coating, as the nickel/cobalt provides optimal reflectivity for the 2 - 8 keV band. The MMA has a thermal shield at each end, providing thermal control, ensuring against heat loss, all while they allow X-ray photons to pass through. The shields are made of an ultra thin ($1.4 \mu\text{m}$) polyimide film with a 50 nm aluminum coat. The full detector area is $15 \times 15 \text{ mm}$, and the telescope field of view (FOV) is $12.9' \times 12.9'$.

The Detector Units

The detector units (DUs) represent the most important part of the IXPE observatory. Each DU is placed at the focus of the MMAs, which is important to ensure position determination, energy determination, timing information and polarization sensitivity. Each DU operates with a Gas Pixel Detector (GPD). An incident X-ray enters the detector via a beryllium window, then interacts with the Di-methyl ether fill gas. This produces a photoelectron, which traces a trail of ionization in the gas. The track drifts through Gas Electron Multipliers in order to increase the charge of the photoelectron, which then reaches a pixel anode read-out. The GPD images the tracks of the photoelectron. The original direction in which the photoelectron is emitted is preferentially aligned along the electric vector of the absorbed photon. The original point of interaction in the detector provides information on the position on the sky of the sources, while the total charge in the track gives us information on the energy of the absorbed X-ray photon.

***NuSTAR*: The Nuclear Spectroscopic Telescope Array**

The Nuclear Spectroscopic Telescope Array (*NuSTAR*; see Figure 5.6) is a NASA SMEX mission, launched on June 13, 2012 from the Reagan Test Site located on the Kwajalein Atoll in the South Pacific on board the Pegasus XL vehicle. The telescope focuses on the hard X-ray emission, operating within the 3 - 80 keV energy range. The importance of this observatory lays especially in its angular resolution

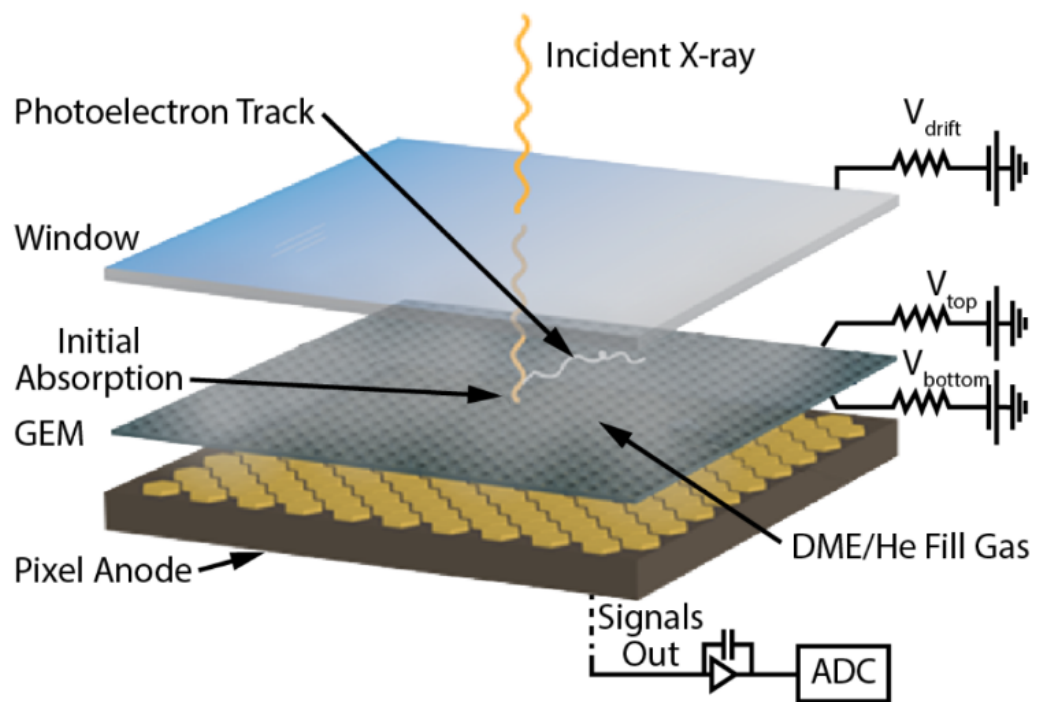


Figure 5.4. The composition of a Gas Pixel Detector (GPD). Figure credit: Weisskopf et al. (2016).

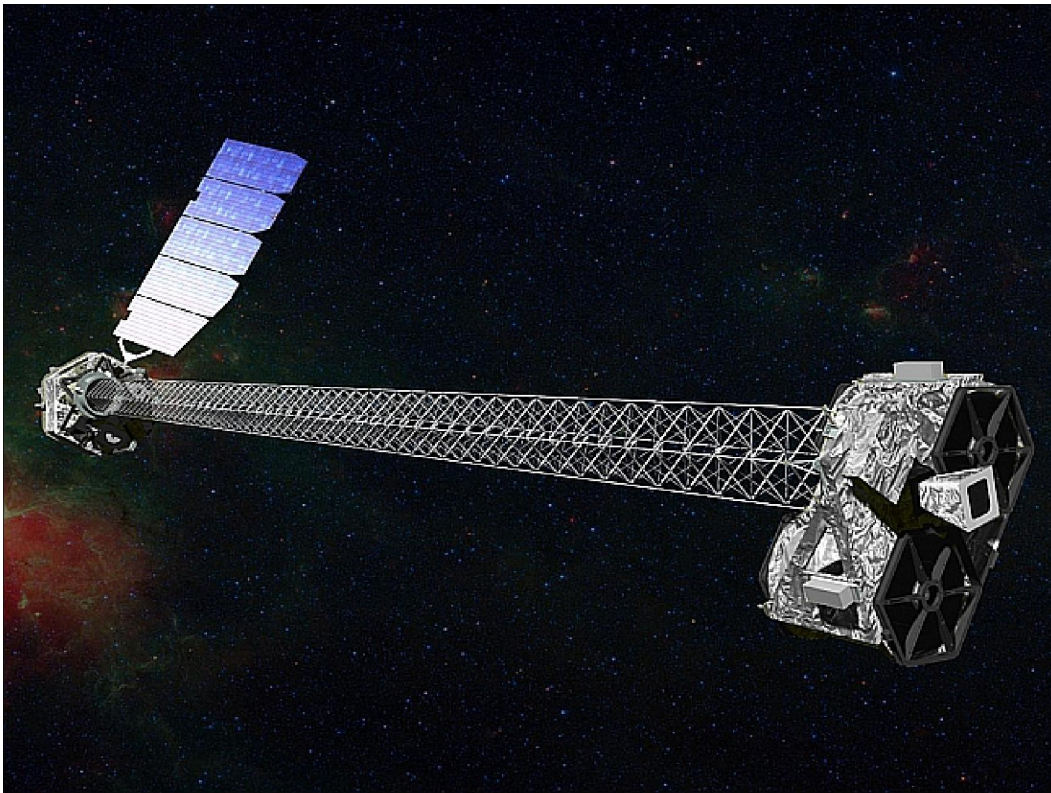


Figure 5.6. The Nuclear Spectroscopic Telescope Array. Figure credit: NASA/GPL.

and sensitivity, which is higher than any current hard X-ray observatory working within the same energy band (Harrison et al., 2013) by an order of magnitude and two orders of magnitude, respectively.

The *NuSTAR* telescope is composed of two co-aligned telescopes sensitive to hard X-ray photons. There are three main parts composing the telescope:

- the optics (or mirrors), focusing the radiation
- the detectors, recording the image
- expendable mast, holding the optics and the detectors at the 10 m separation distance on the orbit

Optics

NuSTAR uses two optics units allowing the telescope to look at the same location on the sky. After an observation, the two images are joined together on the ground, which allows observation of fainter objects. The telescope uses Wolter-type low-grazing angle focusing optics. Each of the two modules is composed of 133 shells, that are placed concentrically and con-focally. Their focal length is 10.15 m. The angular resolution of the two modules is $\sim 12''$ (at FWHM), with the FOV $\sim 10'$. Since this is an X-ray optics, the reflective ability of the shells decreases with increasing angle of incident photons. This consequence is more noticeable on higher energies, where the FOV decreases to $6'$ at the 60 keV energy.

Detectors

The satellite carries on board high-energy X-ray detectors suited to detect the position and energy of incoming X-ray photons, which work to record an image focused by the optics. The detectors are placed in the focal point of the light from the telescope. For this reason, they are also called the focal-plane detectors. Each detector is equipped with a Focal Plane Module (FPM). The FPM is comprised of four detectors made of Cadmium Zinc Telluride (CdZnTe), with 32×32 pixels. They are surrounded by an anti-coincidence shield made of Cesium Iodide (CsI). The resolution of these detectors is $\sim 1\%$. Moreover, they also have a high quantum efficiency over the entire energy range of *NuSTAR*.

Mast

The mast is 10 m in length and its function is to bridge the detectors and mirrors. Hard X-ray photons graze off the mirror planes at almost parallel angles. Due to this fact, a telescope operating in the hard X-ray energy band needs a long focal length (= focal plane; the distance between the optics and detectors). The mast is compact,

of light weight and ensures a stable connecting structure between the two aligned branches.

List of Figures

- 1.2 The disk-corona model for an accreting X-ray binary system containing a black hole as a compact object. The XRB contains an optically thick accretion disk described by a multi-color blackbody spectrum (red arrows). The direct contribution from the disk is thermal. However, some of the thermal photons scatter on the electrons in the corona, where they get Compton scattered and produce a power-law (represented by blue arrows), which irradiates the accretion disk and results in the reflection component (green arrows). Figure credit: Nampalliwar and Bambi (2020). 4
- 1.4 Illustration of corona geometry models: lamppost model (a), sandwich model (b), spherical model (c) and toroidal model (d). Figure credit: Nampalliwar and Bambi (2020). 5
- 1.5 The Fe emission line profile. The line profile depends on the contribution from the Doppler and transverse-Doppler effects, relativistic beaming and gravitational redshift. The left panel shows an accretion disk with its right hand side rotating towards the observer and the left hand side away from the observer. Two annuli are marked on the disk. The right panel shows the Fe line profile of these two annuli for a non-relativistic accretion disk (upper subpanel), the transverse Doppler and relativistic beaming considered (second subpanel from top), and redshift (third subpanel). All these effects summed together in the bottom subpanel. Image credit: Fabian et al. (2000). 7
- 1.7 An energy spectrum of the NS-LMXB source GX 3+1, analyzed by S.Piraino et al. (2012). Between 6 - 7 keV we see a pronounced iron line. 7
- 1.9 Disk-corona model of an accreting black hole in an X-ray binary source. Shown are spectral components: thermal component radiated by the accretion disk (red), power law component originated by the corona (blue) and the reflection component due to the irradiation of the accretion disk by the power law from the corona (green). Image credit: Nampalliwar and Bambi (2020). 8

1.11	Portrayal of the typical q-shaped track that X-ray binary systems with a black hole trace throughout their evolution through various spectral states in the hardness-intensity diagram (HID). Figure credit: Kylafis et al. (2012).	11
1.13	Spectral shapes of an X-ray binary system containing a black hole Cyg X-1 in the low/hard state (red) and the high/soft state (black). Figure credit: Yamada et al. (2013).	12
1.15	Representation of the color-color diagram (CCD) for neutron star low-mass X-ray binary systems. The sources are either Atoll or Z-sources based on the shape of the track they trace in the diagram. Atoll sources are either found in an island state (IS), lower banana (LB) or upper banana (UB). Z-sources trace horizontal branch (HB), normal branch (NB) or the flaring branch (FB). Figure credit: van Straaten et al. (2003) and Jonker et al. (2000).	15
1.17	A representation of a slab coronal geometry considered in the Western-like model, where the disk photons get scattered on the corona surrounding the disk, while the neutron star is observed directly as a blackbody. Image credit: A. Gnarini	16
1.18	Representation of a wedge (a) and spherical (b) coronal geometry in the Eastern-like scenario, with a thermal component from the accretion disk (observed directly) and the seed photons from the neutron star scattered in the corona. Image credit: A. Gnarini.	17
1.23	Polarization ellipse	21
1.20	Energy dependence of the spectra (top), Polarization Degree (middle) and Polarization Angle (bottom) radiated by a spherical corona. Different coronal height results in different polarization characteristics. Image credit Zhang et al. (2022).	25
1.22	Energy dependence of Polarization Degree (top) and Polarization Angle (bottom) for an accreting neutron star low-mass X-ray binary system in the high/soft state. Represented are different polarization properties for the shell coronal geometry (red) and for slab (blue). Image credit: Gnarini et al. (2022).	26
2.2	A representation of a connection between a black hole spin and the distance if the inner radius of the accretion disk. For non-rotating (or low-spin) black holes, the inner radius is at a greater distance from the black hole (left) than in the case of a maximally rotating black hole (on the right). Image credit https://www.cfa.harvard.edu/imagelist/2006-30	28
2.4	A visual representation of an x-ray binary system as observed by IXPE with marked angles for inclination Θ , orientation of the system χ and its distance d towards the observer. Figure credit: Anastasia Yilmaz.	33

- 2.5 Polarization degree (left) and polarization angle (right) dependence on energy for different inclination cases for GRS1915+105 with BH mass $M = 14 M_{\odot}$ and spin $a = 0$ (orange, green and violet lines) and $a = 0.998$ (red, yellow and blue lines). The accretion rate is considered in such a way, that it would correspond to the observed luminosity $L = 0.45 L_{\text{Edd}}$. The plots were created using the KYNBBRR model. 33
- 2.6 Same as in Figure 2.5, but with the accretion rate corresponding to the luminosity $L = 0.185 L_{\text{Edd}}$. The plots were created using the KYNBBRR model. 34
- 2.7 Upper panel: representation of a black hole accretion disk on the sky of the observer. Bottom: flux and the polarization direction of collected radiation. The effects of variation of the polarization angle due to strong gravity are shown going from left to right. The figures represent a maximally rotating black hole. Starting from a region distant from the black hole, at $r = 30r_g$, (a), emission peaks at lower temperatures (≈ 1 keV) and the polarization is horizontal. Then, going very close to the black hole, at $r = 1.285r_g$, (b), the energy flux peaks at a higher energy (≈ 5 keV) and the polarization (blue line on the bottom right subpanel) is close to vertical. The length of the blue line represents the polarization degree, which gets lower closer to the source. 35
- 2.8 Same as in Figure 2.5, but with the accretion rate corresponding to the luminosity $L = 0.446 L_{\text{Edd}}$. The plots were created using the KYNBB model. 36
- 2.9 Same as in Figure 2.5, but with the accretion rate corresponding to the luminosity $L = 0.204 L_{\text{Edd}}$. The plots were created using the KYNBB model. 37
- 2.10 Contour plots of spin vs inclination resulting from the fit the simulated Stokes parameters Q and U obtained for $a = 0, 0.7, 0.9, 0.998$ for various exposure times: (a) $t = 500$ ks, (b) $t = 250$ ks and (c) $t = 125$ ks. Confidence contours at 1σ (red), 2σ (green) and 3σ (blue) are also shown. The gray cross marks the original values, which were (left to right, for each panel) spin $a = 0, 0.7, 0.9$ and 0.998 and $i = 70^\circ$ for all the plotted cases. The black "plus" sign shows the best fit value, which is (again, left to right) $a = 0, 0.7, 0.91$ and 0.998 (a), $a = 0, 0.82, 0.992$ and 0.999 (b) and $a = 0.4, 0.7, 0.86$ and 0.993 (c). Data are plotted for a model without returning radiation (KYNBB). 40
- 2.11 Spin (a) and inclination (b) constraints with the KYNBB model versus input values. Green dashed line represents the 1:1 relation for reconstructed and input spins (a) and the input value for the inclination (b). 41

2.12	Energy dependence of Stokes Q/E (a) and U/E (b) data simulated for spin 0.998 and for each of the three IXPE detector units fitted with the theoretical model. Response matrix was applied on the models. The data were simulated using a model with returning radiation (KYNBBRR).	42
2.13	Contour plots of spin vs albedo for spin values $a = 0$ (a), 0.7 (b), 0.9 (c) and 0.998 (d) using simulated Stokes Q/E and U/E dependence on energy data. Plot in (d) is composed of two different grids divided by the black rectangular area, with the interval in spin 0.90–0.98 having a step of 0.01 and the interval 0.98–1.00 with the step of 0.002. In red 1σ , green 2σ and blue 3σ contours. Similarly to the previous case, the grey cross sign marks the original value, which was 50 % albedo in all the shown cases and spin $a = 0$ (a), $a = 0.7$ (b), $a = 0.9$ (c) and $a = 0.998$ (d). The black "plus" sign marks the best-fit value, which is as follows: $a = 0$, albedo = 38 % (a), $a = 0.65$, albedo = 73 % (b), $a = 0.93$, albedo = 43 % (c), $a = 0.998$, albedo = 50 % (d). Plots are calculated using a model with returning radiation (KYNBBRR).	43
3.1	Best fit of the GS 1826-238 source observation using Eastern (a) and Western (b) models (upper panels of both plots) and their data residuals in the sigma units (in the bottom part).	52
3.2	Best fit of the GX 9+9 source observation using Eastern (a) and Western (b) models (upper panels of both plots) and their data residuals in the sigma units (in the bottom part). We notice an iron line in the data residuals in the 6 - 7 keV band.	53
3.3	Best fit of the GX 9+9 source observation using Eastern (a) and Western (b) models (upper panels of both plots) and their data residuals in the sigma units (in the bottom part). An additional component fitting the iron line was used.	55
3.4	Incident model spectrum used to fit the data from an observation of GX 9+9 with the additional model component accounting for the iron line profile. Disk emission or the neutron star blackbody (pink), Comptonization (brown), Gaussian line (green) and the total spectrum (blue).	56
3.6	Cyg X-2 fit (upper panel) and its data residuals (bottom) using a model without relativistic reflection. We observe strong residuals around the energy of $\approx 5.5 - 7.5$ keV.	58
3.7	Best fit of the Cyg X-2 source observation using Eastern (a) and Western (b) models (upper panels of both plots) and their data residuals in the sigma units (in the bottom part). The fit was performed using the relativistic reflection model <code>relxill</code>	60

3.8	Best fit of the Cyg X-2 source observation using Eastern (a) and Western (b) models (upper panels of both plots) and their data residuals (in the bottom part). The fit was performed using the relativistic reflection model <code>relxillCp</code>	61
3.9	Best fit of the Cyg X-2 source observation in the upper panel and data residuals in the sigma units in the bottom panel for int1 in (a) and int2 in (b). The fit was performed using the relativistic reflection model <code>relxillNS</code>	63
3.10	Incident model spectrum used to fit the int1 (a) without the Gaussian line profile and int2 (b) including the gaussian line profile in order to fit the relativistic Fe line. The fit was performed using the relativistic reflection model <code>relxillNS</code> . Disk emission (pink), Comptonization (orange/dark blue), <code>relxillNS</code> (green), Gaussian line (red) and the total spectrum (black/blue).	64
3.11	Best fit of the Cyg X-2 source observation in the upper panel and data residuals in the sigma units in the bottom panel for int1 in (a) and int2 in (b). The fit was performed using the relativistic reflection model <code>relxillNS</code> with the blackbody temperatures tied together.	65
3.13	Fit of the GS 1826-238 source observation using the Western model after switching the accretion disk and NS temperatures. We notice very apparent residuals (middle sub-panel) from the model on energies $\lesssim 10$ keV. In this scenario we do not obtain an acceptable fit, which is also apparent from the residuals in sigma units (bottom sub-panel).	69
5.2	Imaging X-ray polarimetry Explorer. Figure credit: Weisskopf et al. (2008).	82
5.4	The composition of a Gas Pixel Detector (GPD). Figure credit: Weisskopf et al. (2016).	84
5.6	The Nuclear Spectroscopic Telescope Array. Figure credit: NASA/GPL.	85

List of Tables

2.1	Model parameters of <code>KYNBB</code>	31
2.2	Best-fit values for the spin (a), inclination (i) and orientation of the source on the sky of the observer (χ) for simulated exposure times 500 ks, 250 ks and 125 ks, modeled and fitted with <code>KYNBB</code> . (u) - errors that were unconstrained during the fitting procedure.	38
3.1	Log of the observations of the studied sources	49
3.2	Best-fit values of the accretion disk, corona and neutron star temperatures and the photon index of the GS 1826-238 spectra using the Eastern (EM) and Western Models (WM). Column density nH of the <code>TBabs</code> model component has the value of $0.2 \times 10^{22} atoms/cm^2$. 51	51
3.3	Best-fit values of the accretion disk, corona and neutron star temperatures and the photon index of the GX 9+9 spectra using the Eastern (EM) and Western Models (WM). Column density nH of the <code>TBabs</code> model component has the value of $0.2 \times 10^{22} atoms/cm^2$. 57	57
3.4	Best-fit values of the accretion disk, corona and neutron star temperatures, inner radius of the accretion disk and its ionization, and the photon index of the Cyg X-2 spectra using the Eastern (EM) and Western Models (WM). The fit was performed using the relativistic reflection model <code>relxill</code> . Column density nH of the <code>TBabs</code> model component has the value of $0.2 \times 10^{22} atoms/cm^2$. u - error is unconstrained.	66
3.5	Best-fit values of the accretion disk, corona and neutron star temperatures, inclination of the source, inner radius of the accretion disk and its ionization, and the photon index of the Cyg X-2 spectra using the Eastern (EM) and Western Models (WM). The fit was performed using the relativistic reflection model <code>relxillCp</code> . Column density nH of the <code>TBabs</code> model component has the value of $0.2 \times 10^{22} atoms/cm^2$. f - parameter was frozen for the fit. u - error is unconstrained.	67

-
- 3.6 Best-fit values of the accretion disk, corona and neutron star temperatures, inner radius of the accretion disk and its ionization, Fe line energy, and the photon index of the Cyg X-2 spectra. The fit was performed using the relativistic reflection model `relxillNS`. Column density `nH` of the `TBabs` model component has the value of $0.2 \times 10^{22} \text{ atoms/cm}^2$. u - error is unconstrained, t - parameter is tied to the kT_{bb} parameter of the `nthComp` model. 68

Bibliography

- Vivek K. Agrawal, Anuj Nandi, and Tilak Katoch. AstroSat view of ‘clocked’ burster GS 1826-238: broad-band spectral nature of persistent and burst emission during soft state. *Monthly Notices of the Royal Astronomical Society*, 518(1):194–205, sep 2022. doi: 10.1093/mnras/stac2579. URL <https://doi.org/10.1093>.
- R. D. Blandford and D. G. Payne. Hydromagnetic flows from accretion disks and the production of radio jets. *MNRAS*, 199:883–903, June 1982. doi: 10.1093/mnras/199.4.883.
- R. D. Blandford and R. L. Znajek. Electromagnetic extraction of energy from Kerr black holes. *MNRAS*, 179:433–456, May 1977. doi: 10.1093/mnras/179.3.433.
- Jennifer L. Blum and J. M. Miller. The Relativistic Iron Line And Black Hole Spin Of GRS 1915+105. In *American Astronomical Society Meeting Abstracts #213*, volume 213 of *American Astronomical Society Meeting Abstracts*, page 328.03, January 2009.
- Michal Bursa. Numerical implementation of equations for photon motion in Kerr spacetime. In *RAGtime 17-19: Workshops on Black Holes and Neutron Stars*, pages 7–21, December 2017.
- Fiamma Capitanio, Sergio Fabiani, Andrea Gnarini, Francesco Ursini, Carlo Ferrigno, Giorgio Matt, Juri Poutanen, Massimo Cocchi, Romana Mikusincova, Ruben Farinelli, Stefano Bianchi, Jari J. E. Kajava, Fabio Muleri, Celia Sanchez-Fernandez, Paolo Soffitta, Kinwah Wu, Ivan Agudo, Lucio A. Antonelli, Matteo Bachetti, Luca Baldini, Wayne H. Baumgartner, Ronaldo Bellazzini, Stephen D. Bongiorno, Raffaella Bonino, Alessandro Brez, Niccoló Bucciantini, Simone Castellano, Elisabetta Cavazzuti, Stefano Ciprini, Enrico Costa, Alessandra De Rosa, Ettore Del Monte, Laura Di Gesu, Niccolò Di Lalla, Alessandro Di Marco, Immacolata Donnarumma, Victor Doroshenko, Michal Dovciak, Steven R. Ehlert, Teruaki Enoto, Yuri Evangelista, Riccardo Ferrazzoli, Javier A. Garcia, Shuichi Gunji, Kiyoshi Hayashida, Jeremy Heyl, Wataru Iwakiri, Svetlana G. Jorstad, Vladimir Karas, Takao Kitaguchi, Jeffery J. Kolodziejczak, Henric Krawczynski, Fabio La Monaca, Luca Latronico, Ioannis Liodakis, Simone Maldera, Alberto Manfreda, Frédéric Marin, Andrea Marinucci, Alan P. Marscher, Herman L. Marshall, Ikuyuki Mitsuishi, Tsunefumi Mizuno, C. Y. Ng, Stephen L. O’Dell,

- Nicola Omodei, Chiara Oppedisano, Alessandro Papitto, George G. Pavlov, Abel L. Peirson, Matteo Perri, Melissa Pesce -Rollins, Pierre-Olivier Petrucci, Maura Pilia, Andrea Possenti, Simonetta Puccetti, Brian D. Ramsey, John Rankin, Ajay Ratheesh, Roger W. Romani, Carmelo Sgrò, Patrick Slane, Gloria Spandre, Toru Tamagawa, Fabrizio Tavecchio, Roberto Taverna, Yuzuru Tawara, Allyn F. Tennant, Nicholas E. Thomas, Francesco Tombesi, Alessio Trois, Sergey S. Tsygankov, Roberto Turolla, Jacco Vink, Martin C. Weisskopf, Fei Xie, and Silvia Zane. Polarization properties of the weakly magnetized neutron star X-ray binary GS 1826-238 in the high soft state. *arXiv e-prints*, art. arXiv:2212.12472, December 2022. doi: 10.48550/arXiv.2212.12472.
- J. Casares, J. I. González Hernández, G. Israelian, and R. Rebolo. On the mass of the neutron star in Cyg X-2. *Monthly Notices of the Royal Astronomical Society*, 401(4): 2517–2520, 01 2010. ISSN 0035-8711. doi: 10.1111/j.1365-2966.2009.15828.x. URL <https://doi.org/10.1111/j.1365-2966.2009.15828.x>.
- Subrahmanyan Chandrasekhar. *Radiative transfer*. 1960.
- M. Chauvin, H. G. Florén, M. Friis, M. Jackson, T. Kamae, J. Kataoka, T. Kawano, M. Kiss, V. Mikhalev, T. Mizuno, N. Ohashi, T. Stana, H. Tajima, H. Takahashi, N. Uchida, and M. Pearce. Accretion geometry of the black-hole binary Cygnus X-1 from X-ray polarimetry. *Nature Astronomy*, 2:652–655, June 2018. doi: 10.1038/s41550-018-0489-x.
- J. Chenevez, D. K. Galloway, J. J. M. in 't Zand, J. A. Tomsick, D. Barret, D. Chakrabarty, F. Fürst, S. E. Boggs, F. E. Christensen, W. W. Craig, C. J. Hailey, F. A. Harrison, P. Romano, D. Stern, and W. W. Zhang. A soft x-ray spectral episode for the clocked burster, gs 1826–24 as measured by swift and nustar. *The Astrophysical Journal*, 818(2):135, feb 2016. doi: 10.3847/0004-637X/818/2/135. URL <https://dx.doi.org/10.3847/0004-637X/818/2/135>.
- M. Cocchi, A. Bazzano, L. Natalucci, P. Ubertini, J. Heise, J. J. M. in't Zand, J. M. Muller, and M. J. S. Smith. Clocked bursts from GS 1826-238. In Mark L. McConnell and James M. Ryan, editors, *The Fifth Compton Symposium*, volume 510 of *American Inst. Phys. Conf. Ser.*, pages 203–207, April 2000. doi: 10.1063/1.1303203.
- M. Cocchi, R. Farinelli, and A. Paizis. BeppoSAX view of the NS-LMXB GS 1826-238. *A&A*, 529:A155, May 2011. doi: 10.1051/0004-6361/201016241.
- P. A. Connors and R. F. Stark. Observable gravitational effects on polarised radiation coming from near a black hole. *Nature*, 269(5624):128–129, September 1977. doi: 10.1038/269128a0.
- P. A. Connors, T. Piran, and R. F. Stark. Polarization features of X-ray radiation emitted near black holes. *ApJ*, 235:224–244, January 1980. doi: 10.1086/157627.

- A. P. Cowley, D. Crampton, and J. B. Hutchings. The halo population X-ray source Cygnus X-2. *ApJ*, 231:539–550, July 1979. doi: 10.1086/157216.
- S. W. Davis, O. M. Blaes, I. Hubeny, and N. J. Turner. Relativistic Accretion Disk Models of High-State Black Hole X-Ray Binary Spectra. *ApJ*, 621:372–387, March 2005. doi: 10.1086/427278. URL <http://adsabs.harvard.edu/abs/2005ApJ...621..372D>.
- T. Di Salvo and L. Stella. High energy radiation from neutron star binaries, 2002. URL <https://arxiv.org/abs/astro-ph/0207219>.
- T. Di Salvo, R. Farinelli, L. Burderi, F. Frontera, E. Kuulkers, N. Masetti, N. R. Robba, L. Stella, and M. van der Klis. On the spectral evolution of Cygnus X-2 along its color-color diagram. *A&A*, 386:535–547, May 2002. doi: 10.1051/0004-6361:20020238.
- M. Díaz Trigo and L. Boirin. Accretion disc atmospheres and winds in low-mass X-ray binaries. *Astronomische Nachrichten*, 337(4-5):368, May 2016. doi: 10.1002/asna.201612315.
- Chris Done, Marek Gierliński, and Aya Kubota. Modelling the behaviour of accretion flows in X-ray binaries. Everything you always wanted to know about accretion but were afraid to ask. *A&ARv*, 15(1):1–66, December 2007. doi: 10.1007/s00159-007-0006-1.
- Michal Dovciak. *Radiation of Accretion Discs in Strong Gravity*. PhD thesis, -, November 2004.
- M. Dovčiak, V. Karas, and T. Yaqoob. An Extended Scheme for Fitting X-Ray Data with Accretion Disk Spectra in the Strong Gravity Regime. *ApJS*, 153:205–221, July 2004. doi: 10.1086/421115. URL <http://adsabs.harvard.edu/abs/2004ApJS...153..205D>.
- M. Dovčiak, F. Muleri, R. W. Goosmann, V. Karas, and G. Matt. Thermal disc emission from a rotating black hole: X-ray polarization signatures. *MNRAS*, 391(1):32–38, November 2008. doi: 10.1111/j.1365-2966.2008.13872.x.
- A. C. Fabian and R. R. Ross. X-ray Reflection. *Space Sci. Rev.*, 157(1-4):167–176, December 2010. doi: 10.1007/s11214-010-9699-y.
- A. C. Fabian, M. J. Rees, L. Stella, and N. E. White. X-ray fluorescence from the inner disc in Cygnus X-1. *MNRAS*, 238:729–736, May 1989. doi: 10.1093/mnras/238.3.729.
- A. C. Fabian, K. Iwasawa, C. S. Reynolds, and A. J. Young. Broad Iron Lines in Active Galactic Nuclei. *PASP*, 112(775):1145–1161, September 2000. doi: 10.1086/316610.

- R. Farinelli, S. Fabiani, J. Poutanen, F. Ursini, C. Ferrigno, S. Bianchi, M. Cocchi, F. Capitanio, A. De Rosa, A. Gnarini, F. Kislat, G. Matt, R. Mikusincova, F. Muleri, I. Agudo, L. A. Antonelli, M. Bachetti, L. Baldini, W. H. Baumgartner, R. Bellazzini, S. D. Bongiorno, R. Bonino, A. Brez, N. Bucciantini, S. Castellano, E. Cavazzuti, S. Ciprini, E. Costa, E. Del Monte, L. Di Gesu, N. Di Lalla, A. Di Marco, I. Donnarumma, V. Doroshenko, M. Dovčiak, S. R. Ehlert, T. Enoto, Y. Evangelista, R. Ferrazzoli, J. A. Garcia, S. Gunji, K. Hayashida, J. Heyl, W. Iwakiri, S. G. Jorstad, V. Karas, T. Kitaguchi, J. J. Kolodziejczak, H. Krawczynski, F. La Monaca, L. Latronico, I. Liodakis, S. Maldera, A. Manfreda, F. Marin, A. P. Marscher, H. L. Marshall, I. Mitsuishi, T. Mizuno, C. Y. Ng, S. L. O'Dell, N. Omodei, C. Oppedisano, A. Papitto, G. G. Pavlov, A. L. Peirson, M. Perri, M. Pesce-Rollins, P. O. Petrucci, M. Pilia, A. Possenti, S. Puccetti, B. D. Ramsey, J. Rankin, A. Ratheesh, R. W. Romani, C. Sgrò, P. Slane, P. Soffitta, G. Spandre, T. Tamagawa, F. Tavecchio, R. Taverna, Y. Tawara, A. F. Tennant, N. E. Thomas, F. Tombesi, A. Trois, S. S. Tsygankov, R. Turolla, J. Vink, M. C. Weisskopf, K. Wu, F. Xie, and S. Zane. Accretion geometry of the neutron star low mass X-ray binary Cyg X-2 from X-ray polarization measurements. *MNRAS*, 519(3): 3681–3690, March 2023. doi: 10.1093/mnras/stac3726.
- R. P. Fender and E. Kuulkers. On the peak radio and X-ray emission from neutron star and black hole candidate X-ray transients. *MNRAS*, 324(4):923–930, July 2001. doi: 10.1046/j.1365-8711.2001.04345.x.
- R. P. Fender, T. M. Belloni, and E. Gallo. Towards a unified model for black hole X-ray binary jets. *MNRAS*, 355(4):1105–1118, December 2004. doi: 10.1111/j.1365-2966.2004.08384.x.
- Rob Fender. Jets from X-ray binaries. In *Compact stellar X-ray sources*, volume 39, pages 381–419. 2006.
- Hua Feng, Weichun Jiang, Massimo Minuti, Qiong Wu, Aera Jung, Dongxin Yang, Saverio Citraro, Hikmat Nasimi, Jiandong Yu, Ge Jin, Jiahui Huang, Ming Zeng, Peng An, Luca Baldini, Ronaldo Bellazzini, Alessandro Brez, Luca Latronico, Carmelo Sgrò, Gloria Spandre, Michele Pinchera, Fabio Muleri, Paolo Soffitta, and Enrico Costa. PolarLight: a CubeSat X-ray polarimeter based on the gas pixel detector. *Experimental Astronomy*, 47(1-2):225–243, April 2019. doi: 10.1007/s10686-019-09625-z.
- G. J. Ferland, M. Chatzikos, F. Guzmán, M. L. Lykins, P. A. M. van Hoof, R. J. R. Williams, N. P. Abel, N. R. Badnell, F. P. Keenan, R. L. Porter, and P. C. Stancil. The 2017 Release Cloudy. *Rev. Mex. Astron. Astrofis.*, 53:385–438, October 2017.
- Juhan Frank, Andrew King, and Derek J. Raine. *Accretion Power in Astrophysics: Third Edition*. 2002.

- Duncan K. Galloway, Andrew Cumming, Erik Kuulkers, Lars Bildsten, Deepto Chakrabarty, and Richard E. Rothschild. Periodic thermonuclear x-ray bursts from gs 1826–24 and the fuel composition as a function of accretion rate. *The Astrophysical Journal*, 601(1):466, jan 2004. doi: 10.1086/380445. URL <https://dx.doi.org/10.1086/380445>.
- J. García and T. R. Kallman. X-ray Reflected Spectra from Accretion Disk Models. I. Constant Density Atmospheres. *ApJ*, 718(2):695–706, August 2010. doi: 10.1088/0004-637X/718/2/695.
- J. García, T. R. Kallman, and R. F. Mushotzky. X-ray Reflected Spectra from Accretion Disk Models. II. Diagnostic Tools for X-ray Observations. *ApJ*, 731(2): 131, April 2011. doi: 10.1088/0004-637X/731/2/131.
- Javier A. García, Thomas Dauser, Renee Ludlam, Michael Parker, Andrew Fabian, Fiona A. Harrison, and Jörn Wilms. Relativistic X-Ray Reflection Models for Accreting Neutron Stars. *ApJ*, 926(1):13, February 2022. doi: 10.3847/1538-4357/ac3cb7.
- G. Ghisellini, F. Haardt, and G. Matt. The contribution of the obscuring torus to the X-ray spectrum of Seyfert galaxies: a test for the unification model. *MNRAS*, 267: 743–754, April 1994. doi: 10.1093/mnras/267.3.743.
- R. Giacconi, W. P. Reidy, T. Zehnpfennig, J. C. Lindsay, and W. S. Muney. Solar X-Ray Image Obtained Using Grazing-Incidence Optics. *ApJ*, 142:1274–1278, October 1965. doi: 10.1086/148404.
- R. Giacconi, G. Branduardi, U. Briel, A. Epstein, D. Fabricant, E. Feigelson, W. Forman, P. Gorenstein, J. Grindlay, H. Gursky, F. R. Harnden, J. P. Henry, C. Jones, E. Kellogg, D. Koch, S. Murray, E. Schreier, F. Seward, H. Tananbaum, K. Topka, L. Van Speybroeck, S. S. Holt, R. H. Becker, E. A. Boldt, P. J. Serlemitsos, G. Clark, C. Canizares, T. Markert, R. Novick, D. Helfand, and K. Long. The Einstein (HEAO 2) X-ray Observatory. *ApJ*, 230:540–550, June 1979. doi: 10.1086/157110.
- Marek Gierliński, Andrzej Maciołek-Niedźwiecki, and Ken Ebisawa. Application of a relativistic accretion disc model to X-ray spectra of LMC X-1 and GRO J1655-40. *MNRAS*, 325(3):1253–1265, August 2001. doi: 10.1046/j.1365-8711.2001.04540.x.
- M. Gilfanov, M. Revnivtsev, and S. Molkov. Boundary layer, accretion disk and X-ray variability in the luminous LMXBs. *A&A*, 410:217–230, October 2003. doi: 10.1051/0004-6361:20031141.
- A. Gnarini, F. Ursini, G. Matt, S. Bianchi, F. Capitanio, M. Cocchi, R. Farinelli, and W. Zhang. Polarization properties of weakly magnetized neutron stars

- in low-mass X-ray binaries. *MNRAS*, 514(2):2561–2567, August 2022. doi: 10.1093/mnras/stac1523.
- R. W. Goosmann and C. M. Gaskell. Modeling optical and UV polarization of AGNs. I. Imprints of individual scattering regions. *A&A*, 465:129–145, April 2007. doi: 10.1051/0004-6361:20053555. URL <http://adsabs.harvard.edu/abs/2007A%26A...465..129G>.
- R. W. Goosmann, C. M. Gaskell, and F. Marin. Off-axis irradiation and the polarization of broad emission lines in active galactic nuclei. *Advances in Space Research*, 54:1341–1346, October 2014. doi: 10.1016/j.asr.2013.11.020. URL <http://adsabs.harvard.edu/abs/2014AdSpR...54.1341G>.
- Fiona A. Harrison, William W. Craig, Finn E. Christensen, Charles J. Hailey, William W. Zhang, Steven E. Boggs, Daniel Stern, W. Rick Cook, Karl Forster, Paolo Giommi, Brian W. Grefenstette, Yunjin Kim, Takao Kitaguchi, Jason E. Koglin, Kristin K. Madsen, Peter H. Mao, Hiromasa Miyasaka, Kaya Mori, Matteo Perri, Michael J. Pivovarov, Simonetta Puccetti, Vikram R. Rana, Niels J. Westergaard, Jason Willis, Andreas Zoglauer, Hongjun An, Matteo Bachetti, Nicolas M. Barrière, Eric C. Bellm, Varun Bhalerao, Nicolai F. Brejnholt, Felix Fuerst, Carl C. Liebe, Craig B. Markwardt, Melania Nynka, Julia K. Vogel, Dominic J. Walton, Daniel R. Wik, David M. Alexander, Lynn R. Cominsky, Ann E. Hornschemeier, Allan Hornstrup, Victoria M. Kaspi, Greg M. Madejski, Giorgio Matt, Silvano Molendi, David M. Smith, John A. Tomsick, Marco Ajello, David R. Ballantyne, Mislav Baloković, Didier Barret, Franz E. Bauer, Roger D. Blandford, W. Niel Brandt, Laura W. Brenneman, James Chiang, Deepto Chakrabarty, Jerome Chenevez, Andrea Comastri, Francois Dufour, Martin Elvis, Andrew C. Fabian, Duncan Farrah, Chris L. Fryer, Eric V. Gotthelf, Jonathan E. Grindlay, David J. Helfand, Roman Krivonos, David L. Meier, Jon M. Miller, Lorenzo Natalucci, Patrick Ogle, Eran O. Ofek, Andrew Ptak, Stephen P. Reynolds, Jane R. Rigby, Gianpiero Tagliaferri, Stephen E. Thorsett, Ezequiel Treister, and C. Megan Urry. The nuclear spectroscopic telescope array (nustar) high-energy x-ray mission. *The Astrophysical Journal*, 770(2):103, may 2013. doi: 10.1088/0004-637X/770/2/103. URL <https://dx.doi.org/10.1088/0004-637X/770/2/103>.
- G. Hasinger and M. van der Klis. Two patterns of correlated X-ray timing and spectral behaviour in low-mass X-ray binaries. *A&A*, 225:79–96, November 1989.
- Paul Hertz and Kent S. Wood. Discovery of a 4.2 Hour X-Ray Period in GX 9+9. *ApJ*, 331:764, August 1988. doi: 10.1086/166597.
- Jeroen Homan and Tomaso Belloni. The Evolution of Black Hole States. *Ap&SS*, 300(1-3):107–117, November 2005. doi: 10.1007/s10509-005-1197-4.
- L. Homer, P. A. Charles, and D. O’Donoghue. Evidence for a 2-h optical modulation in GS 1826–24. *Monthly Notices of the Royal Astronomical Society*, 298(2):

- 497–501, 08 1998. ISSN 0035-8711. doi: 10.1046/j.1365-8711.1998.01656.x. URL <https://doi.org/10.1046/j.1365-8711.1998.01656.x>.
- R. Iaria, S. M. Mazzola, T. Di Salvo, A. Marino, A. F. Gambino, A. Sanna, A. Riggio, and L. Burderi. Reflection component in the Bright Atoll Source GX 9+9. *A&A*, 635:A209, March 2020. doi: 10.1051/0004-6361/202037491.
- N. A. Inogamov and R. A. Sunyaev. Spread of matter over a neutron-star surface during disk accretion. *Astronomy Letters*, 25(5):269–293, May 1999.
- Zac Johnston, Alexander Heger, and Duncan K. Galloway. Multi-epoch X-ray burst modelling: MCMC with large grids of 1D simulations. *MNRAS*, 494(3): 4576–4589, May 2020. doi: 10.1093/mnras/staa1054.
- Peter G. Jonker, Michiel van der Klis, Rudy Wijnands, Jeroen Homan, Jan van Paradijs, Mariano Méndez, Eric C. Ford, Erik Kuulkers, and Frederick K. Lamb. The Power Spectral Properties of the Z Source GX 340+0. *ApJ*, 537(1):374–386, July 2000. doi: 10.1086/30902910.48550/arXiv.astro-ph/0002022.
- Taro Kotani, Ken Ebisawa, Tadayasu Dotani, Hajime Inoue, Fumiaki Nagase, Yasuo Tanaka, and Yoshihiro Ueda. ASCA Observations of the Absorption Line Features from the Superluminal Jet Source GRS 1915+105. *ApJ*, 539(1):413–423, August 2000. doi: 10.1086/309200.
- Henric Krawczynski, Fabio Muleri, Michal Dovčiak, Alexandra Veledina, Nicole Rodriguez Cavero, Jiri Svoboda, Adam Ingram, Giorgio Matt, Javier A. Garcia, Vladislav Loktev, Michela Negro, Juri Poutanen, Takao Kitaguchi, Jakub Podgorný, John Rankin, Wenda Zhang, Andrei Berdyugin, Svetlana V. Berdyugina, Stefano Bianchi, Dmitry Blinov, Fiamma Capitanio, Niccolò Di Lalla, Paul Draghis, Sergio Fabiani, Masato Kagitani, Vadim Kravtsov, Sebastian Kiehlmann, Luca Latronico, Alexander A. Lutovinov, Nikos Mandarakas, Frédéric Marin, Andrea Marinucci, Jon M. Miller, Tsunefumi Mizuno, Sergey V. Molkov, Nicola Omodei, Pierre-Olivier Petrucci, Ajay Ratheesh, Takeshi Sakanoi, Andrei N. Semena, Raphael Skalidis, Paolo Soffitta, Allyn F. Tennant, Phillipp Thalhammer, Francesco Tombesi, Martin C. Weisskopf, Joern Wilms, Sixuan Zhang, Iván Agudo, Lucio A. Antonelli, Matteo Bachetti, Luca Baldini, Wayne H. Baumgartner, Ronaldo Bellazzini, Stephen D. Bongiorno, Raffaella Bonino, Alessandro Brez, Niccolò Bucciantini, Simone Castellano, Elisabetta Cavazzuti, Stefano Ciprini, Enrico Costa, Alessandra De Rosa, Ettore Del Monte, Laura Di Gesu, Alessandro Di Marco, Immacolata Donnarumma, Victor Doroshenko, Steven R. Ehlert, Teruaki Enoto, Yuri Evangelista, Riccardo Ferrazzoli, Shuichi Gunji, Kiyoshi Hayashida, Jeremy Heyl, Wataru Iwakiri, Svetlana G. Jorstad, Vladimir Karas, Jeffery J. Kolodziejczak, Fabio La Monaca, Ioannis Liodakis, Simone Maldera, Alberto Manfreda, Alan P. Marscher, Herman L. Marshall, Ikuyuki Mitsuishi, Chi-Yung Ng, Stephen L. O’Dell, Chiara Oppedisano, Alessandro Papitto, George G. Pavlov, Abel L. Peirson, Matteo Perri, Melissa Pesce-Rollins,

- Maura Pilia, Andrea Possenti, Simonetta Puccetti, Brian D. Ramsey, Roger W. Romani, Carmelo Sgrò, Patrick Slane, Gloria Spandre, Toru Tamagawa, Fabrizio Tavecchio, Roberto Taverna, Yuzuru Tawara, Nicholas E. Thomas, Alessio Trois, Sergey Tsygankov, Roberto Turolla, Jacco Vink, Kinwah Wu, Fei Xie, and Silvia Zane. Polarized x-rays constrain the disk-jet geometry in the black hole x-ray binary Cygnus X-1. *Science*, 378(6620):650–654, November 2022. doi: 10.1126/science.add5399.
- N. D. Kylafis, I. Contopoulos, D. Kazanas, and D. M. Christodoulou. Formation and destruction of jets in X-ray binaries. *A&A*, 538:A5, February 2012. doi: 10.1051/0004-6361/201117052.
- Jean-Pierre Lasota. The disc instability model of dwarf novae and low-mass X-ray binary transients. *New Astron. Rev.*, 45(7):449–508, June 2001. doi: 10.1016/S1387-6473(01)00112-9.
- Li-Xin Li, Ramesh Narayan, and Jeffrey E. McClintock. Inferring the Inclination of a Black Hole Accretion Disk from Observations of its Polarized Continuum Radiation. *ApJ*, 691(1):847–865, January 2009. doi: 10.1088/0004-637X/691/1/847.
- K. S. Long, G. A. Chanan, and R. Novick. The X-ray polarization of the CYG sources. *ApJ*, 238:710–716, June 1980. doi: 10.1086/158027.
- Xiangyun Long, Hua Feng, Hong Li, Jiahuan Zhu, Qiong Wu, Jiahui Huang, Massimo Minuti, Weichun Jiang, Dongxin Yang, Saverio Citraro, Hikmat Nasimi, Jiandong Yu, Ge Jin, Ming Zeng, Peng An, Jiachen Jiang, Enrico Costa, Luca Baldini, Ronaldo Bellazzini, Alessandro Brez, Luca Latronico, Carmelo Sgrò, Gloria Spandre, Michele Pinchera, Fabio Muleri, and Paolo Soffitta. A Significant Detection of X-ray Polarization in Sco X-1 with PolarLight and Constraints on the Corona Geometry. *Astrophys. Lett.*, 924(1):L13, January 2022. doi: 10.3847/2041-8213/ac4673.
- Malcolm S. Longair. *High Energy Astrophysics*. 2011.
- R. M. Ludlam, E. M. Cackett, J. A. García, J. M. Miller, A. L. Stevens, A. C. Fabian, J. Homan, M. Ng, S. Guillot, D. J. K. Buisson, and D. Chakrabarty. Radius Constraints from Reflection Modeling of Cygnus X-2 with NuSTAR and NICER. *ApJ*, 927(1):112, March 2022. doi: 10.3847/1538-4357/ac5028.
- F. Marin, R. W. Goosmann, C. M. Gaskell, D. Porquet, and M. Dovčiak. Modeling optical and UV polarization of AGNs. II. Polarization imaging and complex reprocessing. *A&A*, 548:A121, December 2012. doi: 10.1051/0004-6361/201219751. URL <http://adsabs.harvard.edu/abs/2012A%26A...548A.121M>.

- Sera Markoff, Michael Nowak, Stéphane Corbel, Rob Fender, and Heino Falcke. Modeling the x-ray contribution of xrb jets. *New Astronomy Reviews*, 47(6): 491–493, 2003. ISSN 1387-6473. doi: [https://doi.org/10.1016/S1387-6473\(03\)00078-2](https://doi.org/10.1016/S1387-6473(03)00078-2). URL <https://www.sciencedirect.com/science/article/pii/S1387647303000782>. The physics of relativistic jets in the CHANDRA and XMM era.
- A. Martocchia, G. Matt, V. Karas, T. Belloni, and M. Feroci. Iron line diagnostics for the GRS 1915+105 black hole. *Nuclear Physics B Proceedings Supplements*, 132:404–407, June 2004. doi: 10.1016/j.nuclphysbps.2004.04.072.
- G. Matt, G. C. Perola, and L. Piro. The iron line and high energy bump as X-ray signatures of cold matter in Seyfert 1 galaxies. *A&A*, 247:25, July 1991.
- G. Matt, A. C. Fabian, and R. R. Ross. Iron K-alpha lines from X-ray photoionized accretion discs. *MNRAS*, 262:179–186, May 1993. doi: 10.1093/mnras/262.1.179.
- J. E. McClintock, R. Narayan, and R. Shafee. Estimating the spins of stellar-mass black holes. In Mario Livio and Anton M. Koekemoer, editors, *Black Holes*, pages 252–260. 2011.
- Jeffrey E. McClintock, Rebecca Shafee, Ramesh Narayan, Ronald A. Remillard, Shane W. Davis, and Li-Xin Li. The spin of the near-extreme kerr black hole GRS 1915105. *The Astrophysical Journal*, 652(1):518–539, nov 2006. doi: 10.1086/508457. URL <https://doi.org/10.1086/508457>.
- Jeffrey E. McClintock, Ramesh Narayan, and James F. Steiner. Black hole spin via continuum fitting and the role of spin in powering transient jets. *Space Science Reviews*, 183(1-4):295–322, jul 2013. doi: 10.1007/s11214-013-0003-9. URL <https://doi.org/10.1007/s11214-013-0003-9>.
- A. Merloni, A. C. Fabian, and R. R. Ross. On the interpretation of the multicolour disc model for black hole candidates. *MNRAS*, 313:193–197, March 2000. doi: 10.1046/j.1365-8711.2000.03226.x. URL <http://adsabs.harvard.edu/abs/2000MNRAS.313..193M>.
- A. V. Mescheryakov, M. G. Revnivtsev, and E. V. Filippova. Parameters of irradiated accretion disks from optical and X-ray observations of GS 1826-238. *Astronomy Letters*, 37(12):826–844, December 2011. doi: 10.1134/S1063773711120073.
- S. Migliari and R. P. Fender. Jets in neutron star X-ray binaries: a comparison with black holes. *MNRAS*, 366(1):79–91, February 2006. doi: 10.1111/j.1365-2966.2005.09777.x.
- S. Migliari, R. P. Fender, M. Rupen, P. G. Jonker, M. Klein-Wolt, R. M. Hjellming, and M. van der Klis. Disc-jet coupling in an atoll-type neutron star X-ray binary: 4U 1728-34 (GX 354-0). *MNRAS*, 342(4):L67–L71, July 2003. doi: 10.1046/j.1365-8711.2003.06795.x.

- K. Mitsuda, H. Inoue, K. Koyama, K. Makishima, M. Matsuoka, Y. Ogawara, N. Shibasaki, K. Suzuki, Y. Tanaka, and T. Hirano. Energy spectra of low-mass binary X-ray sources observed from Tenma. *PASJ*, 36:741–759, January 1984.
- Kazuhisa Mitsuda, Hajime Inoue, Norio Nakamura, and Yasuo Tanaka. Luminosity-related changes of the energy spectrum of X 1608-522. *PASJ*, 41:97–111, January 1989.
- Sigenori Miyamoto, Shunji Kitamoto, Kiyoshi Hayashida, and Wataru Egoshi. Large Hysteretic Behavior of Stellar Black Hole Candidate X-Ray Binaries. *Astrophys. Lett.*, 442:L13, March 1995. doi: 10.1086/187804.
- Aditya S Mondal, G C Dewangan, M Pahari, and B Raychaudhuri. NuSTAR view of the Z-type neutron star low-mass X-ray binary Cygnus X-2. *Monthly Notices of the Royal Astronomical Society*, 474(2):2064–2072, 11 2017. ISSN 0035-8711. doi: 10.1093/mnras/stx2931. URL <https://doi.org/10.1093/mnras/stx2931>.
- S. E. Motta, T. M. Belloni, L. Stella, T. Muñoz-Darias, and R. Fender. Precise mass and spin measurements for a stellar-mass black hole through X-ray timing: the case of GRO J1655-40. *MNRAS*, 437(3):2554–2565, January 2014. doi: 10.1093/mnras/stt2068.
- Michael P. Muno, Tomaso Belloni, Vivek Dhawan, Edward H. Morgan, Ronald A. Remillard, and Michael P. Rupen. A Lack of Radio Emission from Neutron Star Low-Mass X-Ray Binaries. *ApJ*, 626(2):1020–1027, June 2005. doi: 10.1086/429987.
- Sourabh Nampalliwar and Cosimo Bambi. *Accreting Black Holes*, pages 15–54. 07 2020. ISBN 978-981-15-6336-2. doi: 10.1007/978-981-15-6337-9_2.
- Ramesh Narayan, Jeffrey E. McClintock, and Rebecca Shafee. Estimating the Spins of Stellar-Mass Black Holes by Fitting Their Continuum Spectra. In Ye-Fei Yuan, Xiang-Dong Li, and Dong Lai, editors, *Astrophysics of Compact Objects*, volume 968 of *American Institute of Physics Conference Series*, pages 265–272, January 2008. doi: 10.1063/1.2840411.
- R. Novick, H. L. Kestenbaum, K. S. Long, E. H. Silver, M. C. Weisskopf, and R. S. Wolff. OSO-8 X-ray polarimeter and Bragg crystal spectrometer observations. *Highlights of Astronomy*, 4:95–97, January 1977.
- I. D. Novikov and K. S. Thorne. Astrophysics of black holes. In *Black Holes (Les Astres Occlus)*, pages 343–450, January 1973.
- Asaf Pe'er and Sera Markoff. X-Ray Emission from Transient Jet Model in Black Hole Binaries. *ApJ*, 753(2):177, July 2012. doi: 10.1088/0004-637X/753/2/177.

- Wim Penninx, Walter H. G. Lewin, Albert A. Zijlstra, Kazuhisa Mitsuda, and Jan van Paradijs. A connection between the X-ray spectral branches and the radio brightness in GX17 + 2. *Nature*, 336(6195):146–148, November 1988. doi: 10.1038/336146a0.
- G. Ponti, S. Bianchi, T. Muñoz-Darias, K. De, R. Fender, and A. Merloni. High ionisation absorption in low mass X-ray binaries. *Astronomische Nachrichten*, 337(4-5):512–517, May 2016. doi: 10.1002/asna.201612339.
- Robert Popham and Rashid Sunyaev. Accretion Disk Boundary Layers around Neutron Stars: X-Ray Production in Low-Mass X-Ray Binaries. *ApJ*, 547(1): 355–383, January 2001. doi: 10.1086/318336.
- A. Ratheesh, G. Matt, F. Tombesi, P. Soffitta, M. Pesce-Rollins, and A. Di Marco. Exploring the accretion-ejection geometry of GRS 1915+105 in the obscured state with future X-ray spectro-polarimetry. *A&A*, 655:A96, November 2021. doi: 10.1051/0004-6361/202140701.
- Ronald A. Remillard and Jeffrey E. McClintock. X-Ray Properties of Black-Hole Binaries. *ARA&A*, 44(1):49–92, September 2006. doi: 10.1146/annurev.astro.44.051905.092532.
- M. G. Revnivtsev and M. R. Gilfanov. Boundary layer emission and Z-track in the color-color diagram of luminous LMXBs. *A&A*, 453(1):253–259, July 2006. doi: 10.1051/0004-6361:20053964.
- Mikhail G. Revnivtsev, Valery F. Suleimanov, and Juri Poutanen. On the spreading layer emission in luminous accreting neutron stars. *MNRAS*, 434(3):2355–2361, September 2013. doi: 10.1093/mnras/stt1179.
- Christopher Reynolds. Black Hole Spin And Ionized Outflows In The Cooling-Flow Quasar H1821+643. NASA Proposal id.13-ADAP13-62, January 2013.
- Christopher S. Reynolds. Observing black holes spin. *Nature Astronomy*, 3:41–47, January 2019. doi: 10.1038/s41550-018-0665-z.
- Christopher S. Reynolds. Observational Constraints on Black Hole Spin. *ARA&A*, 59:117–154, September 2021. doi: 10.1146/annurev-astro-112420-035022.
- Christopher S. Reynolds and Andrew C. Fabian. Broad Iron-K α Emission Lines as a Diagnostic of Black Hole Spin. *ApJ*, 675(2):1048–1056, March 2008. doi: 10.1086/527344.
- A. Różańska, A. M. Dumont, B. Czerny, and S. Collin. The structure and radiation spectra of illuminated accretion discs in active galactic nuclei - I. Moderate illumination. *MNRAS*, 332(4):799–813, June 2002. doi: 10.1046/j.1365-8711.2002.05338.x.

- G. B. Rybicki and A. P. Lightman. *Radiative processes in astrophysics*. 1979.
- P. Savolainen, D. C. Hannikainen, O. Vilhu, A. Paizis, J. Nevalainen, and P. Hakala. Exploring the spreading layer of GX 9+9 using RXTE and INTEGRAL. *MNRAS*, 393(2):569–578, February 2009. doi: 10.1111/j.1365-2966.2008.14201.x.
- Jeremy D. Schnittman and Julian H. Krolik. X-RAY POLARIZATION FROM ACCRETING BLACK HOLES: THE THERMAL STATE. *The Astrophysical Journal*, 701(2):1175–1187, jul 2009. doi: 10.1088/0004-637x/701/2/1175. URL <https://doi.org/10.1088/0004-637x/701/2/1175>.
- Rebecca Shafee, Jonathan C. McKinney, Ramesh Narayan, Alexander Tchekhovskoy, Charles F. Gammie, and Jeffrey E. McClintock. Three-Dimensional Simulations of Magnetized Thin Accretion Disks around Black Holes: Stress in the Plunging Region. *Astrophys. Lett.*, 687(1):L25, November 2008. doi: 10.1086/593148.
- N. I. Shakura. Disk Model of Gas Accretion on a Relativistic Star in a Close Binary System. , 49:921, October 1972.
- N. I. Shakura and R. A. Sunyaev. Black holes in binary systems. Observational appearance. *A&A*, 24:337–355, 1973. URL <http://adsabs.harvard.edu/abs/1973A%26A...24..337S>.
- T. Shimura and F. Takahara. On the spectral hardening factor of the X-ray emission from accretion disks in black hole candidates. *ApJ*, 445:780–788, June 1995. doi: 10.1086/175740. URL <http://adsabs.harvard.edu/abs/1995ApJ...445..780S>.
- S. Piraino, A. Santangelo, P. Kaaret, Benjamin Muck, A. D’Ài, Tiziana di Salvo, R. Iaria, Natale R. Robba, L. Burderi, and Elise Egron. A relativistic iron emission line from the neutron star low-mass x-ray binary gx 3+1. *Astronomy and Astrophysics*, 542, 2012.
- R. F. Stark and P. A. Connors. Observational test for the existence of a rotating black hole in Cyg X-1. *Nature*, 266(5601):429–430, March 1977. doi: 10.1038/266429a0.
- James F. Steiner, Jeffrey E. McClintock, Ronald A. Remillard, Lijun Gou, Shin’ya Yamada, and Ramesh Narayan. The constant inner-disk radius of lmc x-3: A basis for measuring black hole spin. *The Astrophysical Journal Letters*, 718(2):L117, jul 2010. doi: 10.1088/2041-8205/718/2/L117. URL <https://dx.doi.org/10.1088/2041-8205/718/2/L117>.
- Luigi Stella and Mario Vietri. kHz Quasiperiodic Oscillations in Low-Mass X-Ray Binaries as Probes of General Relativity in the Strong-Field Regime. *Phys. Rev. Lett.*, 82(1):17–20, January 1999. doi: 10.1103/PhysRevLett.82.17.

- Valery Suleimanov and Juri Poutanen. Spectra of the spreading layers on the neutron star surface and constraints on the neutron star equation of state. *Monthly Notices of the Royal Astronomical Society*, 369(4):2036–2048, 07 2006. ISSN 0035-8711. doi: 10.1111/j.1365-2966.2006.10454.x. URL <https://doi.org/10.1111/j.1365-2966.2006.10454.x>.
- R. A. Sunyaev and L. G. Titarchuk. Comptonization of X-Rays in Plasma Clouds - Typical Radiation Spectra. *A&A*, 86:121, June 1980.
- R. A. Syunyaev, V. A. Arefev, K. N. Borozdin, M. R. Gilfanov, V. V. Efremov, A. S. Kaniovskii, E. M. Churazov, E. Kendziorra, B. Mony, P. Kretschmar, M. Maisack, R. Staubert, S. Dobereiner, J. Englhauser, W. Pietsch, C. Reppin, J. Trumper, G. K. Skinner, M. R. Nottingham, H. Pan, and A. P. Willmore. Broadband X-Ray Spectra of Black-Hole Candidates X-Ray Pulsars and Low-Mass Binary X-Ray Systems - KVANT Module Results. *Soviet Astronomy Letters*, 17:409, November 1991.
- Y. Tanaka and N. Shibazaki. X-ray Novae. *ARA&A*, 34:607–644, January 1996. doi: 10.1146/annurev.astro.34.1.607.
- R. Taverna, W. Zhang, M. Dovčiak, S. Bianchi, M. Bursa, V. Karas, and G. Matt. Towards a complete description of spectra and polarization of black hole accretion discs: albedo profiles and returning radiation. *MNRAS*, 493(4):4960–4977, April 2020. doi: 10.1093/mnras/staa598.
- R. Taverna, L. Marra, S. Bianchi, M. Dovčiak, R. Goosmann, F. Marin, G. Matt, and W. Zhang. Spectral and polarization properties of black hole accretion disc emission: including absorption effects. *MNRAS*, 501(3):3393–3405, March 2021. doi: 10.1093/mnras/staa3859.
- A. J. Tetarenko, G. R. Sivakoff, J. C. A. Miller-Jones, E. W. Rosolowsky, G. Petitpas, M. Gurwell, J. Wouterloot, R. Fender, S. Heinz, D. Maitra, S. B. Markoff, S. Migliari, M. P. Rupen, A. P. Rushton, D. M. Russell, T. D. Russell, and C. L. Sarazin. Extreme jet ejections from the black hole X-ray binary V404 Cygni. *MNRAS*, 469(3):3141–3162, August 2017. doi: 10.1093/mnras/stx1048.
- Jaap Tinbergen. *Astronomical Polarimetry*. 2005.
- Y. Ueda, H. Inoue, Y. Tanaka, K. Ebisawa, F. Nagase, T. Kotani, and N. Gehrels. Detection of Absorption-Line Features in the X-Ray Spectra of the Galactic Superluminal Source GRO J1655-40. *ApJ*, 492(2):782–787, January 1998. doi: 10.1086/305063.
- M. van der Klis. Rapid aperiodic variability in X-ray binaries. In *X-ray Binaries*, pages 252–307, January 1995.

- Steve van Straaten, Michiel van der Klis, and Mariano Méndez. The Atoll Source States of 4U 1608-52. *ApJ*, 596(2):1155–1176, October 2003. doi: 10.1086/37815510.48550/arXiv.astro-ph/0307041.
- O. Vilhu, A. Paizis, D. Hannikainen, J. Schultz, and V. Beckmann. The Spreading Layer of GX9+9 421. In *The Obscured Universe. Proceedings of the VI INTEGRAL Workshop*, volume 622 of *ESA Special Publication*, page 421, January 2007.
- M. C. Weisskopf, E. H. Silver, H. L. Kestenbaum, K. S. Long, and R. Novick. A precision measurement of the X-ray polarization of the Crab Nebula without pulsar contamination. *Astrophys. Lett.*, 220:L117–L121, March 1978. doi: 10.1086/182648.
- Martin C. Weisskopf, Ronaldo Bellazzini, Enrico Costa, Brian D. Ramsey, Stephen L. O’Dell, Ronald F. Elsner, Allyn F. Tennant, George G. Pavlov, Giorgio Matt, Victoria M. Kaspi, Paolo S. Coppi, Kinwah Wu, Oswald H. W. Siegmund, and Vyacheslav E. Zavlin. An imaging x-ray polarimeter for the study of galactic and extragalactic x-ray sources. In Martin J. L. Turner and Kathryn A. Flanagan, editors, *Space Telescopes and Instrumentation 2008: Ultraviolet to Gamma Ray*, volume 7011 of *Society of Photo-Optical Instrumentation Engineers (SPIE) Conference Series*, page 70111I, July 2008. doi: 10.1117/12.788184.
- Martin C. Weisskopf, Brian Ramsey, Stephen L. O’Dell, Allyn Tennant, Ronald Elsner, Paolo Soffita, Ronaldo Bellazzini, Enrico Costa, Jeffery Kolodziejczak, Victoria Kaspi, Fabio Mulieri, Herman Marshall, Giorgio Matt, and Roger Romani. The imaging x-ray polarimetry explorer (ixpe). *Results in Physics*, 6: 1179–1180, 2016. ISSN 2211-3797. doi: <https://doi.org/10.1016/j.rinp.2016.10.021>. URL <https://www.sciencedirect.com/science/article/pii/S221137971630448X>.
- Martin C. Weisskopf, Paolo Soffitta, Luca Baldini, Brian D. Ramsey, Stephen L. O’Dell, Roger W. Romani, Giorgio Matt, William D. Deinger, Wayne H. Baumgartner, Ronaldo Bellazzini, Enrico Costa, Jeffery J. Kolodziejczak, Luca Latronico, Herman L. Marshall, Fabio Muleri, Stephen D. Bongiorno, Allyn Tennant, Niccolo Bucciantini, Michal Dovciak, Frederic Marin, Alan Marscher, Juri Poutanen, Pat Slane, Roberto Turolla, William Kalinowski, Alessandro Di Marco, Sergio Fabiani, Massimo Minuti, Fabio La Monaca, Michele Pinchera, John Rankin, Carmelo Sgro’, Alessio Trois, Fei Xie, Cheryl Alexander, D. Zachery Allen, Fabrizio Amici, Jason Andersen, Angelo Antonelli, Spencer Antoniak, Primo Attinà, Mattia Barbanera, Matteo Bachetti, Randy M. Baggett, Jeff Bladt, Alessandro Brez, Raffaella Bonino, Christopher Boree, Fabio Borotto, Shawn Breeding, Daniele Brienza, H. Kyle Bygott, Ciro Caporale, Claudia Cardelli, Rita Carpentiero, Simone Castellano, Marco Castronuovo, Luca Cavalli, Elisabetta Cavazzuti, Marco Ceccanti, Mauro Centrone, Saverio Citraro, Fabio D’Amico, Elisa D’Alba, Laura Di Gesu, Ettore Del Monte, Kurtis L. Dietz, Niccolo’

- Di Lalla, Giuseppe Di Persio, David Dolan, Immacolata Donnarumma, Yuri Evangelista, Kevin Ferrant, Riccardo Ferrazzoli, MacKenzie Ferrie, Joseph Footdale, Brent Forsyth, Michelle Foster, Benjamin Garelick, Shuichi Gunji, Eli Gurnee, Michael Head, Grant Hibbard, Samantha Johnson, Erik Kelly, Kiranmayee Kilaru, Carlo Lefevre, Shelley Le Roy, Pasqualino Loffredo, Paolo Lorenzi, Leonardo Lucchesi, Tyler Maddox, Guido Magazzu, Simone Maldera, Alberto Manfreda, Elio Mangraviti, Marco Marengo, Alessandra Marrocchesi, Francesco Massaro, David Mauger, Jeffrey McCracken, Michael McEachen, Rondal Mize, Paolo Mereu, Scott Mitchell, Ikuyuki Mitsuishi, Alfredo Morbidini, Federico Mosti, Hikmat Nasimi, Barbara Negri, Michela Negro, Toan Nguyen, Isaac Nitschke, Alessio Nuti, Mitch Onizuka, Chiara Oppedisano, Leonardo Orsini, Darren Osborne, Richard Pacheco, Alessandro Paggi, Will Painter, Steven D. Pavelitz, Christina Pentz, Raffaele Piazzolla, Matteo Perri, Melissa Pesce-Rollins, Colin Peterson, Maura Pilia, Alessandro Profeti, Simonetta Puccetti, Jaganathan Ranganathan, Ajay Ratheesh, Lee Reedy, Noah Root, Alda Rubini, Stephanie Ruswick, Javier Sanchez, Paolo Sarra, Francesco Santoli, Emanuele Scalise, Andrea Sciortino, Christopher Schroeder, Tim Seek, Kalie Sosdian, Gloria Spandre, Chet O. Speegle, Toru Tamagawa, Marcello Tardiola, Antonino Tobia, Nicholas E. Thomas, Robert Valerie, Marco Vimercati, Amy L. Walden, Bruce Weddendorf, Jeffrey Wedmore, David Welch, Davide Zanetti, and Francesco Zanetti. The Imaging X-Ray Polarimetry Explorer (IXPE): Pre-Launch. *Journal of Astronomical Telescopes, Instruments, and Systems*, 8(2):026002, April 2022. doi: 10.1117/1.JATIS.8.2.026002.
- N. E. White, L. Stella, and A. N. Parmar. The X-Ray Spectral Properties of Accretion Disks in X-Ray Binaries. *ApJ*, 324:363, January 1988. doi: 10.1086/165901.
- R. A. D. Wijnands, M. van der Klis, E. Kuulkers, K. Asai, and G. Hasinger. Ginga observations of cygnus x-2, 1997. URL <https://arxiv.org/abs/astro-ph/9704229>.
- Shin'ya Yamada, Kazuo Makishima, Chris Done, Shunsuke Torii, Hirofumi Noda, and Soki Sakurai. Evidence for a cool disk and inhomogeneous coronae from wide-band temporal spectroscopy of cygnus x-1 with suzaku. *Publications of the Astronomical Society of Japan*, 65, 04 2013. doi: 10.1093/pasj/65.4.80.
- Michael Zamfir, Andrew Cumming, and Duncan K. Galloway. Constraints on Neutron Star Mass and Radius in GS 1826-24 from Sub-Eddington X-Ray Bursts. *ApJ*, 749(1):69, April 2012. doi: 10.1088/0004-637X/749/1/69.
- S. N. Zhang, W. Cui, and W. Chen. Black Hole Spin in X-Ray Binaries: Observational Consequences. *Astrophys. Lett.*, 482:L155–L158, June 1997. doi: 10.1086/310705. URL <http://adsabs.harvard.edu/abs/1997ApJ...482L.155Z>.
- S. N. Zhang, M. Feroci, A. Santangelo, Y. W. Dong, H. Feng, F. J. Lu, K. Nandra, Z. S. Wang, S. Zhang, E. Bozzo, S. Brandt, A. De Rosa, L. J. Gou, M. Hernanz,

- M. van der Klis, X. D. Li, Y. Liu, P. Orleanski, G. Pareschi, M. Pohl, J. Poutanen, J. L. Qu, S. Schanne, L. Stella, P. Uttley, A. Watts, R. X. Xu, W. F. Yu, J. J. M. in 't Zand, S. Zane, L. Alvarez, L. Amati, L. Baldini, C. Bambi, S. Basso, S. Bhattacharyya, R. Bellazzini, T. Belloni, P. Bellutti, S. Bianchi, A. Brez, M. Bursa, V. Burwitz, C. Budtz-Jørgensen, I. Caiazzo, R. Campana, X. L. Cao, P. Casella, C. Y. Chen, L. Chen, T. Chen, Y. Chen, Y. Chen, Y. P. Chen, M. Civitani, F. Coti Zelati, W. Cui, W. W. Cui, Z. G. Dai, E. Del Monte, D. de Martino, S. Di Cosimo, S. Diebold, M. Dovciak, I. Donnarumma, V. Doroshenko, P. Esposito, Y. Evangelista, Y. Favre, P. Friedrich, F. Fuschino, J. L. Galvez, Z. L. Gao, M. Y. Ge, O. Gevin, D. Goetz, D. W. Han, J. Heyl, J. Horak, W. Hu, F. Huang, Q. S. Huang, R. Hudec, D. Huppenkothen, G. L. Israel, A. Ingram, V. Karas, D. Karelin, P. A. Jenke, L. Ji, S. Korpela, D. Kunneriath, C. Labanti, G. Li, X. Li, Z. S. Li, E. W. Liang, O. Limousin, L. Lin, Z. X. Ling, H. B. Liu, H. W. Liu, Z. Liu, B. Lu, N. Lund, D. Lai, B. Luo, T. Luo, B. Ma, S. Mahmoodifar, M. Marisaldi, A. Martindale, N. Meidinger, Y. P. Men, M. Michalska, R. Mignani, M. Minuti, S. Motta, F. Muleri, J. Neilsen, M. Orlandini, A. T. Pan, A. Patruno, E. Perinati, A. Picciotto, C. Piemonte, M. Pinchera, A. Rachevski, M. Rapisarda, N. Rea, E. M. R. Rossi, A. Rubini, G. Sala, X. W. Shu, C. Sgro, Z. X. Shen, P. Soffitta, L. M. Song, G. Spandre, G. Stratta, T. E. Strohmayer, L. Sun, J. Svoboda, G. Tagliaferri, C. Tenzer, T. Hong, R. Taverna, G. Torok, R. Turolla, S. Vacchi, J. Wang, D. Walton, K. Wang, J. F. Wang, R. J. Wang, Y. F. Wang, S. S. Weng, J. Wilms, B. Winter, X. Wu, X. F. Wu, S. L. Xiong, Y. P. Xu, Y. Q. Xue, Z. Yan, S. Yang, X. Yang, Y. J. Yang, F. Yuan, W. M. Yuan, Y. F. Yuan, G. Zampa, N. Zampa, A. Zdziarski, C. Zhang, C. L. Zhang, L. Zhang, X. Zhang, Z. Zhang, W. D. Zhang, S. J. Zheng, P. Zhou, and X. L. Zhou. eXTP: Enhanced x-ray timing and polarization mission. In Jan-Willem A. den Herder, Tadayuki Takahashi, and Marshall Bautz, editors, *SPIE Proceedings*. SPIE, jul 2016. doi: 10.1117/12.2232034. URL <https://doi.org/10.1117%2F12.2232034>.
- Wenda Zhang, Michal Dovčiak, and Michal Bursa. Constraining the Size of the Corona with Fully Relativistic Calculations of Spectra of Extended Coronae. I. The Monte Carlo Radiative Transfer Code. *ApJ*, 875(2):148, April 2019. doi: 10.3847/1538-4357/ab1261.
- Wenda Zhang, Michal Dovčiak, Michal Bursa, Vladimír Karas, Giorgio Matt, and Francesco Ursini. Investigating the X-ray polarization of lamp-post coronae in BHXRBs. *MNRAS*, 515(2):2882–2889, September 2022. doi: 10.1093/mnras/stac193710.48550/arXiv.2207.03228.

.so long and thanks for all the fish